INVESTIGATION EFFECT OF EXTERNAL STRESS ON HYDROGEN SOLVUS IN A ZIRCALOY-4 FUEL CLADDING ALLOY: APPLICATION OF IN SITU DIFFRACTION TECHNIQUE AND MESOSCALE PHASE-FIELD SIMULATION

BY

JUN-LI LIN

DISSERTATION

Submitted in partial fulfillment of the requirements
for the degree of Doctor of Philosophy in Nuclear, Plasma and Radiological Engineering
in the Graduate College of the
University of Illinois at Urbana-Champaign, 2018

Urbana, Illinois

Doctoral Committee:

Professor Brent J. Heuser, Chair and Director of Research
Professor James F. Stubbins
Professor Pascal Bellon
Professor Yang Zhang

ABSTRACT

Zircaloy-4 is widely used as a nuclear fuel cladding material in light water reactors (LWRs). However, the formation of the zirconium hydride phase in the cladding significantly degrades its mechanical properties by reducing the local ductility and initiating crack propagation. Therefore, one of the current fuel performance modeling efforts is to simulate the degradation of the cladding properties caused by the hydride phase. Distribution of the hydride phase in the cladding is mainly controlled by the temperature and the stress value. The temperature effect can be modeled using the hydrogen solvus and the temperature-driven hydrogen diffusion (Soret effect). However, while correlating the effect of stress on hydride formation, a disagreement arises between the experimental data and the theoretical model. The theory predicts that the effect of stress is negligible while experiments observe that hydrides preferentially accumulates in regions with high tensile stress. This contradiction hinders accurately incorporating the stress effect into the fuel performance code. The purpose of this doctoral research is to resolve this disagreement by performing a systematic experimental and modeling study; also to provide valuable information to model the effect of stress on hydride formation in zirconium-based alloys.

For the experimental study, we utilized an in situ diffraction technique to investigate the evolution of hydride phase in a Zircaloy-4 material under different thermo-mechanical conditions. Zircaloy-4 tensile specimens with hydrogen concentrations ranging from 0 to 977 wppm were tested under isothermal, slow cooling and thermal cycling conditions. A uniaxial tensile stress was applied to the specimens throughout the thermal processes. The test temperature ranged from 25 to 420 °C and the applied stress ranged from 78 to 218 MPa. Diffraction spectra were recorded during the thermo-mechanical processes as a function of temperature and stress value; phase information was obtained from the spectra. The

analysis focused on the effect of stress on precipitation and dissolution of the hydride phase. Experimental results showed the hydride phase was stable under the isothermal condition if the applied stress was less than the yield stress of the zirconium matrix. However, the stress significantly affected the hydride precipitation and dissolution behavior under slow-cooling and thermal-cycling conditions. This stress effect depended on the Zr crystalline orientation. The stress increased the amount of hydrogen in solution for Zr crystals which had their basal plane normal (c-axis) inclined toward the tensile stress direction. This also implies the stress delayed hydride precipitation or promoted hydride dissolution in these crystals. If we described the evolution of the hydrogen concentration in solution of these crystals by an Arrhenius type equation, we find that stress significantly decreased the energy term Q in the Arrhenius behavior. The average Q reduction was 97 J/molH per MPa of tensile stress. This is a significant effect compared to the current theory ($\sim$ 0.086 J/molH per MPa of tensile stress). Thus, our experimental result is inconsistent with the theory.

We performed the phase-field modeling to understand this disagreement. The CALPHAD-based phase-field code Hyrax was used to quantitatively model the hydrogen solvus in a zirconium solution. Hyrax was built on the finite element framework MOOSE and was specifically developed for the binary zirconium-hydrogen system. We first modeled the hydrogen solvus in an external-stress free, single zirconium crystal system. The output of this modeling was successfully validated by comparing with experimental data.

The external stress effect was then incorporated. Tensile stress was applied to a single zirconium crystal and a bi-crystal system. For the single crystal system, the hydrogen solvus was not affected by the stress, regardless of the loading direction. For the bi-crystals system, the stress redistributed the hydride between the two crystals. The hydride phase preferentially accumulated in the crystal which had the c-axis parallel to the stress. However, the equilibrium hydrogen solvus in the bi-crystal system was not affected by the stress. These results indicate the stress does not affect the hydrogen solvus but re-distributes the hydride between zirconium crystals. This is because the stress yields different strain energy in crystals with different crystalline orientations and creates an energy gradient that drives the hydrogen diffusion. The hydride preferentially precipitates in low strain energy region which creates more lattice misfit strain to compensate the gradient. This explains why stress would

affect hydride dissolution and precipitation differently in different Zr crystals as observed by the diffraction experiments. The modeling result also supports the theoretical prediction that the external stress does not affect hydrogen solvus.

An important conclusion is that the external stress does not affect hydrogen solvus in zirconium solution but facilitates hydride re-distribution in a system. The hydride phase distribution does not depend on the stress value but depend on the strain energy gradient. Hydrides re-distribute and accumulate in regions which have relatively low strain energy.

To my wife Pei-Yun, my family, friends, and scientists of the past and the future.

ACKNOWLEDGMENTS

I would like to express my greatest appreciation to my advisor, Dr. Brent J. Heuser, for his continuous support of my doctoral research. He gave me opportunities to chase my research ideas with his full encouragement behind. I would also like to thank my doctoral committee: Dr. James F. Stubbins, Dr. Yang Zhang, and especially Dr. Pascal Bellon for their encouragement and insightful comments and questions. I would also like to thank my group members, Weicheng Zhong, Peter Mouche, Donghee Park, Dr. Xiaochun Han, Dr. Mohamed S. ElBakhshwan, and Dr. Kuan-Che Lan for their encouragement and support. I would express great appreciation to Dr. Kun Mo, who offers many research opportunities and shares his knowledge with me. I would also gratefully appreciate Dr. Andrea M. Jokisaari, who assists me to learn phase-field model as well as reaching computational resources for me.

I would like to acknowledge the experimental instruments used in pursuit of this doctoral research. This work was carried out in part in the Frederick Seitz Materials Research Laboratory Central Research Facilities at the University of Illinois at Urbana-Champaign. The use of the VULCAN Engineering Materials Diffractometer at the Spallation Neutron Source, Oak Ridge National Laboratory, is supported by the Scientific User Facilities Division, the Office of Basic Energy Sciences, U.S. Department of Energy. Also, the use of the 1-ID Beamline at the Advanced Photon Source, Argonne National Laboratory, is supported by the Scientific User Facilities Division, the Office of Basic Energy Sciences, U.S. Department of Energy. I would also like to acknowledge the usage of the computational resources. The simulation work was carried out using the Illinois Campus Cluster at the University of Illinois at Urbana-Champaign and the High-Performance Computing Center at Idaho National Laboratory. I would also express my gratitude to Dr. Andrea M. Jokisaari for her generous

support on Hyrax, and the MOOSE team at Idaho National Laboratory for their help and support. This work was supported by the US Department of Energy Nuclear Energy Fuel Aging in Storage and Transportation IRP under Grant Number IRP-2011-05352, the US Department of Energy Accident Tolerant Fuel IRP under Contract Number IRP-12-4728, and by the University of Illinois Campus Research Board under Award Number RB17006.

I would like to thank my families and friends for enriching my life, especially Yu-Tsun Shao, for his invaluable personal support and scientific guidance. Word cannot express my love and appreciation for my wife, Pei-Yun Hsiao, who has always been on my side throughout my doctoral career.

This research would not have been possible without these people. I also express my deepest respect and appreciation to all scientists, who continually extend the boundaries of human knowledge.

TABLE OF CONTENTS

LIST OF TABLES

LIST OF FIGURES

CHAPTER 1

INTRODUCTION

Zircaloy-4 is one of the most common fuel cladding materials used in light water reactors due to excellent mechanical properties, corrosion resistance, and low thermal neutron absorption cross-section. While a reactor operates, corrosion of the outer wall of the cladding and radiolysis of the water coolant creates hydrogen. A fraction of the hydrogen diffuses into the cladding and dissolves in the zirconium solution. The zirconium hydride phase starts precipitating once the hydrogen concentration exceeds the terminal solid solubility. These hydride particles distribute inhomogeneously within the cladding due to a temperature gradient across the cladding thickness; the waterside temperature is approximately 50 °C lower than the fuel side. Therefore, hydride preferentially precipitates on the waterside of the cladding, generating a rim morphology (high density of hydride particle). An extreme example is a hydride blister (bulky pure hydride structure) forms at defect locations where the oxide layer spalled off. Hydride precipitation has deleterious effects on cladding properties. It limits the fuel burn-up and impacts the life of cladding in service and in the long-term storage. The brittle hydride phase reduces the local ductility, initiates early crack formation and induces delayed hydride cracking (DHC) phenomenon on the cladding.

It is thus important to measure the amount of hydride formed at a certain level of hydrogen concentration. Therefore, the terminal solid solubility for hydrogen in zirconium alloys solution has been established. The hydrogen terminal solid solubility increases exponentially with increasing temperature and is usually described using the Arrhenius equation. The hydrogen solubility as a function of temperature is also known as the hydrogen solvus. In the binary zirconium-hydrogen system, precipitation of the less dense hydride phase (δ-hydride) elastically and plastically distorts the zirconium phase. The plastic strain energy is compensated by undercooling required to precipitate the hydride. Hence the precipita-

tion temperature of zirconium hydride is lower than the dissolution temperature, causing a hysteresis between the two temperatures. The hydrogen solvus is applied to calculate the fraction of hydride at a certain hydrogen concentration and is useful when predicting the loss of mechanical properties caused by the deleterious hydride phase.

Besides the temperature, it is possible the stress gradient in a component can affect the hydride distribution. In principle, the strain energy provided by an external stress should reduce the hysteresis by decreasing the dissolution temperature and increasing precipitation temperature. The theory for the external stress effect on hydrogen solvus in zirconium alloys has been studied in a series of papers in the past 40 years. Section 2.3.1 summarizes the details of the theory development. Puls's hydrogen solvus equation is widely adopted as the most updated theory. In this model, the effect of external stress on hydrogen solubility in zirconium is negligible even at a high-level of stress ($\sim$1800 MPa). However, only a few experimental data can be used to validate the theory due to the difficulty of performing in situ experiments. In fact, these experimental data result in different conclusions regarding the external stress effect on the hydrogen solvus; a significant change of the hydrogen solvus under a relatively low-level of stress (160 - 240 MPa) is observed. This inconsistency between the experiment and the theory has not been solved. Section 2.4 discusses this in detail.

Zircaloy cladding is a primary structure in a fuel-pellet component. Failure of the cladding structure causes the release of radionuclides, posting a threat to reactors and long-term storage environment. Thus, any factor that potentially affects the cladding integrity should be predictable. Recent efforts focus on fuel performance code development to model the possible phenomena that occur in a fuel component. Examples are FRAPCON, FALCON, BISON and MARMOT. MOOSE is a multiphysics, parallel finite-element framework which is capable to solve coupled differential equations for various systems. BISON and MARMOTH inherit parts of the MOOSE physic modules and further extend to model engineering and mesoscale fuel performance. Fuel performance modeling efforts combine MOOSE-BISON-MARMOT (MBM) for the multiscale modeling on current LWR and the next generation fuel components. The fuel cladding phenomenon are also included in MBM. An important study is to model the hydride phase formation in the zirconium-based cladding. The effect of temperature on hydride distribution in the cladding has been successfully implemented.

The temperature-driven diffusion is modeled by building in Soret effect, and the hydride formation is predicted by hydrogen solvus, a temperature-dependent function. However, the current code does not incorporate the effect of stress on hydride formation. This is because the inconsistency between the experiment and the theory generates uncertainty for using the current stress model.

This doctoral research aims to provide a more comprehensive understanding of hydrogen dissolution/precipitation behavior in a zirconium alloy. The variation of hydrogen solvus was studied using in situ diffraction under a uniform tensile stress and different thermomechanical conditions. Phase-field modeling was used to quantitatively study the hydrogen solubility in a zirconium matrix with and without an external stress. This study has successfully explained the disagreement between the experiment and the theory.

CHAPTER 2

LITERATURE REVIEW

2.1 Properties of Zircaloy alloys

2.1.1 Alloying elements

A systematic study of the development of the Zr-based binary alloys was primarily led by U.S. Navy near the end of the World War II [4, 19]. Zirconium was favored for use as a fuel cladding material in the light water reactors (LWRs) because of its low thermal neutron cross-section and adequate mechanical properties. The poor corrosion resistance of a highly purified zirconium resulted in catastrophic failure of this material in the reactor environment [19]. Among a series of testing, Battelle Memorial Inst. and Iowa State College discovered that the addition of tin could enhance corrosion resistance of a pure zirconium metal [3]. It was known that a certain level of tin can mitigate the deleterious effect of nitrogen and other impurities. However, it was also found that the excess amount of tin accelerated the oxide formation on the zirconium-tin alloys, reducing the corrosion resistance [3]. The addition of tin generated Sn^{3+} ions which increased the O^{2-} vacancy concentration by replacing Zr^{4+} in oxygen-deficient ZrO_{2-x} lattices. This enhanced the oxygen diffusion through the oxide layer to the fresh metal matrix, accelerating the corrosion rate (assuming the zirconium corrosion rate was dominated by oxygen ion transportation in the reactor environment). Therefore, reducing the tin content minimized this effect. However, without the addition of tin, the corrosion resistance of zirconium alloy was degraded by the presence of nitrogen impurities. It was believed that the N^{3-} ion replaced the O^{2-} ion sites, increasing the amount of oxygen vacancy and enhanced the corrosion rate [3]. By adding a trace amounts of tin, the Sn^{3+} ions formed clusters with the N^{3-} ions and the O^{2-} vacancy, decreasing the mobility of

the oxygen vacancy. The formation of the Sn^{3+}-N^{3-}-O^{2-} ion-vacancy cluster decreased the volumetric strain associated with the three individual elements and was preferred by the system [2]. A study done by Garde *et al.* [2] showed that by optimizing the tin content (1.2% to 1.7% weight fraction), the corrosion resistance of a Zircaloy-4 alloy was improved by 30 to 40%; their experimental data is shown in Fig. 2.1, where the corrosion resistance of the material decreases as the tin content decreases. Tin stays in the solid solution at this concentration range and acts as a α stabilizer as it expands the α-Zr region. A zirconium-tin binary phase diagram is shown in Ref. [20].

It was later found that the addition of tin could not reach its maximum beneficial effect unless iron (Fe), nickel (Ni) and chromium (Cr) were also added [3, 4]. This discovery came from an accidental contamination of a Zr-2.5Sn alloy by a stainless steel ingot during the

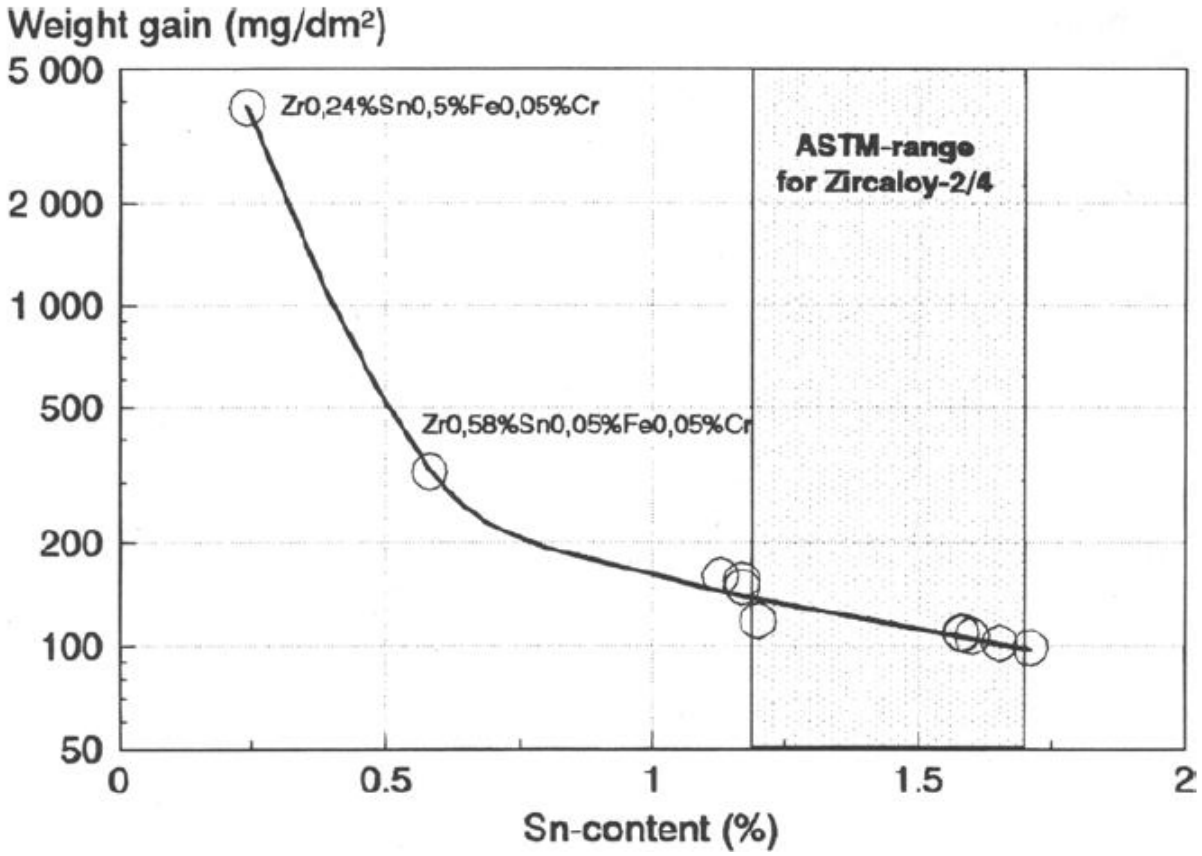

Figure 2.1: Showing effect of the tin concentration on the corrosion resistance of a ZrSnFeCr-alloy. A higher amount of weight-gain was observed at a lower tin content. This figure was reprinted from the Fig. 8 in Ref. [2].

melting process. The solubility of these elements in the α-Zr phase is very low; around 120 ppm for iron and 200 ppm for chromium at the maximum temperature of the α-Zr phase [21]. Therefore, these elements formed the intermetallic second phase particles (SPPs) within the α-Zr matrix, having a general formula of Zr_2(Ni,Fe) or Zr(Fe,Cr)$_2$. Interestingly, the addition of these insoluble elements did not decrease the oxidation rate but contributed to the earlier onset of the linear post-transition oxidation behavior where the oxidation rate was not diffusional controlled [22]. This helped create a more uniform and protective oxide layer which prevented the early spallation of the surface oxide. An experiment done by Garde *et al.* [2] suggested that there is a complex relationship between the SPP size and the corrosion resistance. Their data is shown in Fig. 2.2. They came to a conclusion that the zirconium alloy can achieve highest corrosion resistance when having the SPP size of 0.075 to 0.12 µm; the physical reason behind is, however, not fully understood yet.

Since the size, morphology, and distribution of these second phase precipitate significantly depended on the thermomechanical treatment of the manufacturing process, a cumulative annealing parameter (CAP) was developed to estimate the complete heat treatment history in order to predict the desired particle size and morphology. For example, Garzarolli *et al.* [23] have shown that a CAP value below 10^{-18} hr (for $Q/R = 40000$ K) would yield precipitates which have high nodular corrosion resistance, whereas a CAP above 10^{-19} hr yields precipitates which have high uniform corrosion resistance. These second phase particles also slightly increase the strength of the alloy by dispersion strengthening. We note that the complete thermomechanical treatments for the SPPs vary between companies and are proprietary.

Oxygen, another common element in Zircaloy, is not considered to be an impurity but an alloying element. The oxygen was artificially added to the alloy by adding the ZrO_2 powder during the manufacturing process with the average oxygen concentration range of 800-1600 ppm [4]. The purpose was to increase the strength of the alloy by solid solution strengthening. It was found that the yield strength of the alloy was increased by 150 MPa at the room temperature with the addition of 1000 ppm oxygen [4]. Oxygen is also an α stabilizer that expands the α-Zr region.

The choice of alloying elements led to the development of Zircaloy-2 (Zry-2), Zircaloy-3

(Zry-3) and Zircaloy-4 (Zry-4) alloys. Zry-3, a low tin alloy ($\sim$ 0.25% of tin), was soon abandoned due to the poor corrosion and manufacture issue [3]. Zry-4 was developed with the purpose to mitigate the hydrogen absorption by reducing the nickel content. This alloy contains the same chromium and tin concentration as the Zry-2 but has a higher iron level to compensate the removal of nickel from the alloy. Since the Zry-2 was well developed prior to Zry-4, a nickel-free Zry-2 (Zry-2 without nickel addition) was also created to compare with Zry-4's performance. The corrosion test in an aquatic and steam environment indicated the two alloys (nickel-free Zry-2 and Zry-4) picked up hydrogen markedly less than the original Zry-2 [3]. The experimental data shown in Fig. 2.3 demonstrates reduced hydrogen picked up

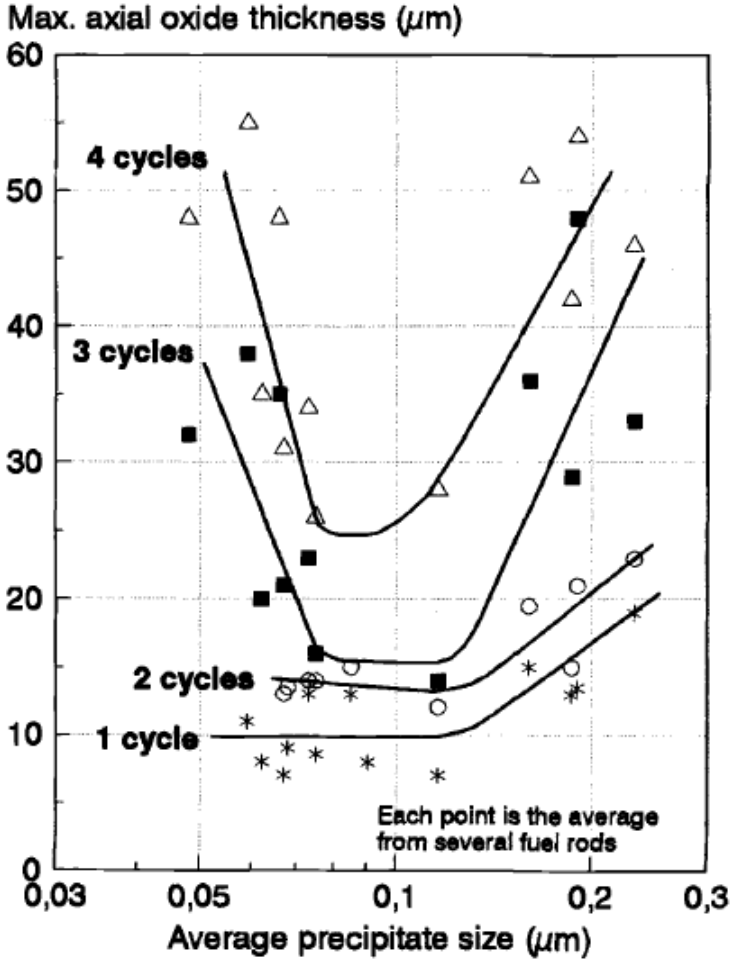

Figure 2.2: Effect of the SPP size on the corrosion resistance of a Zircaloy-2 fuel cladding. Samples have being served in a boiling water reactor (BWR) for different fuel cycles. This figure was reprinted from the Fig. 6 in Ref. [2].

by Zry-4 than the Zry-2. Fig. 2.3 also shows the heat treatment effect by comparing between a raw and a beta-quenched material. The heat treatment yielded different microstructure but did not significantly affect the hydrogen pick-up amount. This study also found that the corrosion resistance of the nickel-free Zry-2 was significantly lower than other two alloys at the high temperatures (above 430 °C). This poor corrosion resistance was attributed to the change of SPPs content due to removing of the nickel, while for Zry-4 the missing nickel was compensated by the iron thus maintained the corrosion resistance. The nickel-free Zry-2 was then dropped. Moreover, the study observed that the Zry-2 is more sensitive to hydrogen content in the water than the Zry-4; that is, the hydrogen absorption in Zry-2 increased with increased hydrogen concentration in the water [3]. This is one of the reasons that Zry-2 only serves in the boiling water reactors (BWRs), and Zry-4 can serve in both BWRs and the pressurized water reactors (PWRs) where corrosion is more severe due to higher operating

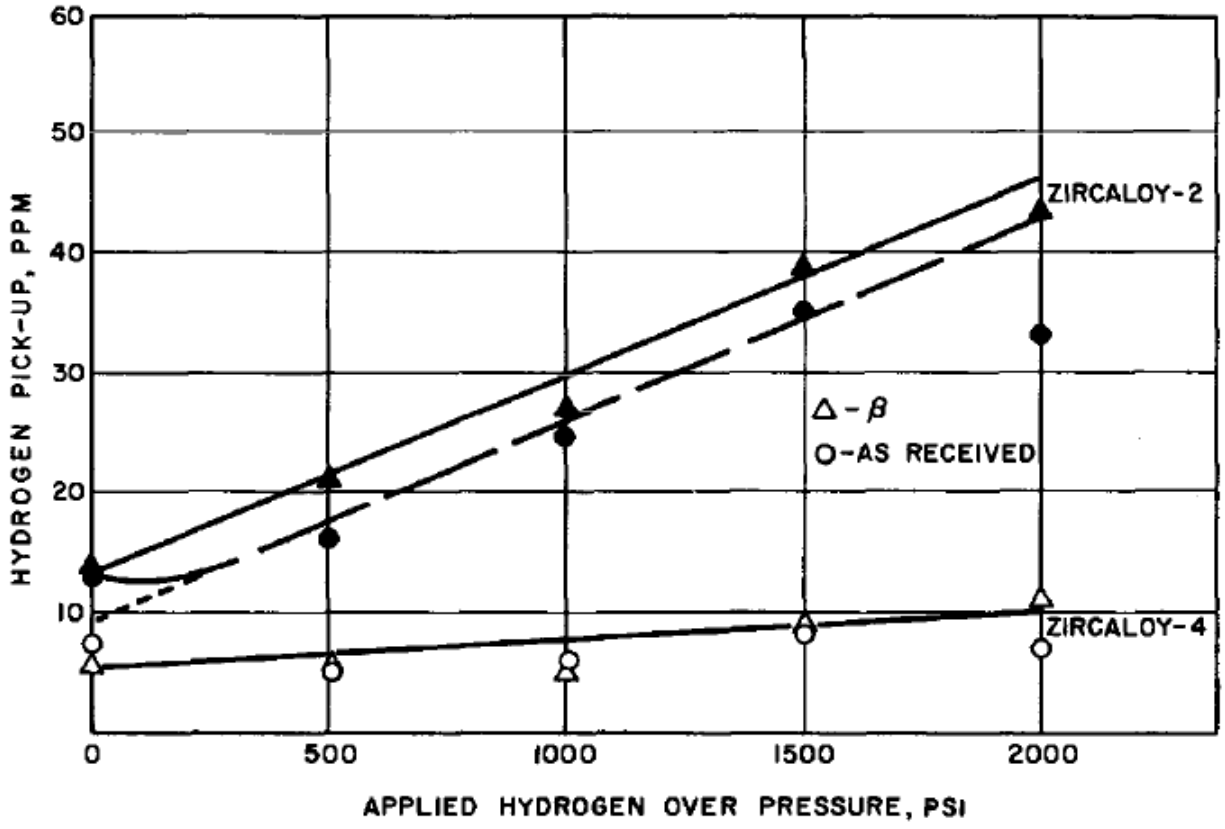

Figure 2.3: Hydrogen pickup amount by the Zry-2 and Zry-4 alloys. This figure was reprinted from the Fig. 16 in Ref. [3].

temperature.

The early research on zirconium alloys culminated in Zry-2 and Zry-4, which currently are the most common alloys applied in the nuclear fuel cladding. The requirement for nuclear grade Zry-2 and Zry-4 is specified by American Society for Testing and Materials (ASTM) standard with the unified numbering system (UNS) of R60802 and R60804, respectively. The nominal chemical composition of the two alloys is specified in Table 2 in Ref. [1], and is reproduced in Table 2.1 in this thesis. This doctoral research focuses on the Zircaloy-4 alloy. Other current studies focus on zirconium-niobium (Nb) binary alloys to extend the fuel lifetime, improve the performance under the loss-of-coolant accident (LOCA) and the reactivity-initiated accident (RIA) conditions. Also, development of advanced cladding alloys such as Zr-1Nb M5® and the Zr-1Nb-1Sn ZIRLO™ further reduced the corrosion rate and the hydrogen picked up amount [24].

2.1.2 Mechanical properties

A pure zirconium has two crystallography structures, hexagonal close-packed (hcp) and body-centered cubic (bcc) structure corresponding to the α and β zirconium phases, respectively. The literature review in this thesis only covers the properties of the α-Zr since it is the major phase in the range between the room temperature to the normal operating temperature of reactors.

The elastic modulus of a single zirconium crystal is anisotropic, which the c axis is stiffer than the a axis. The elastic modulus is 143 and 165 GPa along the a and the c of a single zirconium crystal, respectively. A complete set of data from 4 to 1135 K is given by Fisher and Renken [25]. These authors measured the elastic modulus of a single grain zirconium using the ultrasonic wave propagation. The primary slip system of the α-Zr is prism slip on $\{10\bar{1}0\}$ plane in $\langle 1\bar{2}10\rangle$ direction ($\langle a\rangle$ direction), while slip can also be activated on $\{11\bar{2}1\}$ or $\{10\bar{1}1\}$ planes along the $\langle c+a\rangle$ direction at higher temperatures [4]. Twinning is also an important deformation mechanism for zirconium and is usually activated before the slip. Common twinning system includes $\{10\bar{1}2\}\langle\bar{1}011\rangle$ and $\{1\bar{1}22\}\langle\bar{1}\bar{1}23\rangle$, depending on the applied stress direction.

The bulk properties of a Zircaloy significantly depend on the thermomechanical history and the alloying elements (listed in Table 2.1). Annealed zirconium has a low yield strength of 150 MPa at the room temperature. The addition of oxygen and tin enhances the yield strength to 300 MPa by solid solution strengthening. The SPPs, on the other hand, only causes a small increase in the strength. The thermomechanical treatment further increases the strength as well as retaining the ductility of the alloy. As aforementioned, details for most of the treatment procedure are proprietary. Therefore, this review focuses on the final

Table 2.1: Chemical composition requirement for Zry-2 (R60802) and Zry-4 (R60804). Reproduced from Table 2 in [1].

Element	UNS Number R60802 (Weight %)	UNS Number R60804 (Weight %)
Tin	1.2 to 1.7	1.2 to 1.7
Iron	0.07 to 0.2	0.18 to 0.24
Chromium	0.05 to 0.15	0.07 to 0.13
Nickel	0.03 to 0.08	...
Oxygen	0.09 to 0.16	0.09 to 0.16
Maximum impurities	(Weight %)	(Weight %)
Aluminum	0.0075	0.0075
Boron	0.00005	0.00005
Cadmium	0.00005	0.00005
Calcium	0.003	0.003
Carbon	0.027	0.027
Cobalt	0.002	0.002
Copper	0.005	0.005
Hafnium	0.0025	0.0025
Hydrogen	0.0025	0.0025
Magnesium	0.002	0.002
Manganese	0.005	0.005
Molybdenum	0.005	0.005
Nickel	...	0.007
Niobium	0.01	0.01
Nitrogen	0.008	0.008
Silicon	0.012	0.012
Tungsten	0.01	0.01
Titanium	0.005	0.005
Uranium	0.00035	0.00035

achieved properties for Zircaloy which meets the ASTM nuclear-grade standard.

The commonly accepted treatment is cold-worked stress-relieved (CWSR) and recrystallized (RXA) for Zry-4 and Zry-2, respectively. The different process between the two alloys is to overcome the severe nodular and uniform corrosion in BWRs and PWRs environment. As discussed in the last section, the different SPPs distribution affects the corrosion resistance for different corrosion mechanism. The cold-rolled process generates a strong anisotropic grain orientation (texture) such that the majority of zirconium grains have their c-axis reside within the normal-transverse plane and tilt 30-40° toward the transverse direction (TD), as shown in Fig. 2.4. The texture of a sample can be measured using the X-ray diffraction (XRD) pole figure analysis. A schematic example is shown in Fig. 2.4 while a real measurement of our samples is shown in Fig. 3.1 in the Experiment section. The distribution of the basal plane in the pole figure can be quantified using the Kearns factor [26], which describes the texture using the effective number of grains with their basal poles aligned along the sample axes. The sample axes can be TD, RD, and ND as shown in Fig. 2.4. The value of Kearns factor is calculated using [27],

$$f_{\mathrm{RD}} = \frac{1}{N}\int_0^{\pi/2}\int_0^{2\pi} I(\chi,\eta)\sin^3(\chi)\cos^2(\eta)d\eta d\chi \tag{2.1a}$$

$$f_{\mathrm{TD}} = \frac{1}{N}\int_0^{\pi/2}\int_0^{2\pi} I(\chi,\eta)\sin^3(\chi)\sin^2(\eta)d\eta d\chi \tag{2.1b}$$

$$f_{\mathrm{ND}} = \frac{1}{N}\int_0^{\pi/2}\int_0^{2\pi} I(\chi,\eta)\sin(\chi)\cos^2(\chi)d\eta d\chi \tag{2.1c}$$

where f_i is Kearns factor with i represents the sample axes. $I(\chi,\eta)$ is the measured basal pole intensity. χ and η are the polar and the azimuthal angle, respectively. N is the total intensity counts of a pole figure,

$$N = \int_0^{\pi/2}\int_0^{2\pi} I(\chi,\eta)\sin(\chi)d\eta d\chi \tag{2.2}$$

The f_i value for a CWSR Zry-4 were measured to be equal to 0.59-0.65 in the ND, 0.27-0.3 in the TD and 0.07-0.14 in the RD [13, 28]. The f_i value for an RXA Zry-2 is 0.887 in the

ND, 0.101 in the TD and 0.012 in the RD, indicating a more anisotropic texture than the CWSR Zry-4. The bulk property of an hcp polycrystal material can be estimated using the Kearns factor if it is assumed the contribution from a grain group of specific orientation to a bulk property is proportional to their volume fraction. This provides an approximate relationship between the single crystal and the polycrystal properties. This relationship was derived by Tempest [29],

$$P_i^{\text{Calc}} = f_i P_c + (1 - f_i) P_a \tag{2.3}$$

where P_i^{Calc} is the calculated bulk property along the sample axes i. P_a and P_c are the property of a single hcp crystal along the a and the c-axis, respectively. Eqn. (2.3) was

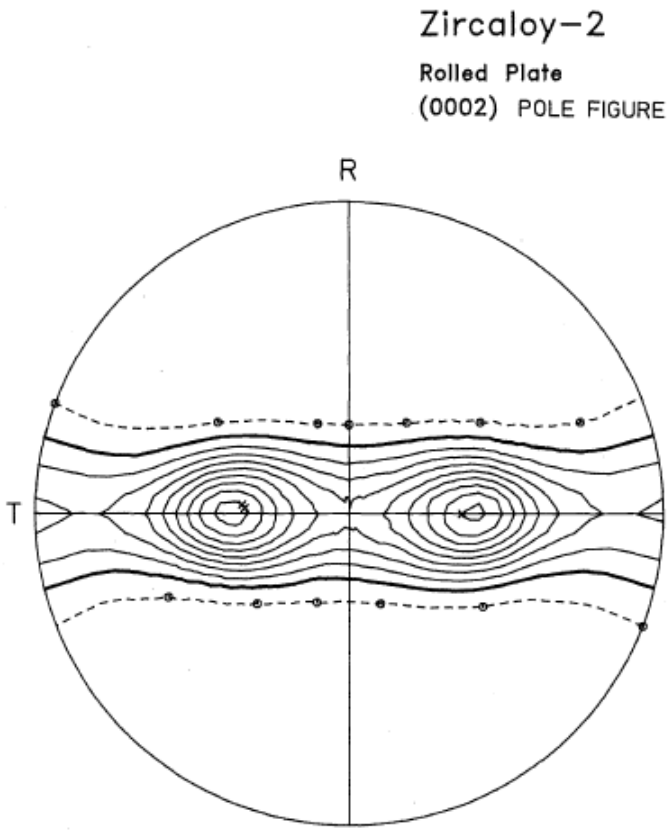

Figure 2.4: A (0002) basal pole figure of a cold-rolled Zry-2 plate reprinted from Fig. 7-13 in [4]. R and T indicate the rolling direction (RD) and the transverse direction (TD), respectively. The normal direction (ND) is perpendicular to the page. The dotted line has half of the intensity of the thick contour line. Each thin contour line indicates an increase of half of the intensity. This figure shows the basal plane distribution of the Zry-2 sample, where most of the grains have their c-axis tilted $\sim 40^\circ$ from the ND to the TD.

proved to be valid when estimated the thermal expansion coefficient of a polycrystal Zry-4 material. However, it is clear that mechanical properties, such as the yield strength and the elastic modulus, cannot be predicted using this simple relationship since the mechanical behavior of a polycrystal is more complex than the average behavior of many single crystals.

Mechanical properties of the material studied in this research were provided by certified manufacturers. The Zircaloy plates and tubes were purchased from ATI Specialty Alloys and Components and Westinghouse Electric Company, respectively. The yield strength of Zry-4 is 467 and 381 MPa at 23 °C along the TD and RD, respectively. The bulk elastic modulus of Zry-4 is 99.3 GPa.

2.2 State of hydrogen in zirconium

Zircaloy cladding reacts with the water coolant during service, forming zirconium oxide and releasing hydrogen via,

$$\mathrm{Zr}+2\mathrm{H_2O} \rightarrow \mathrm{ZrO_2} + 4\mathrm{H} \tag{2.4}$$

The radiolytic decomposition of the water coolant also creates hydrogen,

$$2\mathrm{H_2O} \rightarrow \mathrm{H_2O_2} + \mathrm{H_2} \tag{2.5}$$

Most of the hydrogen was taken away by the water coolant flow, while $\sim 15\%$ of the hydrogen passed through the zirconium oxide layer and reached the fresh cladding matrix [30]. The accumulated hydrogen content at the end-of-life was in a range of 300 to 600 weight parts per million (wt ppm), depending on the fuel burn-up [31].

Upon reaching the fresh matrix, hydrogen dissolves in the α-Zr phase, occupying the interstitial sites of the hcp lattice and transformed into a zirconium hydride phase once the solubility limit is reached. The characteristic of hydrogen in the solid solution and as the hydride phase, as well as their influence on the zirconium matrix, is reviewed in the following sections. A binary zirconium-hydrogen phase diagram [5] is shown in Fig. 2.5 as a reference.

2.2.1 Hydrogen in the zirconium solid solution

Upon reaching the fresh matrix, hydrogen dissolves in the α-Zr solid solution and occupies the interstitial sites of the hcp zirconium lattice. Experimental studies done by Narang *et al.* [32], Khoda-Bakhsh and Ross [33] found the hydrogen preferentially occupied the tetrahedral sites of the lattice. Using *ab initio* calculation, Domain *et al.* [6] and Burr *et al.* [34] obtained a 5.5-8.3 kJ mol^{-1} energy preference for hydrogen in the tetrahedral site compared to the octahedral sites, supporting the experimental result. However, later work by Christensen *et al.* [35] pointed out that the *ab inito* result could depend on the chosen energy criterion. Christensen *et al.* found that at low temperatures (close to the room temperature) the two sites have similar occupation energy and the preference of hydrogen on

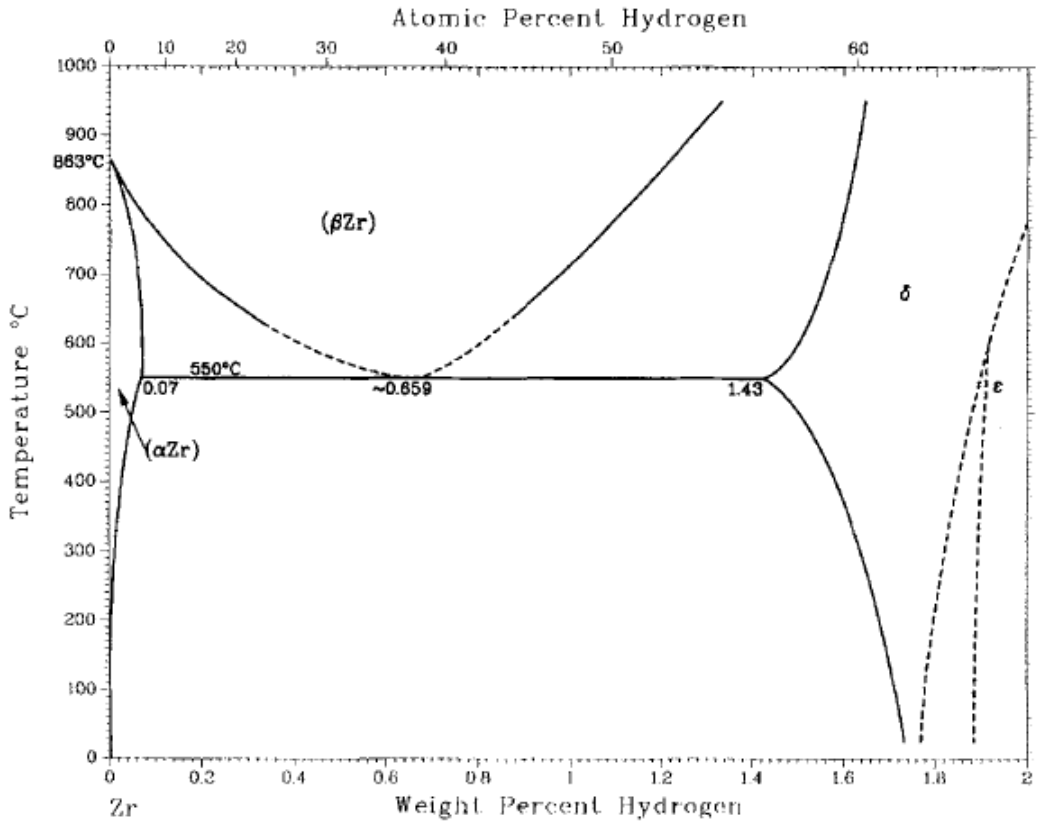

Figure 2.5: A zirconium-hydrogen binary phase diagram reprinted from Fig. 1 in Ref. [5]. The γ-phase was regarded metastable by the author and was absent in this diagram. We should note that the author did not indicate how the equilibrium state was obtained, as the hydrogen solvus did exhibit a large hysteresis gap between the cooling and the heating solvus (see Section 1.3).

the tetrahedral site increase as the temperature increased; nearly 94% of hydrogen occupied the tetrahedral site at 600K. The location of the octahedral and the tetrahedral site for hydrogen interstitial in the zirconium lattice is schematically shown in Fig. 2.6.

The hydrogen in the interstitial site causes a lattice dilatation, which is linearly proportional to the amount of hydrogen in the solid solution, following the Vegard's law [7]. MacEwen *et al.* [7] measured this dilatation using the time-of-flight (TOF) neutron diffraction on an annealed zirconium charged with deuterium. Their measurement is shown in Fig. 2.7. These authors obtained values of 4.85 and 2.86 $\mu\epsilon$ per wt ppm of hydrogen along the c and the a-axis of the zirconium lattice, respectively. The other common way to represent

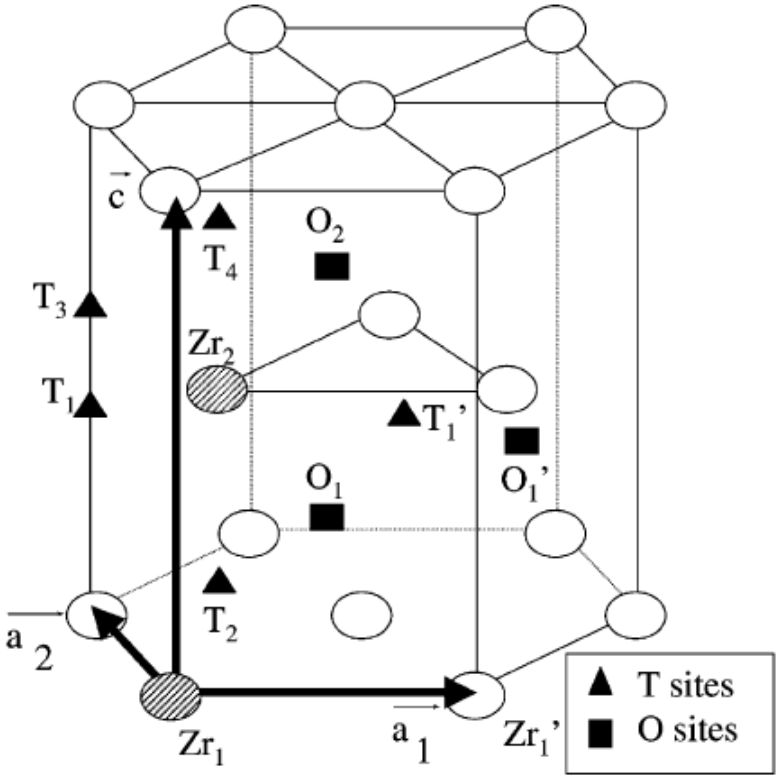

Figure 2.6: Schematically shows the location of the interstitial sites in an hcp zirconium lattice. T and O represent the tetrahedral and the octahedral site, respectively. The prime indicates the same site in a neighboring unit cell. This figure was reprinted from Fig. 1 in Ref. [6].

this dilatation is to use the partial molal volume,

$$\bar{V}_{\mathrm{H}} = \left.\frac{\partial V}{\partial n_{\mathrm{H}}}\right|_{T,P,n_j} = N_0 \Delta v \tag{2.6}$$

$\bar{V}_{\mathrm{H}}$ is the partial molar volume of hydrogen defined as the change of the matrix volume per mole of hydrogen. V is the volume of the metal matrix, n_H is the mole number of dissolved hydrogen, N_0 is the Avogadro's number, and Δv is the change of metal volume per dissolved hydrogen atom. Remarkably, Baranowski *et al.* [36] and Peisl [37] have examined a wide

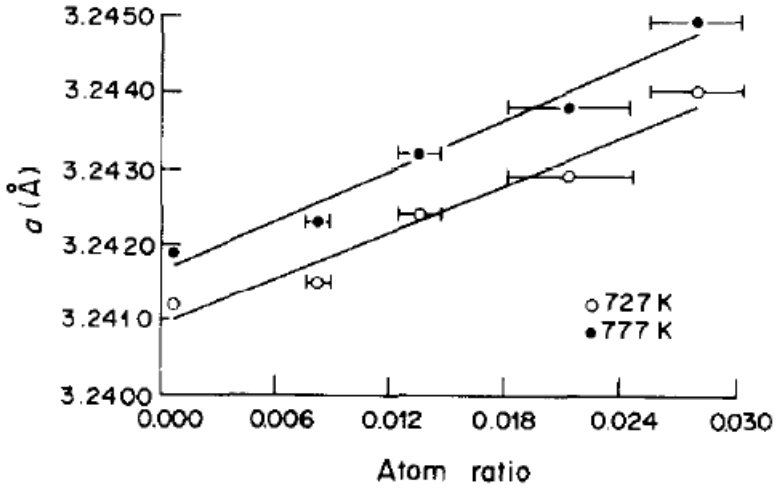

(a) a-axis

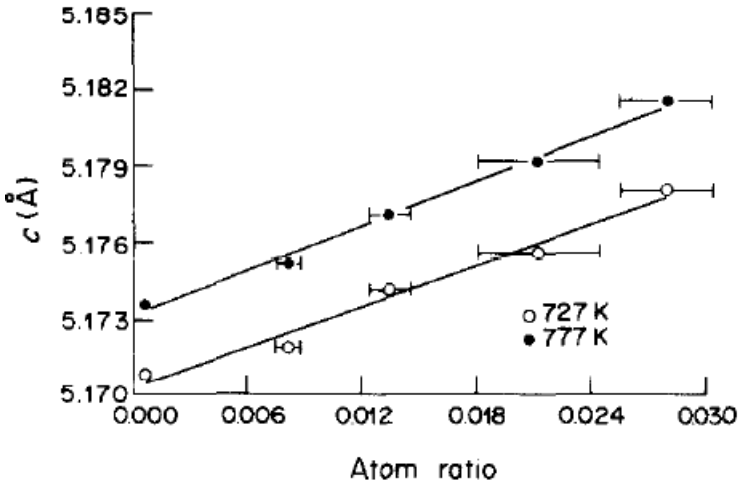

(b) c-axis

Figure 2.7: Zirconium lattice parameter as a function of deuterium atomic fraction. These figures are reprinted from Fig. 2 and Fig. 3 in Ref. [7].

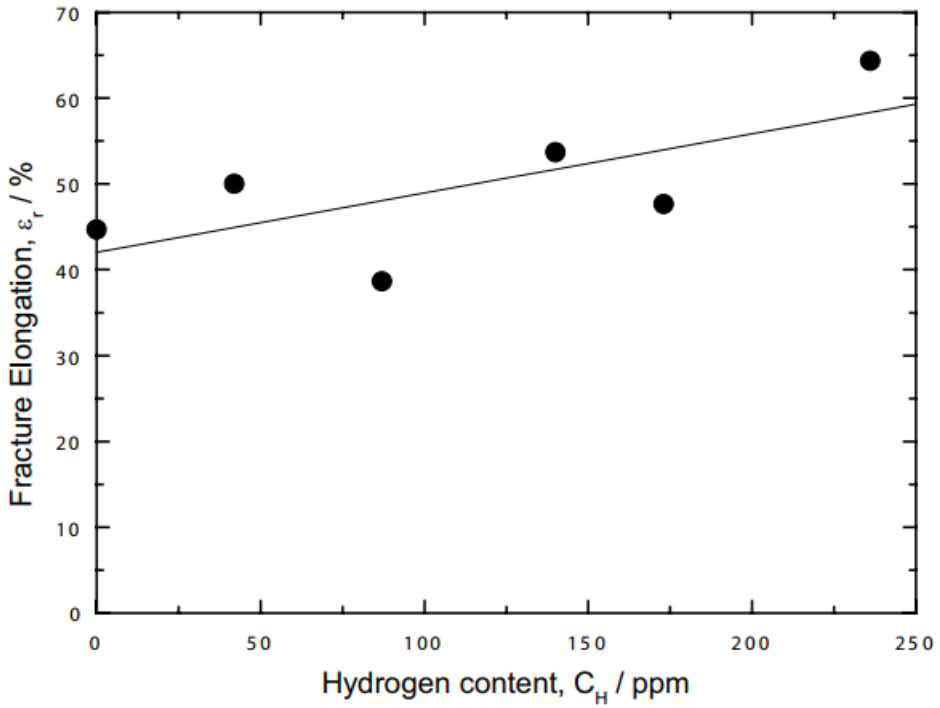

Figure 2.8: The fracture elongation of a pure zirconium at 400 °C as a function of the hydrogen concentration in the solid solution. This figure was reprinted from Fig. 7 in Ref. [8].

range of bcc, fcc and hcp metals and observed that the Δv is nearly a constant value of $2.9\mathring{A}^3$. This is known as "Peisl's rule". MacEwen *et al.*'s measurement also obtained an close value of $\Delta v = 2.78\ \mathring{A}^3$, yielding the hydrogen partial molar volume in the α-zirconium phase of $\bar{V}_{\mathrm{H}}^{\alpha} = 1.67 \times 10^{-6}\ \mathrm{m^3\,mol^{-1}}$.

The interstitial hydrogen also affects the mechanical properties of the zirconium matrix. The experimental work by Yamanaka *et al.* [8] showed that the shear, elastic modulus, and hardness of zirconium decreased with increased hydrogen content in the solid solution. By calculating the electronic structure of the zirconium hydrogen solid solution using the first-principles molecular orbital method, the authors believed that the interstitial hydrogen removed the 4d electron from the metallic bonding to form the zirconium-hydrogen bond, thus degraded the zirconium properties. Surprisingly, the ductility of the zirconium sample increase with increasing amount of hydrogen in the solid solution as shown in Fig. 2.8. This differs from the commonly known hydrogen embrittlement behavior in the steel, also implies the solute hydrogen promotes plastic deformation of the zirconium. This conclusion

is supported by research done by Hong *et al.* [38] that achieved superplasticity (with the engineering strain of 133%) in a pure zirconium by cyclically charging hydrogen under an isothermal condition.

2.2.2 The zirconium-hydride phase

The hydrogen combines Zr to from zirconium-hydride phase once the hydrogen concentration exceeds the solubility limit. Early XRD and metallographic analysis have identified three distinct zirconium hydride phases, which are δ, γ and ϵ phase [39,40]. The δ-hydride is a disordered fcc lattice of the CaF_2 type with tetrahedral sites being occupied by the hydrogen atoms. The δ-hydride phase has an extend stoichiometry of $ZrH_{1.59-1.66}$, while $ZrH_{1.66}$ is the most commonly observed. The γ-hydride has an ordered face centred tetragonal (fct) lattice with the c/a ratio > 1. The γ-hydride phase has an one-to-one ratio of hydrogen to the zirconium atoms (ZrH). ϵ-hydride is observed at higher hydrogen content exists over the composition range of $ZrH_{1.67-2}$; this phase also has an fct structure but with the c/a ratio < 1. Schematic unit cell structures of the three hydride phases created by Olsson *et al.* [9] is shown in Fig. 2.9. A relatively recent TEM study by Zhao *et al.* [41] identified a fourth metastable hydride phase, designated as ξ. ξ has a probable stoichiometry of Zr_2H, and belongs to the trigonal crystal system with a space group of P3m1. Interestingly, speculation on the existence of a fourth hydride phase was raised by Bailey [17] and Carpenter [42] 30 years ago, when they tried to identify small needle-like hydride precipitates during the early

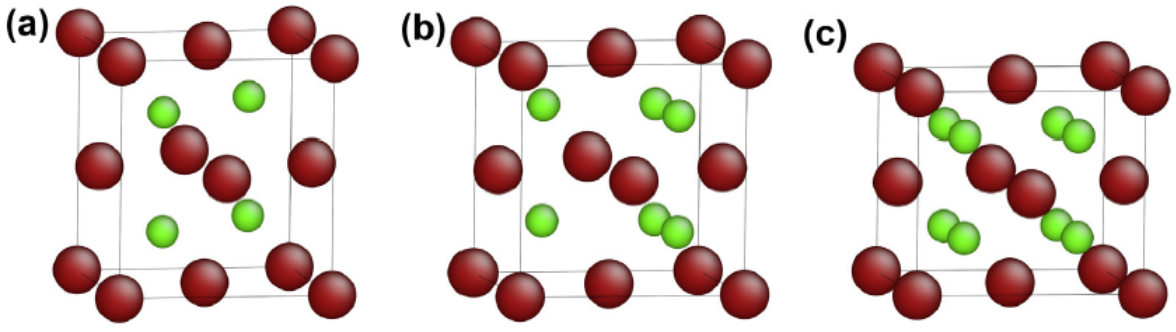

Figure 2.9: The unit cell structures of (a) γ, (b) δ and (a) ϵ hydride phase reprinted from Fig. 2 in Ref. [9].

precipitation stage.

Among the four hydride phases, only δ and ϵ are considered stable. The stability of γ has been debated [43] but currently believed to form under certain conditions [39]. The ξ is regarded as a transition phase during hydride precipitation [41]. Bair *et al.* [44] recently studied the nucleation and growth of the δ-hydride phase using the phase-field simulation. In their study, the formation of γ and ξ phase were also considered. These authors observed that γ and ξ formed as an intermediate transformation path way to the final stable δ phase; the γ had more influence on the final δ morphological shape than the ξ. Bair *et al.*'s work was the first phase-field study on zirconium-hydride system that included more than one hydride phase. The result suggests that γ and ξ are intermediate phases during the nucleation and growth of hydride precipitate, and have a significant impact on the final hydride shape. Phase-field simulations are based on the free energy function and the interfacial energy chosen, as discussed in Ref. [44]. Only the δ-hydride phase is considered in this thesis since it is a commonly accepted stable phase at the room temperature and at the practical service temperature for a fuel cladding.

The δ-phase has high strength but is brittle. The mechanical data of pure $ZrH_{1.66}$ has a broad range. Puls *et al.* [45] obtained a room temperature yield strength of 990 MPa, significantly differed than value 250 MPa obtained by Barraclough and Beevers [40]. Puls [46] attributed this disagreement to the hydrogenation procedure, suggesting that the procedure used by Barraclough and Beevers could generate a great number of microscopic cracks. The elastic modulus of the δ phase determined by Syasin *et al.* [47] ranged from 80-85 GPa at the room temperature and was 100 GPa measured by Kerr *et al.* [48] using the in situ synchrotron diffraction. Lin *et al.* [12] also utilized the synchrotron diffraction and obtained values of 66-75 GPa at 200 °C. The value 132 GPa measured by Yamanaka *et al.* [49] using the X-ray photoelectron spectroscopy at the room temperature is the highest among these experimental studies. Olsson *et al.* [9] carried out an *ab initio* calculation for the elastic constants C_{ijkl} and elastic modulus of the δ phase. These authors obtained an elastic modulus value of 127 GPa, close to the one measured by Yamanaka *et al.* The compliance tensor for the δ phase can also be found in Olsson *et al.*'s work.

The crystallographic orientation relationships between the δ hydride and the α zirconium

are [50],

$$\{111\}_\delta \parallel \{0001\}_\alpha,\ \langle 1\bar{1}0\rangle_\delta \parallel \langle 11\bar{2}0\rangle_\alpha \tag{2.7a}$$

$$\{111\}_\delta \parallel \{10\bar{1}0\}_\alpha,\ \langle 1\bar{1}0\rangle_\delta \parallel \langle 11\bar{2}0\rangle_\alpha \tag{2.7b}$$

The transformation from hcp α-Zr to fcc δ-hydride has an associated volume expansion, creating an internal strain at the interface between the two phases. Carpenter [51] calculated the unconstrained misfit (strain value equal to full expansion of the δ hydride without being constrained by the surrounding matrix) using the relationship in Eqn. (2.7) and obtained strain values of 0.072, 0.0458 and 0.0458 along the [0001] (c-axis), [11$\bar{2}$0] (a-axis) and [1$\bar{1}$00] directions, respectively. This misfit strain corresponded to an unconstrained volume change of 17.2% after transformed from α to the δ phase. The hydrogen partial molar volume in δ-phase $\bar{V}_{\mathrm{H}}^{\delta}$ was calculated as 1.4×10^{-6} m^3 mol^{-1} which is smaller than the hydrogen partial molar volume in α-Zr solution ($\bar{V}_{\mathrm{H}}^{\delta} = 1.4\times10^{-6}$ m^3 mol^{-1}) [7]. Singh *et al.* [52] modified Carpenter's calculation by including the temperature dependence,

$$\varepsilon_a^{\mathrm{misfit}} = 0.0371 + 2.3111\times10^{-5}T \tag{2.8a}$$

$$\varepsilon_c^{\mathrm{misfit}} = 0.06463 + 1.9315\times10^{-5}T \tag{2.8b}$$

$\varepsilon_i^{\mathrm{misfit}}$ is the unconstrained misfit strain along the i axis of a zirconium lattice and T is the temperature in K. This transformation strain is greater than the macroscopic yield strain of the surrounding matrix. Therefore, the matrix was plastically deformed locally at the interface of the two phases, allowing the matrix to accommodate the hydride precipitate. Dislocations surrounded the hydride particles were commonly observed [17, 53]. Puls [54] suggested that approximate 40-50% of this accommodation strain energy was relaxed by the plastic deformation. The most recent measurement on the accommodation strain was done by Barrow *et al.* [53] using the nanobeam electron diffraction technique. These authors measured the constrained strain for a nano-hydride particle in a Zry-2 matrix and obtained strain values of 0.055, 0.031 and 0.005 along the [0001] (c-axis), [11$\bar{2}$0] (a-axis) and [1$\bar{1}$00] directions, respectively, suggesting the nano-hydride had a needle shape. They also found this accommodation strain decayed quickly away from the interface, extending only $\sim$ 50

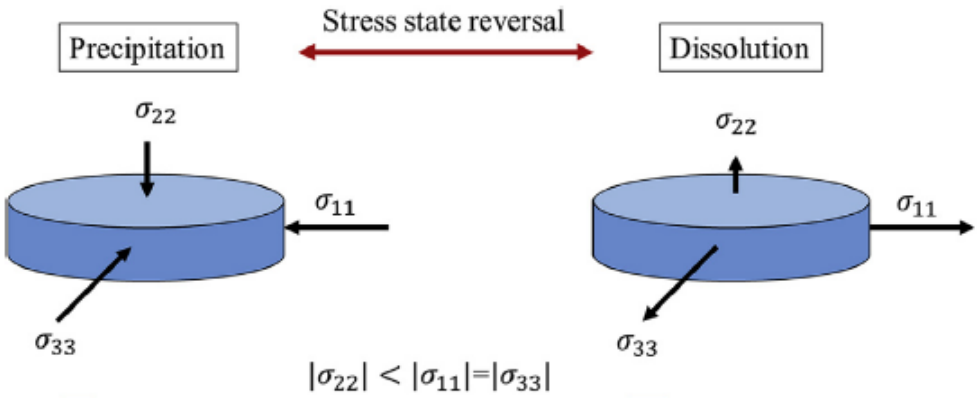

Figure 2.10: Showing the schematic internal stress state within a microscopic hydride particle when the hydride is (a) precipitating and (b) dissolving. This figure was reprinted from Fig. 9 in Ref. [10].

nm from the interface to the matrix.

The accommodation strain generates the corresponding internal stress within the hydride particle. Cinbiz *et al.* [10] qualitatively illustrated the internal stress state by studying the change of $\delta(111)$ plane spacing for both circumferential and radial hydride particles using the synchrotron XRD. Their result indicated the internal stress state in the macroscopic hydride was a collective result of microscopic hydride particles, and was independent of the macroscopic hydride orientation. The internal stress within the hydride is in compression when precipitating, and is in tension when dissolving, while the in-plane stress is always larger than the out-of-plane stress. The stress state is depicted in Fig. 2.10.

2.3 Hydrogen solubility in Zircaloy

Hydride precipitation begins when the hydrogen content exceeds the solubility limit. The hydrogen solubility is thus an important topic since it predicts the hydride phase fraction for an amount of hydrogen at a given temperature. The solubility limit, also known as the hydrogen solvus, is therefore essential when investigating the influence of hydride on the cladding performance. The hydrogen solvus is defined as the hydrogen concentration in solution at equilibrium with the hydride phase at a given temperature. It is also referred to the hydrogen terminal solid solubility (TSS). The TSS is generally described by the terminal

solid solubility of dissolution (TSSd) and the terminal solid solubility of precipitation (TSSp) for a system under heating and cooling, respectively. In a closed system with a constant hydrogen content, the TSSd represents the temperature when the last hydrides have dissolved, and the TSSp represents the temperature when the first hydride starts to form. This thesis primarily focuses on the hydrogen solvus in a CWSR Zircaloy-4 matrix.

2.3.1 Hydrogen solvus model

An important aspect of hydrogen solvus is the reproducible hysteresis between the TSSd and TSSp. A commonly referred hydrogen solvus model is based on the accommodation energy between the hydride and the matrix phase. The accommodation energy model considers both the elastic and plastic deformation energy. Puls developed a well-known accommodation energy model that primarily focused hydrogen solvus in zirconium alloys [54]. In this model, the primary cause of the hysteresis is the lattice misfit strain between α-Zr and δ-hydride phase as discussed in Section 2.2.2. The true equilibrium hydrogen solvus without the hysteresis is defined as C_{H}^{0}. The lattice misfit strain induces accommodation strain energy to the system. The system accommodates this energy differently upon cooling and heating, shifting C_{H}^{0} and creates the hysteresis. Puls assumed that the unconstrained accommodation energy $\overline{W}_{\mathrm{uncon}}^{a}$ was greater than the elastic constrained accommodation energy $\overline{W}_{\mathrm{el}}^{a}$ by an unrecoverable amount of plastic energy ΔH_p lost on cool-down,

$$\overline{W}_{\mathrm{uncon}}^{a} = \overline{W}_{\mathrm{el}}^{a} + \Delta H_p \tag{2.9}$$

Puls then described the hydrogen TSSp as,

$$C_{\mathrm{TSSp}}^{\mathrm{Con}} = C_{\mathrm{H}}^{0}\exp\Big(\frac{\overline{W}_{\mathrm{uncon}}^{a}}{xRT}\Big) = C_{\mathrm{H}}^{0}\exp\Big(\frac{\overline{W}_{\mathrm{el}}^{a} + \Delta H_p}{xRT}\Big) \tag{2.10}$$

where $C_{\mathrm{TSSp}}^{\mathrm{Con}}$ is the constrained TSSp and C_{H}^{0} is the true equilibrium solvus. x is the number of moles of hydrogen per mole of the hydride, R is the ideal gas constant and T is the temperature in K. Puls further assumed that the same amount of unrecoverable energy ΔH_p must be re-supplied to dissolve the hydride phase on the heat-up, but the elastic energy $\overline{W}_{\mathrm{el}}^{a}$

is available to aid the dissolution. The TSSd was described as,

$$C_{\mathrm{TSSd}}^{\mathrm{Con}} = C_{\mathrm{H}}^{0}\exp\Big(\frac{\overline{W}_{\mathrm{el}}^{a} - \Delta H_p}{xRT}\Big) \tag{2.11}$$

The theoretical TSSd was shifted to higher temperature compared with the theoretical TSSp. $\overline{W}_{\mathrm{uncon}}^{a}$ was calculated as 4.911 kJ mol^{-1} for a plate δ-hydride particle on the zirconium basal plane using Eshelby's method with unconstrained misfit strains given by Carpenter [51]. Using Eqn. (2.11) to compare with Slattery's TSSd data [55], Puls obtained a ΔH_p value of 2.23 kJ mol^{-1} for a Zry-4 sample. Puls then concluded that approximate 40-50% of the unconstrained accommodation energy for the hydride phase was lost to the plastic work.

However, in a later work, Puls [56] indicated that Eqn. (2.9) could be in error. This statement based on Lee *et al.*'s [57] calculation for a spherical precipitate in an isotropic matrix, where Lee *et al.* found that the total accommodation energy was only 0.07 times of the unconstrained accommodation energy,

$$\frac{\overline{W}_{\mathrm{el}}^{a} + \Delta H_p}{\overline{W}_{\mathrm{uncon}}^{a}} = 0.07 \tag{2.12}$$

. We note that these authors used a yield stress value and the isotropic misfit strains in an ideal plastic matrix. Comparing Eqn. (2.11), Eqn. (2.10) and Eqn. (2.12), Puls expected that the $C_{\mathrm{TSSd}}^{\mathrm{Con}} \simeq C_{\mathrm{H}}^{0}$ since $\overline{W}_{\mathrm{el}}^{a} - \Delta H_{\mathrm{p}}$ was very small, and the hysteresis between the $C_{\mathrm{TSSp}}^{\mathrm{Con}}$ and $C_{\mathrm{TSSd}}^{\mathrm{Con}}$ was more closely related to the nucleation barrier and the interface energy on precipitation. This assumption was soon found to be in error by Puls [56] after examining the solubility data of several metal-hydrogen systems. The $C_{\mathrm{TSSd}}^{\mathrm{Con}}$ was not close to C_{H}^{0} and the observed hysteresis was much larger than simply the result of a nucleation barrier.

Flanagan *et al.* [58] published a comprehensive discussion on the first-order phase transformation for a broad range of metal-hydrogen systems which exhibited hysteresis characteristic. These authors concluded that a common feature of these metal-hydrogen systems was the necessity of a finite driving force before the phase transformation. This finite driving force induced a unidirectional finite movement of the phase boundary, causing hysteresis, and was balanced by the production of the internal entropy. The dissipation of the internal work by

the entropy did not release heat to the surrounding environment. Flanagan *et al.* [58] also stated that for the accommodation energy models to be valid, the model should (1): include different accommodation energy for a single hydride particle in the zirconium matrix on cool-down as compared with the system on heat-up. (2): The partial differential accommodation energy with respect to the hydrogen composition should be independent of the hydrogen composition. Despite these insufficiencies, the accommodation energy model was largely referred by literature which studied the hydrogen-zirconium system [12, 13, 28, 59, 60]. The solvus hysteresis for the hydrogen in zirconium alloys is a combination effect of elastic and plastic accommodation energy and the undetected entropy during the phase transformation. The entropy is likely the dominant cause.

2.3.2 Influence of external load on hydrogen solvus

The study of the effect of stress on hydrogen solvus has arisen because the concerns of stress-induced hydride fracture [61] and the delayed hydride cracking for the post-storage fuel cladding [46, 62]. Flanagan and Mason [11] derived a simple thermodynamic relation to describe the effect of stress on the chemical potential of a system. They concluded that the solvus would be unaffected by the stress if the hydrogen partial molar volume for the hydride and the matrix phase was the same, which was the case of a miscibility gap system. For a structural transformation system such as zirconium-hydrogen, the change of the chemical potential is proportional to the stress value and the difference of the hydrogen partial molar volume between the hydride and the matrix phase. As pointed out by MacEwen *et al.* [7], the difference between $\bar{V}_{\mathrm{H}}^{\alpha}$ and $\bar{V}_{\mathrm{H}}^{\delta}$ is at most $-0.27\times10^{-6}\ \mathrm{m^3\,mol^{-1}}$. This suggested that the effect of external stress on the hydrogen solvus in the α-zirconium solution is insignificant.

However, because the chemical potential of hydrogen was reduced by the stress, hydride precipitation would be affected by the presence of a non-uniform stress field. Assuming the hydriding occurred through the reaction,

$$\frac{1}{2}\mathrm{H_2}\ (1\ \mathrm{atm}) + \frac{1}{b-a}\mathrm{ZrH}_a \rightarrow \frac{1}{b-a}\mathrm{ZrH}_b \tag{2.13}$$

where a is the hydrogen solubility in the Zr solid solution in equilibrium with the hydride phase, and b is the metal-to-hydrogen ratio of the hydride phase in equilibrium with hydrogen in the solid solution. The chemical potential of hydrogen was described by [11],

$$\Delta\mu_H^{\sigma>0} = \Delta\mu_H^{\sigma=0} - \frac{\sigma}{b-a}[\bar{V}_{\mathrm{H}}^{\delta} - (\bar{V}_{\mathrm{Zr}}^{\alpha} + a\bar{V}_{\mathrm{H}}^{\alpha})] \tag{2.14}$$

where μ_H is the chemical potential of hydrogen, σ is the external stress and $\bar{V}_{\mathrm{Zr}}^{\alpha}$ is the zirconium partial molar volume in the α-zirconium phase. Eqn. (2.14) is schematically shown in Fig. 2.11. We note here that Eqn. (2.14) does not account for the anisotropic volume change which results from different lattice structure between the α-Zr and the δ-hydride phase. Later treatment by Puls [54] considered the stress contribution by including the hydride transformation strain rather than the hydrogen partial molal volume. Puls's model will also be discussed in this section. In Fig. 2.11, the hydride phase precipitates if the hydrogen chemical potential in an unstressed area is greater or equal to the hydrogen chemical potential in a stressed area, that is, the hydrogen concentration in the unstressed area is greater or equal to a'. The hydrogen solubility is still a in both stressed and unstressed

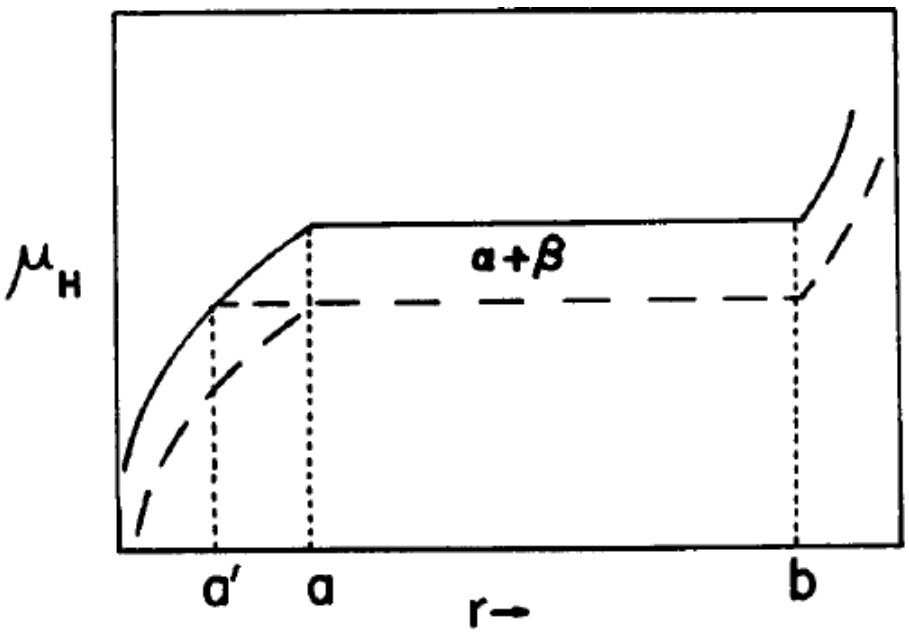

Figure 2.11: The chemical potential of hydrogen μ_H reprinted from Fig. 1 in Ref. [11]. The solid and the dashed line represents $\mu_H^{\sigma=0}$ and $\mu_H^{\sigma>0}$, respectively. r is the hydrogen concentration at equilibrium.

areas; as previously discussed the external stress does not affect the hydrogen solubility.

Puls [54,63] also considered the external stress effect in his accommodation energy model,

$$C_{\mathrm{TSSp}}^{\mathrm{Con},\sigma} = C_{\mathrm{H}}^{0}\exp\Big(\frac{\overline{W}_{\mathrm{uncon}}^{a}}{xRT}\Big)\exp\Big(\frac{xp^{\mathrm{h}}\cdot\bar{V}_{\mathrm{H}}^{\alpha} - \bar{V}_{\mathrm{Zr}}^{\alpha}\sigma_{ij}\cdot\varepsilon_{ij}^{T}}{xRT}\Big) \tag{2.15}$$

or

$$C_{\mathrm{TSSp}}^{\mathrm{Con},\sigma} = C_{\mathrm{TSSp}}^{\mathrm{Con}}\exp\Big(\frac{xp^{\mathrm{h}}\cdot\bar{V}_{\mathrm{H}}^{\alpha} - \bar{V}_{\mathrm{Zr}}^{\alpha}\sigma_{ij}\cdot\varepsilon_{ij}^{T}}{xRT}\Big) \tag{2.16}$$

where σ_{ij} is the applied stress, p^{h} is the hydrostatic stress and ε_{ij} is the unconstrained transformation strain for α-Zr transforms to δ-hydride. Eqn. (2.16) differs than Eqn. (2.10) by an extra exponential term, which describes the contribution of applied stress on the net energy while transferring hydrogen out or into the solid solution by forming or dissolving the hydride phase. For TSSd solvus, the stress contribution is,

$$C_{\mathrm{TSSd}}^{\mathrm{Con},\sigma} = C_{\mathrm{TSSd}}^{\mathrm{Con}}\exp\Big(\frac{xp^{\mathrm{h}}\cdot\bar{V}_{\mathrm{H}}^{\alpha} - \bar{V}_{\mathrm{Zr}}^{\alpha}\sigma_{ij}\cdot\varepsilon_{ij}^{T}}{xRT}\Big) \tag{2.17}$$

. Puls [63] evaluated the magnitude of the stress contribution on the net energy by considering a highly-stressed area at a crack tip, where the highest stress component can reach $\sim$ 1860 MPa at 250 °C. The author obtained a change of net energy by only 129 $\mathrm{J\,mol^{-1}}$ even at this high stress. Comparing with the $\overline{W}_{\mathrm{uncon}}^{a}$ value of 4.911 $\mathrm{kJ\,mol^{-1}}$, this change is negligible. This result agrees with Flanagan and Mason's [11] conclusion, that the equilibrium hydrogen solubility is unaffected by an applied stress. Puls made a similar conclusion after reviewed the most recent DHC model [46,63,64]. The DHC is driven by hydrogen flux flow from bulk region toward a stress concentrator, such as the crack tip, inducing the crack propagation. Puls stated that for this case because the hydrogen solvus at the bulk and the crack tip were unaffected by the stress, there would be no concentration gradient between the two regions. However, the hydrogen flux toward the crack tip would still occur, driven solely by the stress gradient. The hydrogen that arrived at the crack tip was immediately absorbed by the existing hydride phase because the equilibrium condition forced the solvus to remained unchanged. This process repeated, causing the growth of the hydride phase at the crack tip and the crack propagation, leading to DHC. For summary, there is a small

difference between the interpretation by Puls [46] and by Flanagan and Mason [11], but they lead to the same conclusions (1): the equilibrium hydrogen solvus is unaffected by the applied stress. Therefore, the stress gradient does not facilitate the hydrogen concentration gradient. (2): The stress gradient will still enhance hydride precipitation in the region with elevated tensile stress even without the presence of concentration gradient.

2.4 Experimental results of hydrogen solvus in Zircaloy

This thesis primarily focuses on the results for Zircaloy alloys. There have been many techniques applied to quantify the hydrogen solvus in Zircaloy, including diffusion equilibration [16], differential scanning calorimetry (DSC) [15, 60, 65–69], dilatometry [55, 70] and X-ray and neutron diffraction [28, 71]. The experimentally measured hydrogen solvus is commonly described by Arrhenius equation,

$$[H]^{\alpha} = A\exp\left(\frac{-Q}{RT}\right) \tag{2.18}$$

where $[H]^{\alpha}$ is the hydrogen concentration in the α-Zr solid solution, A is the temperature independent pre-exponential factor, R is the ideal gas constant, and T is the temperature in K. Q is an energy term which includes the change of hydrogen enthalpy, the elastic and plastic accommodation energy and the contribution by the applied stress. Table 2.2 summarizes the adopted techniques, experimental conditions and numerical results of several previous works.

Kearns [16] adopted the diffusion equilibrium method by welding a hydrided sample at the end of a much larger hydrogen-free sample. This diffusion couple was annealed for 10 days at 260 °C and 2 days at 525 °C in order to reach equilibrium; the equilibrium hydrogen concentration was measured at the other end of the hydrogen-free sample. The purpose was to avoid the supersaturation effect which caused the hysteresis behavior. Kearns's [16] result was regarded as the true-equilibrium hydrogen solvus since it did not associate with dissolution or precipitation of the hydride phase [54]. However, Puls [46] argued that since the true hysteresis is a reproducible effect that originated from the loss of free energy, it should occur no matter how slow the equilibrium status was approached. Puls, therefore,

suggested that Kearns data is more close to the TSSd solvus instead of a true equilibrium solvus. Data from other literature in addition to the Kearns result were associated with dissolution and precipitation of the hydride phase and were categorized into TSSd and TSSp solvus in Table 2.2. These solvus were obtained by performing the best-fit using Eqn. (2.18) on the experimental data. It can be seen in Table 2.2 that the pre-exponential factor A varies significantly but the Q only slightly differs for both TSSd and TSSp solvus except for Zanellato *et al.* [71] which has a higher Q_{d} and for Colas *et al.* [28] which has a 160 MPa applied stress and a lower Q_{p} value. The pre-exponential factor A includes the entropy contributions to the solvus other than the mixing entropy and could be determined using the thermodynamic data. Puls [46] has pointed out that when quantitatively comparing the hydrogen solvus value it is necessary to include the A otherwise the result is non-physical. However, it should be kept in mind that only Q is affected by the temperature-dependent response. This response could be further affected by an applied stress as implied by Ref. [63] where Puls evaluated the magnitude of the stress effect on the Q. A different treatment was done by Shi *et al.* [73] where the author fixed the A as a constant value obtained from previous result and fit Q to study the difference between different solvus. However, it is clear that this result does not represent the best-fit on the data and could cause a large fitting uncertainty, which was not reported.

The solvus in Table 2.2 were plotted in Fig. 2.12 for a better comparison. For the TSSd solvus where the A value varies significantly, it is difficult to quantitatively compare the solvus by solely considering the Q or A. For example, the TSSd data from Vizcaíno *et al.* [69] has the second highest Q_{d} value and the highest hydrogen content at a given temperature. For the TSSp solvus were the A values are comparable, the hydrogen content is predictable by solely comparing the Q_{p} value; the increase of Q_{p} decreases the hydrogen content in the solid solution. All the data in Table 2.2 exhibits the hysteresis behavior. This is shown in Figure 2.13 by plotting the TSSd and TSSp solvus together; the average hysteresis is 100-120 wppm of hydrogen at 600 K.

Une and Ishimoto [65] observed two different TSSp solvus at different temperature ranges by cooling the sample 10 °C min^{-1} from 600 °C to the room temperature. The first TSSp is at 261 to 600 °C while the second TSSp is below 261 °C. The author attributed the two

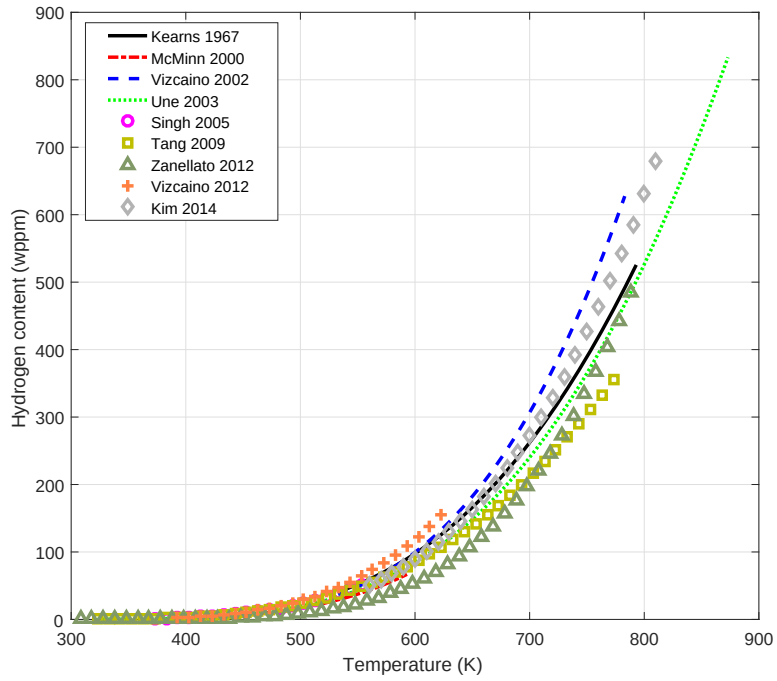

(a) TSSd solvus

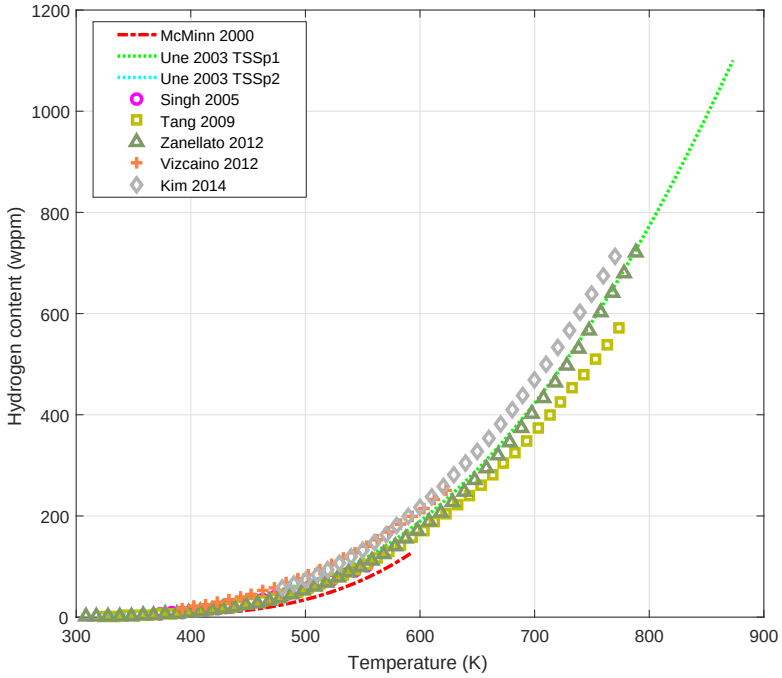

(b) TSSp solvus

Figure 2.12: Hydrogen solvus line in Zircaloy solution plotted using the data listed in Table 2.2 for (a) TSSd solvus and (b) TSSp solvus.

different TSSp to different hydride phase present at the different temperature range. This phenomenon, however, was not observed by others.

Colas *et al.* [28] obtained a much lower Q_p value for hydrogn in a CWSR Zry-4 material with a 160 MPa tensile stress applied along the TD of the sample. This result suggests that the applied tensile stress decreases the Q_p for hydride precipitation. The lower Q_p also means the higher hydrogen content in the solid solution. The author, however, attributed this stress effect to the large uncertainty of their measurement. A similar effect was also observed by Vizcaíno *et al.* [59]. These authors studied a hydrided Zr-2.5%Nb alloy with a

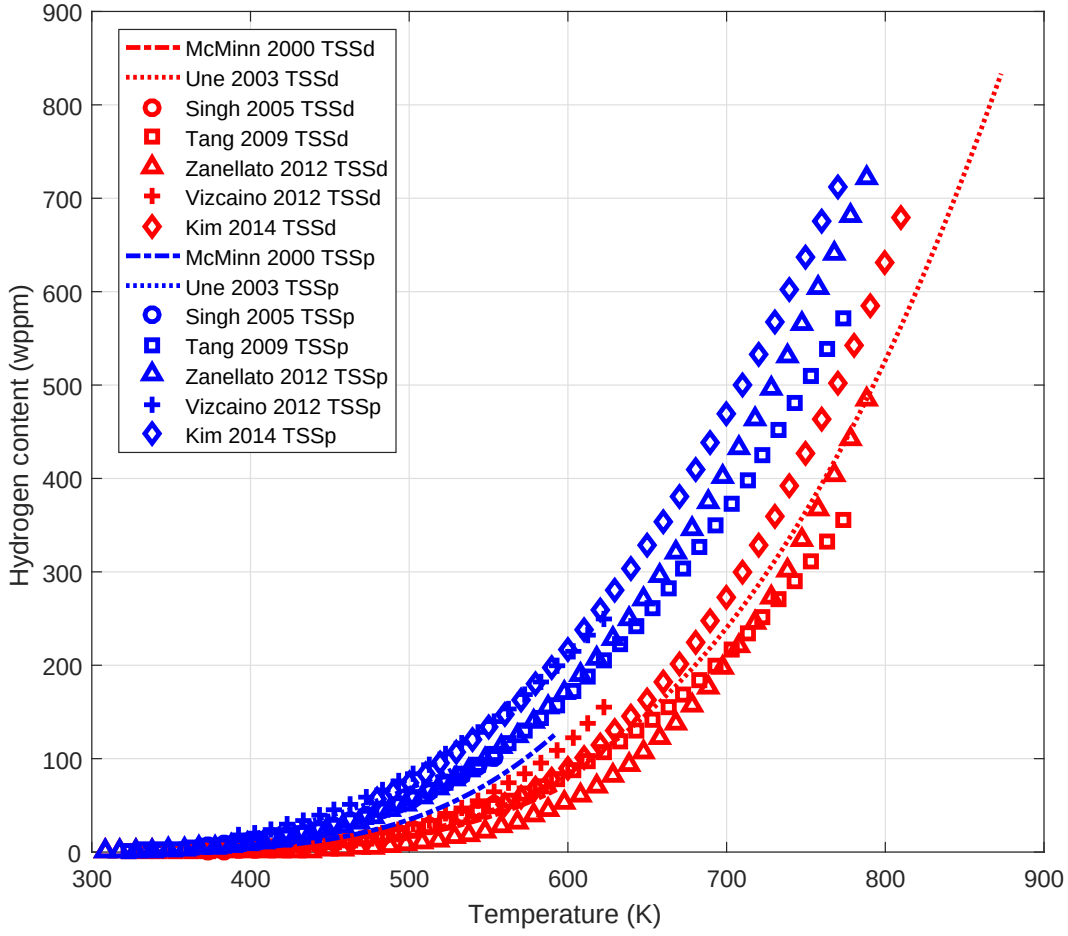

Figure 2.13: Hydrogen solvus data from Table 2.2, showing the hysteresis between the heating and the cooling solvus. Red and blue line or marker represents the TSSd and the TSSp solvus, respectively.

225 MPa tensile stress applied along the TD of the sample. The sample was thermo-cycled between the room temperature and 400 °C while the dissolution and precipitation of the hydride phase were recorded by the synchrotron diffraction. They observed that the applied stress increased the hydrogen TSSp but decreased the TSSd, reducing the hysteresis gap between the two solvus. The magnitude of solvus variation depended on the crystalline orientation; the maximum solvus shift was 18 °C at 225 MPa for zirconium grains which had their basal normal parallel to the applied stress. Results in Ref. [28] and Ref. [59] both suggested that the applied tensile stress would affect the hydrogen solvus, and this influence was much larger than what was predicted by the current theory (Eqn. (2.16) and (2.17)). The same conclusion was made in Ref. [59]. Since both studies (Ref. [28] and Ref. [59]) used synchrotron X-ray diffraction on materials with strong texture and the examination of the hydride phase relies on a single hydride phase reflection, it is possible that the results do not represent the average behavior of a bulk material. A recent study by Lin *et al.* [74] which combined the radiography imaging and the finite element analysis also indicated that the hydride distribution closely followed the stress distribution in a component. Because of this disagreement between the experimental result and the model from the present literature and limited experimental data regarding the influence of applied stress on the hydrogen solvus in Zircaloy, this doctoral research performed a comprehensive study on this topic.

Table 2.2: Experimental conditions and results for hydrogen solvus in Zircaloy materials.

Author	Technique	$[H]_{tot}$	T_{max}	T_{range}	heating/cooling rate	holding time	$\sigma_{applied}$	TSSd solvus	
		(wppm)	(°C)	(°C)	(°C min^{-1})	(min)	(MPa)	A (wppm)	Q_d^* (J/mol)
Kearns 1967 [16]	Diffusion	NA	∼525	260-525	NA/NA	10 days	None	98716	34518
McMinn 2000 [15]	DSC	20 to 80	400	120-320	2/2	NA	None	106447	36438
Vizcaíno 2002 [69]	DSC	20 to 80	570	260-510	5/5	∼10	None	263024	39308
Une 2003 [65]	DSC	40 to 542	600	50-600	10/10	5	None	128000	36540
Singh 2005 [70]	Dilatometry	43 to 100	430	100-280	2/2	30	None	94042	34550
Tang 2009 [60]	DSC	20 to 240	500	50-500	10/10	5	None	52575	32117
Zanellato 2012 [71]	SXD**, 20° span along TD on δ(311)	475 to 600	570	35-520	5/5	30	None	510800	45610±160
Vizcaíno 2012 [72]	DSC	62 to 80	420	125-350	20/20	5	None	171687	36307
Kim 2014 [68]	DSC	40 to 731	550	287-545	20/20	5	None	225500	39101

Author	Technique	$[H]_{tot}$	T_{max}	T_{range}	heating/cooling rate	holding time	$\sigma_{applied}$	TSSp solvus	
		(wppm)	(°C)	(°C)	(°C min^{-1})	(min)	(MPa)	A (wppm)	Q_p^* (J/mol)
McMinn 2000 [15]	DSC	20 to 80	400	120-320	2/2	NA	None	138746	34468
Une 2003 [65]	DSC	40 to 542	600	261-600	10/10	5	None	52600 ($T > 260$°C)	28068 ($T > 260$°C)
	DSC	40 to 542	600	50-260	10/10	5	None	10700 ($T \leq 260$°C)	21026 ($T \leq 260$°C)
Singh 2005 [70]	Dilatometry	43 to 100	430	100-280	2/2	30	None	31236	26315
Tang 2009 [60]	DSC	20 to 240	500	50-500	10/10	5	None	40135	27336
Vizcaíno 2012 [72]	DSC	62 to 80	420	125-350	20/20	5	None	23623	23562
Zanellato 2012 [71]	SXD, 20° span along TD on δ(311)	475 to 600	570	35-520	5/5	30	None	66440	29630±160
Colas 2013 [28]	SXD, 20° span along TD on δ(111)	190 to 350	450		25/1	∼60	None	NA	24320
Colas 2013 [28]	SXD, 20° span along TD on δ(111)	190 to 350	450		25/1	∼60	160‖TD	NA	12040
Kim 2014 [68]	DSC	40 to 731	550	207-504	20/20	5	None	47220	26843

*Q_d and Q_p represents the energy for TSSd and TSSp, respectively.

**Synchrotron X-ray diffraction.

CHAPTER 3

IN SITU DIFFRACTION EXPERIMENTS

3.1 Experimental method

3.1.1 Sample preparation

CWSR Zircaloy-4 plates with various thicknesses were purchased from ATI Specialty Alloys and Components. Plates with thickness of 1.5 and 3 mm were used for synchrotron and neutron diffraction, respectively. The relative thick plate is necessary to increase the signal-to-noise ratio when measured using the high penetration neutron beam. The basal pole figure of this material was measured using the PANalytical X'Pert PRO X-ray diffraction system in Frederick Seitz Materials Research Laboratory at the University of Illinois at Urbana-Champaign and is shown in Fig. 3.1. The Kearns factors along the three principal directions of the sample were calculated using Eqn. (2.1) with the intensity data in Fig. 3.1; the values were found to be equal to 0.65 in the ND, 0.27 in the TD and 0.07 in the RD. These values are in good agreement with the result reported in [28] for a similar material. The chemical composition of this material was provided by the ATI Specialty Alloys and Components which met the requirement of ASTM Standards [1] for the Zircaloy-4 alloy.

Dog-bone tensile specimens were machined from the Zry-4 plate using the electrical discharge machining (EDM) to avoid generating the machining residual stress. The dimension of the tensile specimen is specified in Fig. 3.2. The surface of the tensile specimens were mechanically polished starting with a 180 grit sandpaper and ended up with the 0.05 µm silica suspension. A thin Ni film ($\sim$ 0.2 µm) was sputter coated on the polished surface to enhance the near-surface hydrogen diffusion into the specimen. There is an argument indicates that the mechanical polishing could generate residual stress in the specimen. A

different option for pre-coating surface preparation is to immerse the specimen in the 10:10:1 HNO_3:H_2O_2:HF acid solution; this also helps clean the oxide layer left by the EDM. Disadvantages are the etching process can introduce additional hydrogen and the high safety risk when working with the hydrofluoric acid.

The tensile specimen was hydrided using a Sievert-type gas charging apparatus. A schematic diagram of this apparatus can be found in [14]. The hydrogen charging process was performed at 400 °C after the vacuum reached 10^{-8} torr. The variation of the hydrogen partial pressure in the system was monitored by capacitance manometer gauges until the amount of hydrogen in the sample reached the desired concentration at equilibrium with the gas phase. For neutron scattering experiment, deuterium was selected over hydrogen due to its low neutron incoherent scattering cross section and large neutron coherent scattering cross

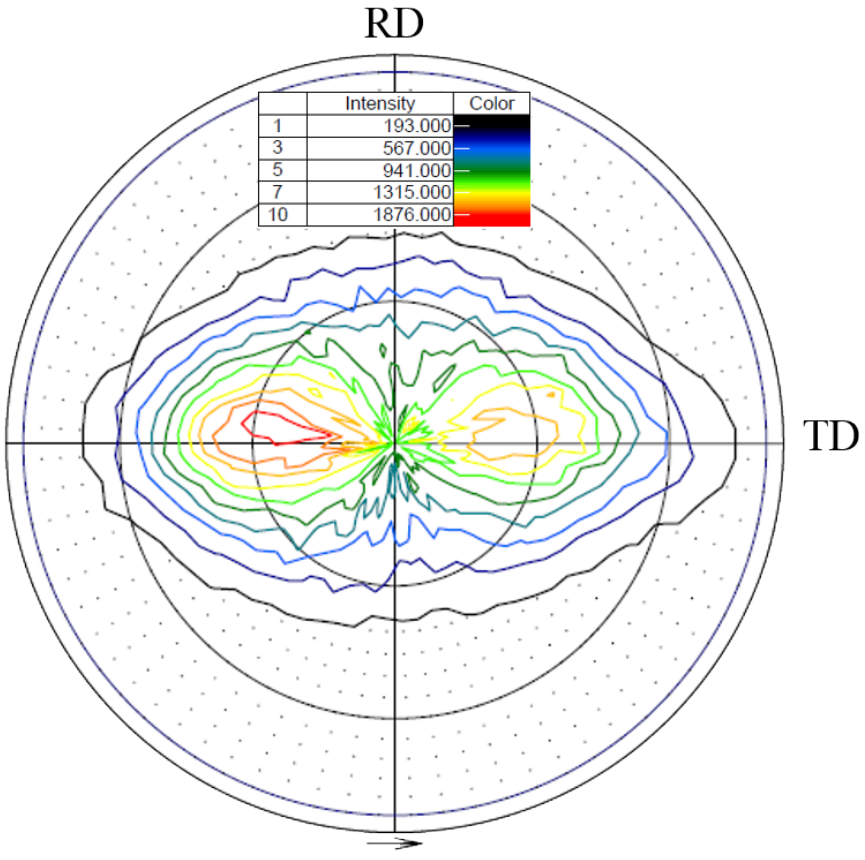

Figure 3.1: Zirconium (0002) basal plane pole figure for the ATI CWSR Zircaloy-4 plate. The corresponding sample orientation is also shown on the figure. This figure was reprinted from Fig. 1a in Ref. [12].

section. The sample was then slowly cooled at 1 °C min^{-1} from 400 °C to the room temperature, precipitating hydride that the majority was in δ-phase [50]. The presence of the Ni film resulted in the formation of a hydride rim or blister layer near the Ni-coated surface, simulating the hydride rim structure typically observed on the post-service fuel cladding tubes.

The metallographic etching process is necessary to reveal the hydride phase under an optical microscope. For the etching process, the cross-section plane of a hydrided sample was swabbed for $\sim$ 10 seconds with a cotton swab dipped in the 10:10:1 HNO_3:H_2O_2:HF acid solution. The cross-section plane needs to be polished at least to a 1200 grit sandpaper prior to the etching. The author highly recommends to mount the sample in the epoxy resin

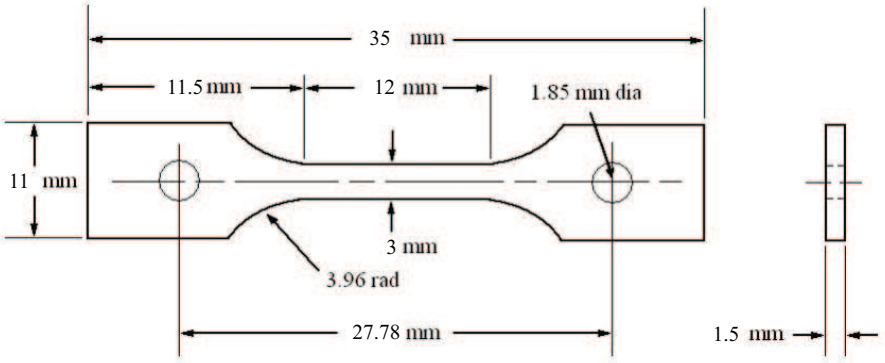

(a)

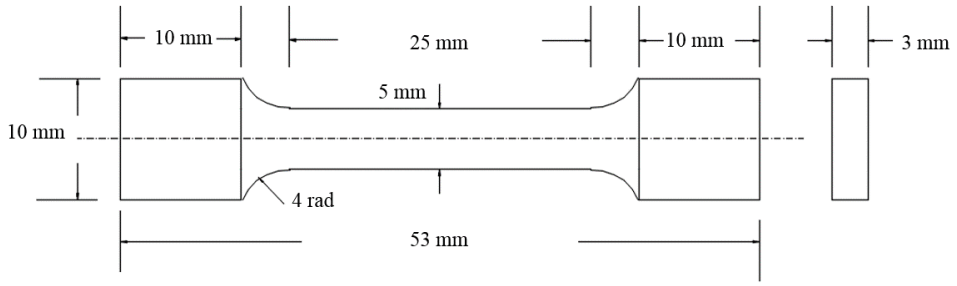

(b)

Figure 3.2: Dimension of the tensile specimen for (a) APS 1-ID and (b) VULCAN.

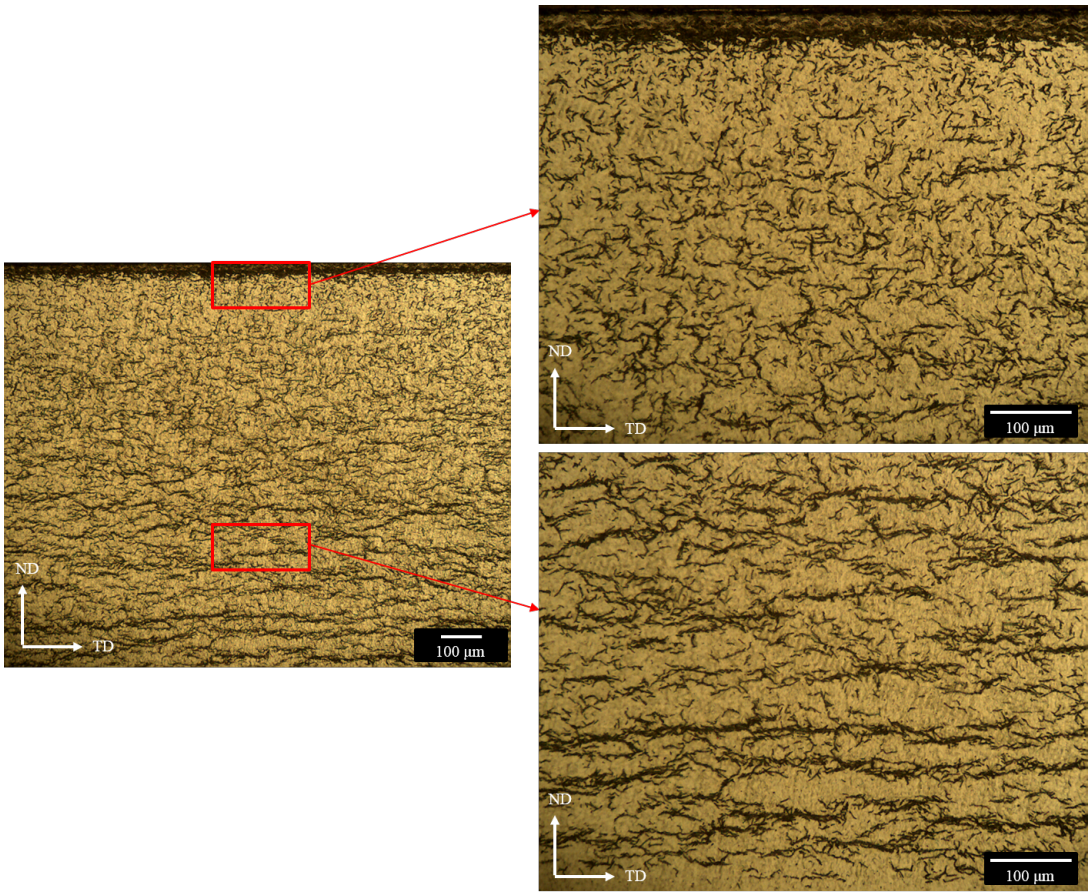

Figure 3.3: Optical images of the cross-section plane of a hydrided sample. A near-surface high-density hydride rim/blister layer was observed. The hydride particles distributed uniformly underneath the rim/blister structure with their long axis along the TD. This sample has 977 wppm of hydrogen. These images were reprinted from Fig. 2 in Ref. [12].

for this process; this protects other surfaces of the sample as well as stabilizes the sample. Images of an etched cross-section plane are shown in Fig. 3.3 for a sample which has 977 wppm of hydrogen. The thickness of the blister/rim structure was 60-68 µm at this hydrogen concentration, which yields a volume fraction of $\sim$ 5% for the blister/rim structure. This result indicates that the contribution of hydride rim/blister structure to the total diffraction intensity from the δ-hydride phase is relatively small.

3.1.2 Diffraction instrument and preliminary data analysis

This thesis utilized in situ synchrotron X-ray and time-of-flight (TOF) neutron diffraction instruments. Table 3.1 briefly summarizes the usage of the beamlines in this research.

In situ synchrotron X-ray diffraction was performed at the 1-ID beamline of the Advanced Photon Source at Argonne National Laboratory, while in situ time-of-flight (TOF) neutron diffraction was conducted using the VULCAN engineering materials diffractometer at Spallation Neutron Source (SNS) at Oak Ridge National Laboratory. The 1-ID Beamline used a set of high-resolution quad GE detectors with 2048×2048 pixels per detector, while VULCAN used the two stationary bank detectors sitting at the scattering angle of $\pm 90^{\circ}$. The instrument setups are shown in Fig. 3.4. For 1-ID, the transmission geometry allows the full Debye-Scherrer ring to be measured; this allows users to focus on grains with the specific orientation by integrating the Debye-Scherrer ring within certain angular sector. An example is shown in Fig. 3.5, where the ring was integrated along the four principal directions to study reflection planes with their normal parallel to these directions. For VULCAN, bank 1 and bank 2 detector record the lattice planes with their normal parallel to the scattering vectors Q_1 and Q_2, respectively. Each bank covers a $\pm 11.5^{\circ}$ diffraction angle. For our measurements, Q_1 and Q_2 were parallel to the RD and ND sample direction, respectively. The external load for both experiments was applied along the RD of the sample using the MTS® load frame system. A clamshell furnace and an induction coil were used in 1-ID and VULCAN for the in situ heating.

Matlab scripts developed by the instrument scientists at 1-ID were used as the main program for the x-ray diffraction data analysis. FIT2D was used for instrument calibration and detector correction [75, 76]. The tilt angle of each quad detector panel was measured by an electronic goniometer. These calibration data are required to input in the Matlab scripts in order to perform further data analysis.

For neutron diffraction at VULCAN, the detector was pre-calibrated with the data being stored in an instrument file. This instrument file was input along with the diffraction data of

Table 3.1: Summary of the beamline usage and the conducted conditions.

Date	Test Procedure	Technique	Eq-Hydrogen Content (Wppm)	$T_{\max}$ (°C)	Heating/Cooling Rate (°C min^{-1})	Max σ_{applied} (MPa)
June 2013	Isothermal Stress-strain	Synchrotron Diffraction	98 - 977	200	25/NA	190 - 218
March 2014	Isostress Cooling	Neutron Diffraction	527	420	NA/1	78
Aug 2014	Isostress Thermal-cycle	Synchrotron Diffraction	520	400	25/1	104

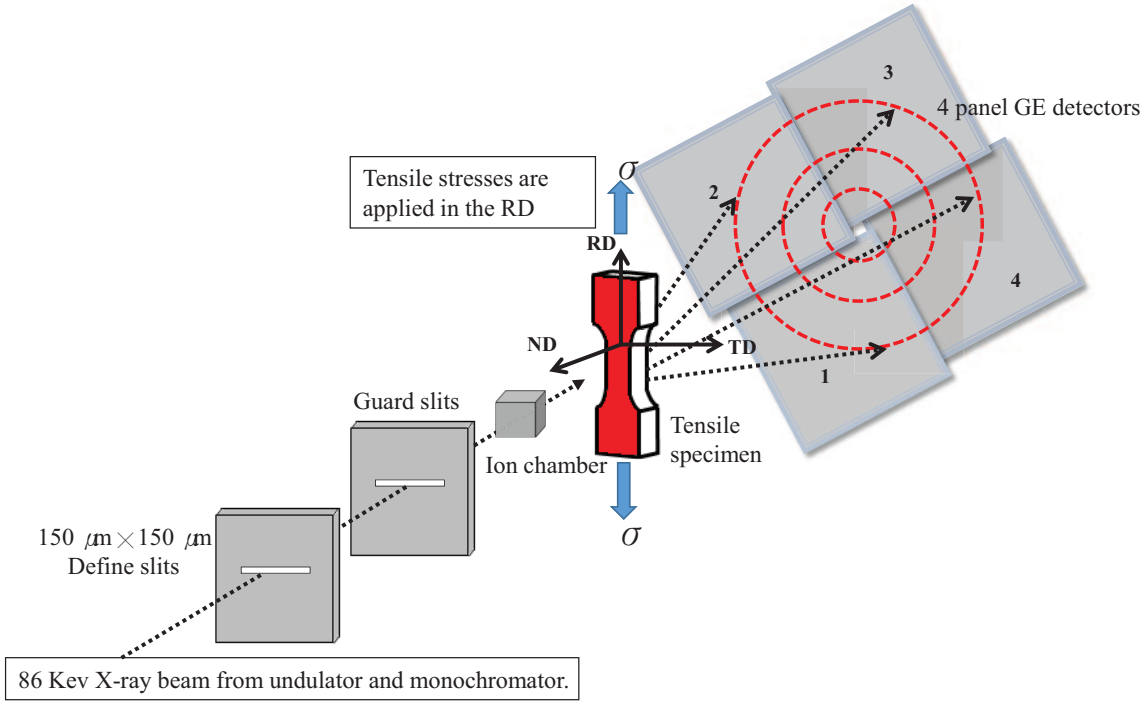

(a)

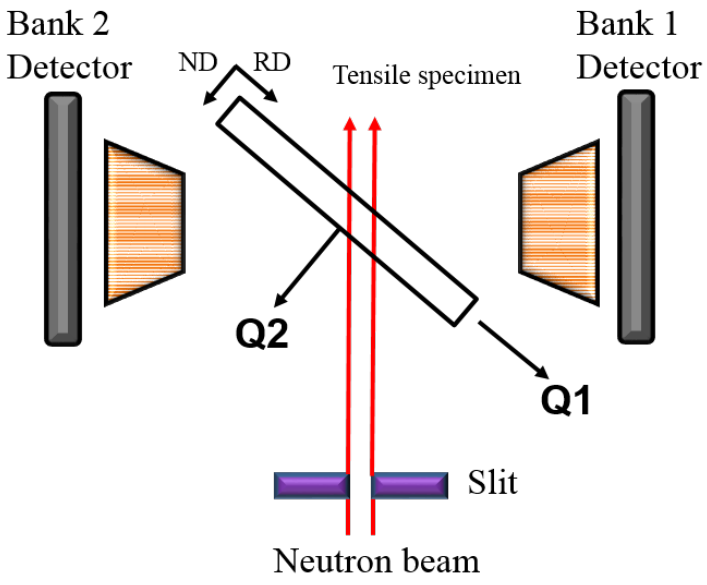

(b)

Figure 3.4: Schematic illustration for the instrument arrangement at (a) APS 1-ID and (b) VULCAN. The red area indicates the surface which has the hydride blister. Figures were reprinted from Fig. 1b in Ref. [13] and Fig. 4 in Ref. [12].

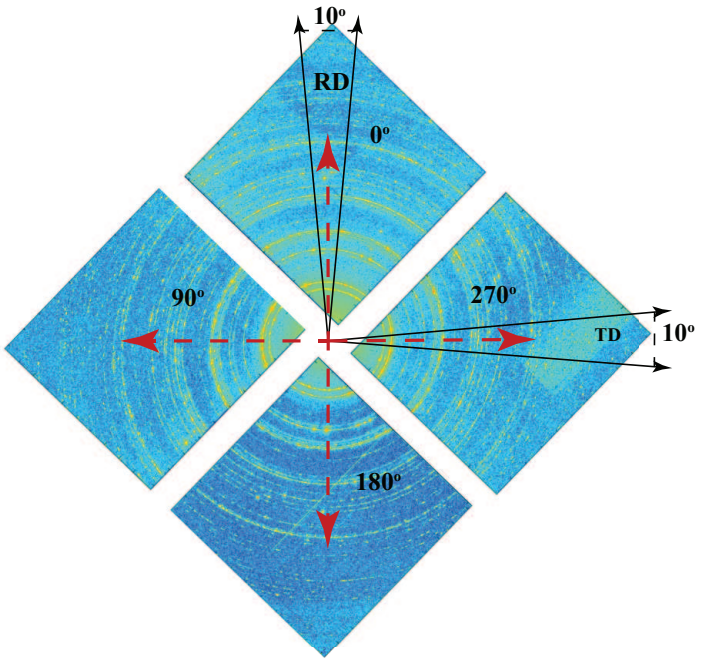

Figure 3.5: A typical Debye-Scherrer ring composed by the quad-panels detector in 1-ID. This figure shows an example of the intensity integration performed on the ring. This figure was reprinted from Fig. 5a in Ref. [14].

the sample into the VULCAN Data Reduction and Interactive Visualization (VDRIVE) software, a Linux-based analysis software developed by the VULCAN scientists. A long neutron exposure time is necessary to obtain the statistically significant diffraction intensity from the zirconium deuteride phase. For our in situ measurement, each TOF neutron diffraction spectra contained 60 minutes of the exposure time. The temperature and stress magnitude of each spectrum was, therefore, an average value in the corresponding 60 minutes period. The detail thermomechanical information is included in Section 3.2.2.

Fig. 3.6a and Fig. 3.6b shows the measured diffraction spectra from 1-ID and VULCAN, respectively. For the 1-ID, the spectrum shows the intensity that has been integrated over the entire Debye-Scherrer ring; for the VULCAN, the spectrum shows the summed intensity of the two detectors. The α-Zr phase is the dominant phase observed as expected. The δ-hydride phase is the only hydride phase observed. The strongest diffraction intensities of this phase were the (111) and (220) reflection for 1-ID and VULCAN measurement. This difference is caused by the strong texture of the matrix material and the different

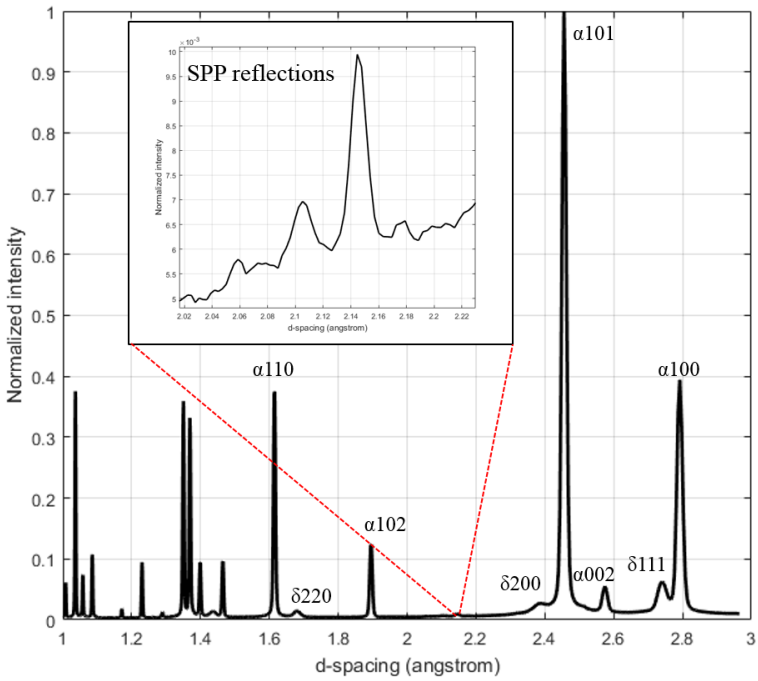

(a) 1-ID

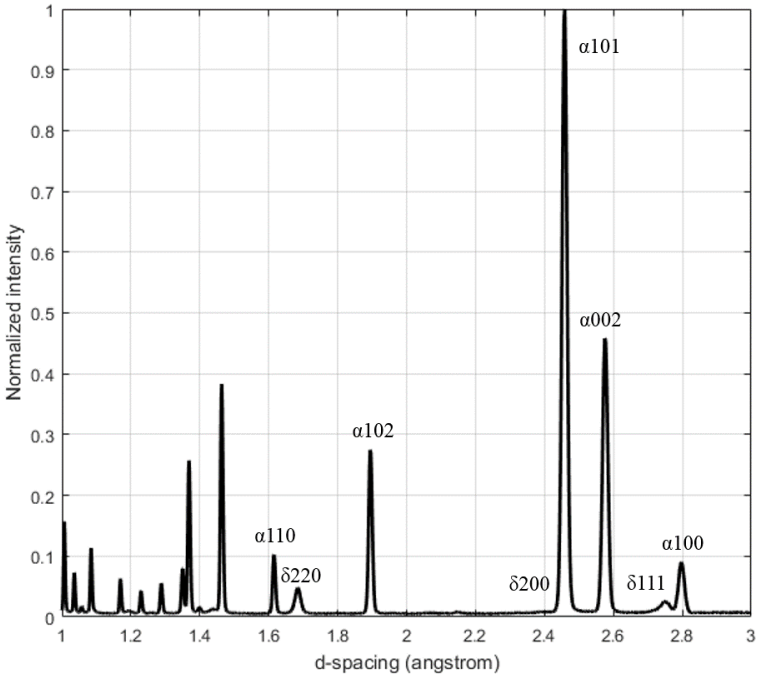

(b) VULCAN

Figure 3.6: Diffraction spectra. (a) 1-ID at APS. Sample was at the room temperature and had 977 wppm of hydrogen. (b) VULCAN at SNS. Sample was at the room temperature and had 2054 wppm of deuterium.

arrangements of the two instruments shown in Fig. 3.4. The largest Kearns factor direction ND was included in VULCAN but excluded in the 1-ID measurement. Therefore, the much higher α-Zr(0002) basal plane intensity was observed by VULCAN than the 1-ID. The δ-phase, which has the strong orientation relationship with the α-Zr (Eqn. (2.7)), also inherits the texture from the α-Zr phase. The measurement from 1-ID also revealed SPP phase in Zry-4 which was identified as a hexagonal C14 laves phase with the composition of $Zr(Fe_{1.5}Cr_{0.5})_2$ [12]. The SPP signal was relative weak in the VULCAN data.

The further data analysis includes the single or multiple reflection peak fitting and fits the entire spectrum using the Rietveld refinement. The single peak fitting gives the information of a grain subset throughout the in situ experiment. The Rietveld refinement, on the other hand, yields the information that is an average result from every recorded reflection in a spectrum. Fig. 3.7 shows an example of peak fitting done in this work for the δ-hydride reflection. The Pseudo-Voigt function was adopted as the fitting peak profile. Because the $\alpha(100)$ and $\delta(111)$ peaks partially overlap, these two peaks are fitted simultaneously by performing the multiple peaks fitting. An example of Rietveld refinement done in this work is shown in Fig. 3.8.

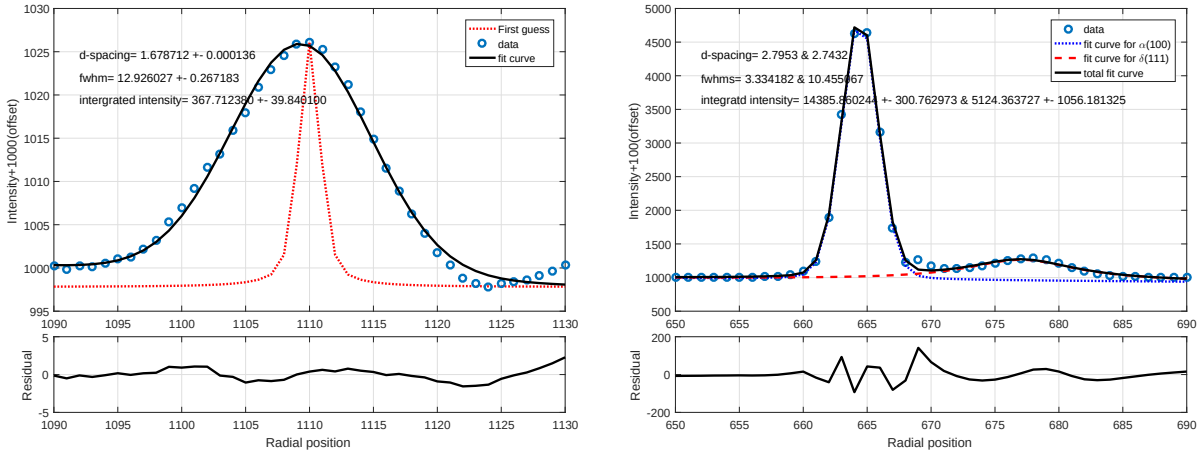

(a) $\delta(220)$ (b) $\alpha(100)$ and $\delta(111)$

Figure 3.7: Examples of reflection peak fitting for (a) $\delta(220)$ and (b) multiple peaks fitting for $\alpha(100)$ and $\delta(111)$. The fitting residual is shown in the subplot.

A crystallography data analysis software GSAS [77] and its graphic interface EXPGUI [78]

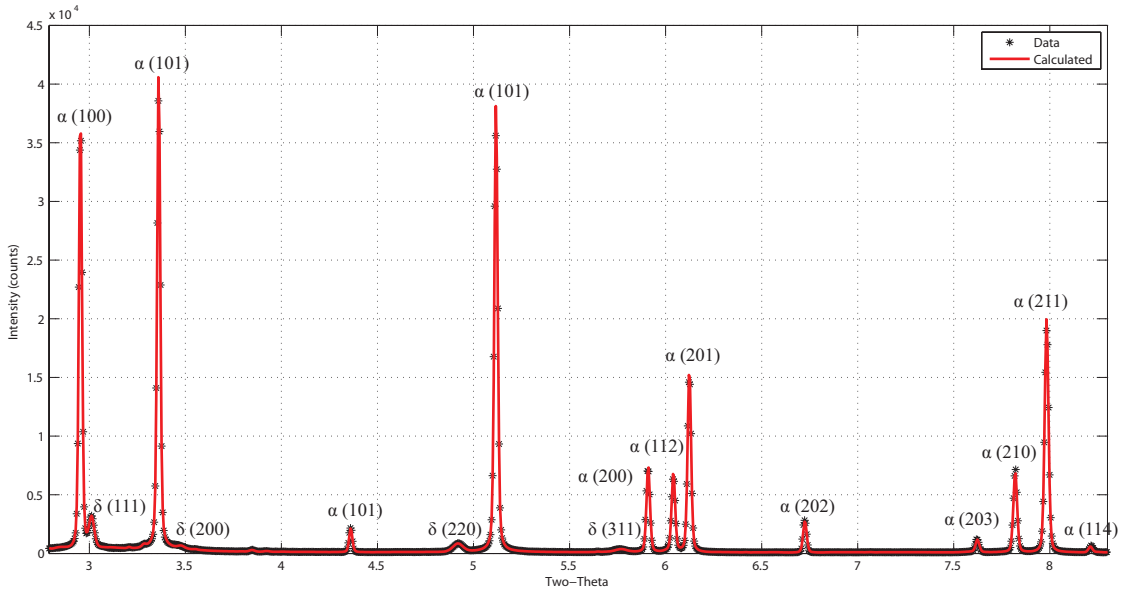

(a)

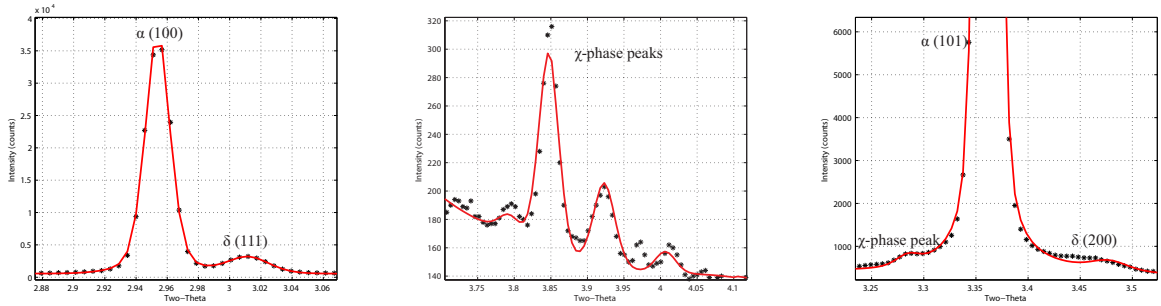

(b) (c) (d)

Figure 3.8: An example of Reitveld refinement fit for a sample which has 977 wppm of hydrogen. Figures on the bottom row focus on the hydride and SPPs reflections and their refinement result. Figures were reprinted from Fig. 6 in Ref. [12]

were used to perform the Rietveld refinement. The strong texture of this material was refined using the spherical harmonics model, while the number of refined coefficients was carefully chosen to obtain a unique solution without losing the physical meaning.

The data that resulted from the fitting and the refinement were further interpreted to obtain the phase information needed. This study considered the amount of hydrogen concentration in the zirconium solid solution under applied stress. This is further discussed in the next section.

3.1.3 Calculating hydrogen content in the solid solution using the diffraction method

For the diffraction experiment, the amount of hydrogen in zirconium solid solution were determined from 1): the change of reflection intensity from the hydride phase [13, 28, 71] and 2): the change of zirconium lattice spacing due to hydrogen occupy the interstitial site [13, 59].

The first method assumes the volume fraction of the hydride phase in the measured volume is linearly proportional to the integrated intensity of the reflection. The integrated intensity of any reflection peak I_i^{hkl} from phase i is [79],

$$I_i^{hkl}(T) = \frac{K R_i^{hkl}(T) V_i(T)}{2\mu} H_i^{hkl} \tag{3.1}$$

where

$$K = \Big(\frac{I_0 A \lambda^3}{32\pi r}\Big)\Big(\frac{\mu_0 e^4}{4\pi m^2}\Big) \tag{3.2}$$

and

$$R_i^{hkl} = \Big(\frac{1}{\nu_i^2}\Big)\left[|F^{hkl}|^2 p\Big(\frac{1+\cos^2 2\theta_i}{\sin^2 2\theta_i \cos\theta_i}\Big)\right](e^{-2M}) \tag{3.3}$$

K is the instrument factor and is independent of the temperature T. The constant variables in K include I_0: the incident beam intensity, A: the cross section area of the incident beam, r: the radius of the diffractometer circle, e and m: the charge and mass of an electron, respectively. R_i^{hkl} is the temperature-dependent material scattering factor which includes

θ_i: a variable that depends on the interplanar spacing, composition and crystal structure of the phase i, F^{hkl}: the structure factor of the $\{hkl\}$ reflection, p: the multiplicity factor and e^{-2M}: the Debye-Waller factor. V_i is the volume fraction of the phase i and μ is the linear absorption coefficient. H_i^{hkl} is the Harris texture index. The ratio between $I_i^{hkl}(T)$ at different temperatures is,

$$\frac{I_i^{hkl}(T_2)}{I_i^{hkl}(T_1)} = \frac{R_i^{hkl}(T_2)V_i(T_2)H_i^{hkl}(T_2)}{R_i^{hkl}(T_1)V_i(T_1)H_i^{hkl}(T_1)} \tag{3.4}$$

. The temperature-independent terms are canceled. The texture index H_i^{hkl} is considered temperature-dependent since the material texture can change when the testing temperature is close to the phase transformation or recrystallization temperature. The temperature contribution of R_i^{hkl} is from the Debye-Waller factor e^{-2M}. In this study $i = \delta$ since δ is the only hydride phase observed.

Zanellato *et al.* [71] thermal-cycled a CWSR Zry-4 plate several times between 50 to 570 °C. These authors found that the change of material texture was negligible under the test conditions. Therefore, the CWSR Zry-4 texture should be fairly stable within the temperature range listed in Table 3.1. It is then reasonable to assume the H_δ^{hkl} is temperature-independent. Zanellato *et al.* [71] also found that the Debye-Waller contribution was also negligible under their thermal-cycle condition. These observations simplify Eqn. (3.4) which yields,

$$\frac{I_\delta^{hkl}(T_n)}{I_\delta^{hkl}(T_0)} = \frac{V_\delta(T_n)}{V_\delta(T_0)} \tag{3.5}$$

After rearranged,

$$V_\delta(T_n) = V_\delta(T_0)\frac{I_\delta^{hkl}(T_n)}{I_\delta^{hkl}(T_0)} \tag{3.6}$$

Eqn. (3.6) suggests that the volume fraction of the δ-hydride phase at any temperature T_n can be calculated by knowing the volume fraction of the δ-hydride phase at a reference temperature T_0 and using the ratio of the integrated diffraction intensity between the T_n and T_0. T_0 is chosen at a temperature that the value of hydride volume fraction is known. For example, room temperature ($\sim$25 °C) is commonly used as T_0 since the amount of hydrogen in the sample can be pre-quantified by the hot extraction or the Sievert-type gas charging

method. The amount of hydrogen in the Zircaloy solid solution is determined by applying the conservation rule,

$$[H]^{\alpha}(T_n) = \frac{[H]^{\alpha}(T_0) - w_{\delta}(T_n)[H]^{\delta}(T_n)}{1 - w_{\delta}(T_n)} \tag{3.7}$$

$[H]^{\alpha}(T_n)$ is the hydrogen concentration by weight in the α-Zr solid solution at T_n. $[H]^{\alpha}(T_0)$ is the known amount of hydrogen concentration in the α-Zr solid solution at T_0. w_{δ} is the weight fraction of the δ-hydride phase which is converted from the V_{δ} in Eqn. (3.6). $[H]^{\delta}(T_n)$ is the maximum amount of hydrogen in the δ-hydride phase at T_n and is determined using the boundary between the δ and $\delta + \alpha$ phase in the binary Zr-H phase diagram [5].

The second method is to calculate the amount of hydrogen in the zirconium solid solution using the change of the zirconium lattice parameter using the known Vegard's law [80]. As discussed in the Section 1.2.1, the dilatation caused by the interstitial hydrogen was obtained as 4.85 and 2.86 $\mu\epsilon$ per wppm of hydrogen along the c-axis and the a-axis of the zirconium lattice, respectively. The major disadvantage of this method is the thermal and mechanical lattice strain must be subtracted to obtain the strain solely due to interstitial hydrogen. The finding of our experimental work is discussed in the following sections.

3.2 Result and discussion

3.2.1 Isothermal stress-strain experiment

This experiment was conducted at 1-ID beamline at APS. The 150×150 µm^2 beam size with 86 KeV X-ray energy was chosen. The data acquisition program automatically scanned 12 data points on the gauge section of the tensile specimen for each sequence. These 12 points were summed to increase the signal-to-noise ratio. Each data point had 1 second exposure time to avoid detector saturation due to the strong texture of the Zr matrix. This procedure also effectively increased the measured volume and minimized the sampling effect. Samples were first measured at the room temperature with zero applied load and then heated to 200 °C. The applied load was then increased incrementally to 700 N, corresponding to ∼200 MPa tensile stress. The load was applied along the RD of the specimen. The thermomechanical

history of this experiment is shown in Fig. 3.9. Samples were hold for ~ 5 minutes at each stress level. Four samples with hydrogen content of 0, 98, 492 and 977 wppm were studied in this experiment. The integrated intensity evolution of the $\delta(220)$ peak as a function of stress is shown in Fig. 3.10a and Fig. 3.10b for the RD and TD segment, respectively. Each segment contains a 10° span along the principal directions of the diffraction ring, as shown in Fig. 3.5. The result suggests the δ-hydride phase has no clear dependency on the applied tensile stress at 200 °C. In this experiment, the load-partitioning between the α-Zr and the δ-hydride phase was observed after the α-Zr matrix yielded [48]. Beyond the yield point of the matrix, the strain in δ-phase increased significantly while the strain in the Zry-4 matrix stayed invariant with an increasing applied load. The magnitude of the stress transferred between the two phases has also been quantified in this experiment and published in [14].

This experiment concluded that the hydrogen content in a measured volume is independent of the applied stress under an isothermal condition. The next in situ experiment, therefore, gradually cooled the temperature down while applied a constant load on the sample.

3.2.2 Isostress cooling experiment

This experiment was conducted at VULCAN at SNS. The sample was heated to 420 °C then slowly cooled to RT at 1 °C min^{-1} with a constant 78 MPa tensile stress applied along

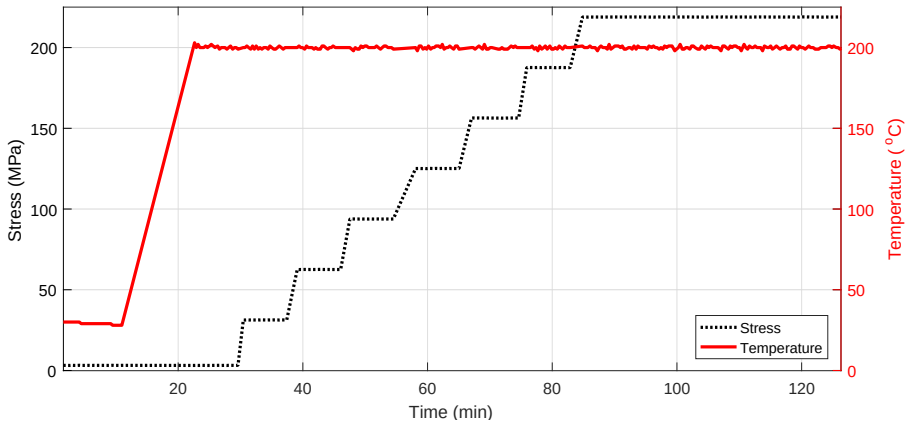

Figure 3.9: The thermal and mechanical history throughout the isothermal stress-strain in situ experiment. The black dotted line and the red solid line represents the stress and the temperature value, respectively.

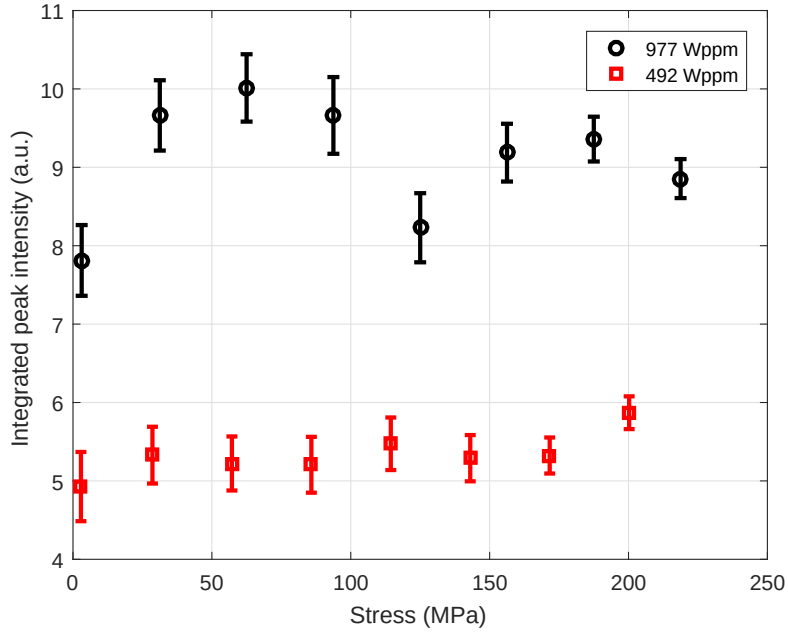

(a) TD segment

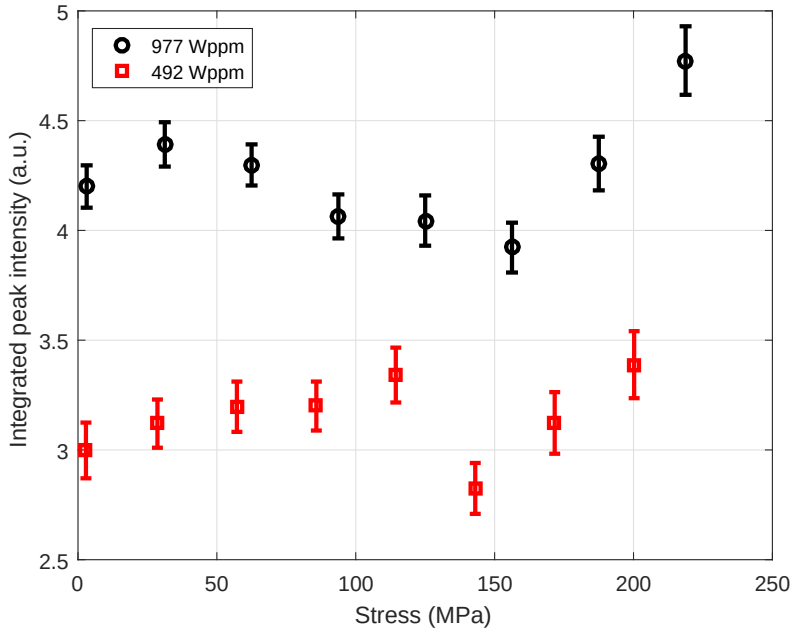

(b) RD segment

Figure 3.10: Evolution of the $\delta(220)$ integrated intensity as a function of applied stress. (a) Diffraction intensity from the RD and (b) the TD segment. The black circle and the red square represents data from the sample with 977 and 492 wppm of hydrogen, respectively.

the RD. The thermal-mechanical history of this experiment is shown in Fig. 3.11. This sample contained 1054 wppm deuterium or 527 wppm hydrogen-equivalent concentration. A ∼20 µm of deuteride rim/blister was observed near the ND surface, similar to what was shown in Fig. 3.3.

Because of the limited angle covered by the two-banks detector (±11.5°), each of the diffraction banks recorded only a sub-set of deuteride grains, which have precipitated on a certain subset of α-Zr grains of a variety of orientations. Hence, it is expected that the result of the experiment will depend on the grain subsets sampled by each diffraction bank. It is possible that the deuteride volume fractions provided by each of the diffraction banks do not coincide with the average behavior of the whole specimen. Therefore, Rietveld refinement was performed to measure the deuteride phase fraction at 70 °C for each bank. These values were used as the reference $V_\delta(T_0 = 70\ ^\circ\text{C})$ in Eqn. (3.6) which all deuterium was regarded in the form of the deuteride phase at this temperature. The $V_\delta(T_0 = 70\ ^\circ\text{C})$ value, converted into total deuterium concentration, were obtained as ∼660 and ∼ 1500 Wppm deuterium in the Bank1 and the Bank2 detector, corresponding to the ND and RD of the specimen, respectively. The average value is very close to the average deuterium concentration contained by the specimen, which is 1054 wppm deuterium. The deuterium concentration in the α-Zr solid solution was calculated using Eqn. (3.7). The weight fraction of the δ-phase at any temperature $w_\delta(T_n)$ was calculated using Eqn. (3.6) based on the $\delta(220)$

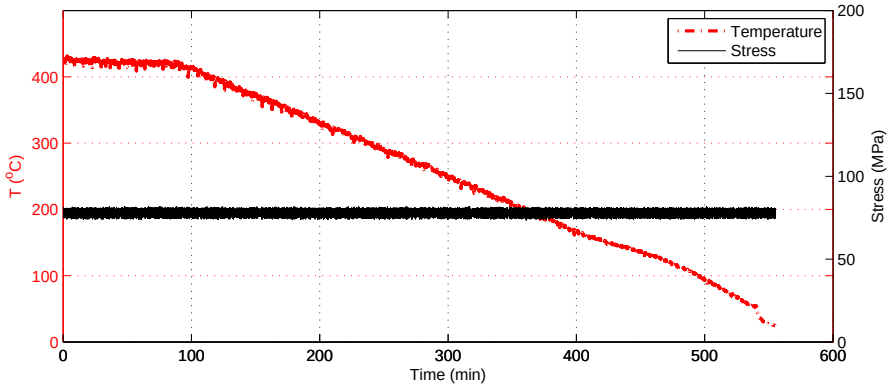

Figure 3.11: The thermomechanical history throughout the isostress cooling in situ experiment. The black-solid line and the red-dashed line represents the stress and the temperature value, respectively.

reflection or using the Rietveld refinement; the corresponding amount of deuterium in the solid solution was denoted as $[D]^{\alpha}$ and $[D]^{\alpha}_{\mathrm{RF}}$ in Fig. 3.12a, respectively. We note that the solubility of deuterium in a Zircaloy is approximated 2 wppm at 70 °C [15]. Therefore, choosing the data at 70 °C as the reference slightly overestimated the amount of deuterium in the deuteride phase, but this deviation was negligible.

$[D]^{\alpha}_{\mathrm{RF}}$ contains information of a larger grain subsets than $[D]^{\alpha}$ which only contains grains belong to the observed $\delta(220)$ reflection. The orientation of these grains, however, cannot be identified from the data due to the instrument limitation of VULCAN. This insufficiency is addressed in the next in situ synchrotron diffraction performed for this research, which the record of a full Debye-Scherrer ring allows us to study the texture relationship between the δ and α phase. Surprisingly, the result in Fig. 3.12a shows the value of $[D]^{\alpha}_{\mathrm{RF}}$ and $[D]^{\alpha}$ is comparable. This suggests that under the current experimental condition, the effect of Zr grain orientation is insignificant, and using the intensity of a single $\delta(220)$ reflection is sufficient to represent the average behavior of the deuteride phase in each bank. Thus, the following data interpretation will only focus on $[D]^{\alpha}$.

Fig. 3.12b shows the result that the evolution of $[D]^{\alpha}_{\mathrm{RF}}$ and $[D]^{\alpha}$ is described using Eqn. (2.18). The data were fit using the York linear regression method [81] which weighted the measurement uncertainty. The TSSp solvus in the two banks were obtained as,

$$C^{\mathrm{ND}}_{[D]^{\alpha}} = 19146\exp(\frac{-18407 \pm 1228}{RT}) \tag{3.8a}$$

$$C^{\mathrm{RD}}_{[D]^{\alpha}} = 11700\exp(\frac{-20420 \pm 1435}{RT}) \tag{3.8b}$$

The value of the energy term Q_{p} for precipitation was found to be smaller than the stress-free value reported in the literature; this is true when compared with studies which used the bulk-average method [15, 60, 65, 68, 70, 72] and for studies which only included a subset of grains [28, 71]. The average Q_{p} value (average value of two banks) in this experiment, which has 78 MPa stress applied along the RD, is $\sim$4 kJ mol^{-1} lower than the stress-free value. Another experiment done by Colas et al. [28] which has 160 MPa stress applied along the TD, the Q_{p} is $\sim$12 kJ mol^{-1} lower than the stress-free value. These results imply the Q_{p} is

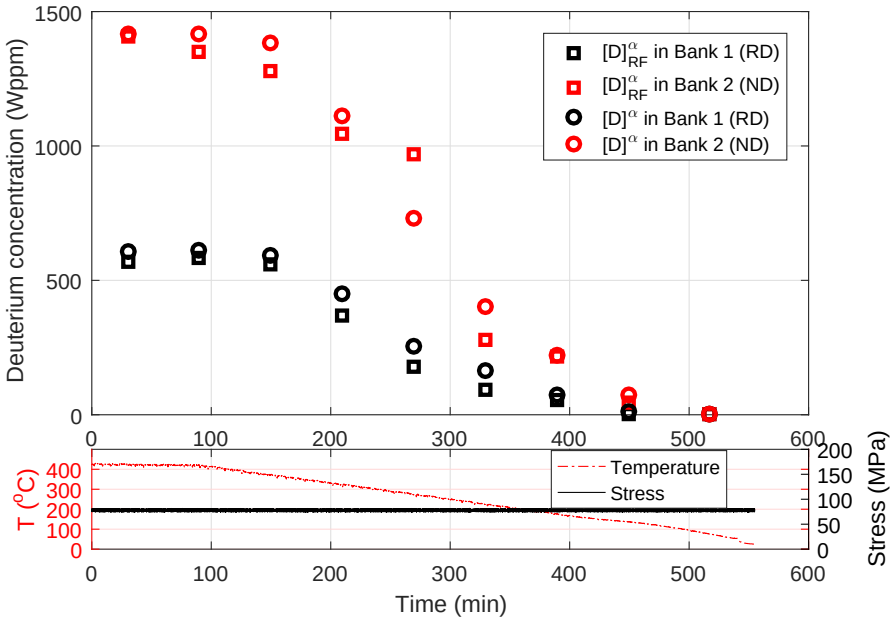

(a)

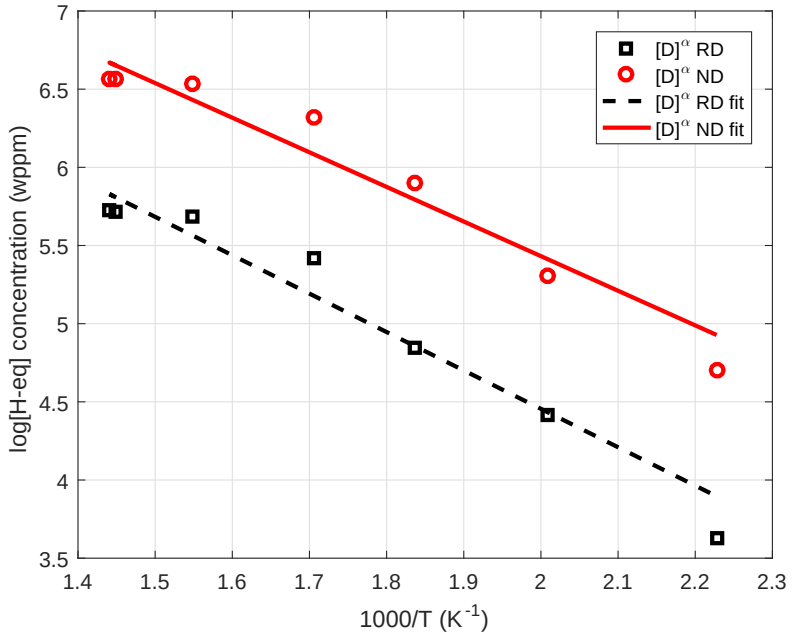

(b)

Figure 3.12: (a) Evolution of the deuterium concentration in the zirconium solid solution. The square and circle marker represents the $[D]^{\alpha}_{\mathrm{RF}}$ and $[D]^{\alpha}$ while the red and black color represents the ND and the RD bank, respectively. The uncertainties are within the size of the data marker. A subplot shows the corresponding temperature and stress value for each point. (b) Arrhenius fit of the $[D]^{\alpha}$ (represented in hydrogen-equivalent concentration) in the zirconium solid solution. The dashed and the solid line represents the fitting line for the data in the RD and the ND bank, respectively.

inversely proportional to the externally applied stress. This also suggests that the applied tensile stress increase the amount of hydrogen in the solid solution for the grain subsets studied. The Q_{p} value decreased by the stress is in disagreement with Puls model (Eqn. (2.16)). As discussed in Section 2.3.2, a 1860 MPa stress at 250 °C only reduced the Q_p by 129 $\mathrm{J\,mol^{-1}}$.

The Puls model (Eqn. (2.16)) was numerically evaluated to estimate the influence of stress on the Q_{p}. Because the specimen was a polycrystal, the unconstrained transformation strain was calculated by substituting Eqn. (2.8) into Eqn. (2.3). The Kearns factor f_i is 0.65 in the ND, 0.27 in the TD and 0.07 in the RD as discussed in Section 3.1.1. Eqn. (2.16) (Puls solvus model) was reproduced here for the convenience,

$$C_{\mathrm{TSSp}}^{\mathrm{Con},\sigma} = C_{\mathrm{TSSp}}^{\mathrm{Con}} \exp\Big(\frac{xp^{\mathrm{h}} \cdot \bar{V}_{\mathrm{H}}^{\alpha} - \bar{V}_{\mathrm{Zr}}^{\alpha} \sigma_{ij} \cdot \varepsilon_{ij}^{T}}{xRT}\Big) \tag{3.9}$$

. If rewrite in a simplified form,

$$C_{\mathrm{TSSp}}^{\mathrm{Con},\sigma} = C_{\mathrm{TSSp}}^{\mathrm{Con}} \exp\Big(\frac{-\Delta Q_{\mathrm{p}}}{RT}\Big) \tag{3.10}$$

where ΔQ_{p} is the amount of Q_{p} value changed by the externally applied stress. The adopted numerical value for each variable in Eqn. (3.9) is,

$$\bar{V}_{\mathrm{H}}^{\alpha} = \begin{bmatrix} 0.033 & 0 & 0 \\ 0 & 0.033 & 0 \\ 0 & 0 & 0.054 \end{bmatrix},$$

$$\bar{V}_{\mathrm{Zr}}^{\alpha} = 14.0024 \times 10^{-6}\ \mathrm{m^3\,mol^{-1}},$$

$$\varepsilon_{ij} = \begin{bmatrix} 0.039 + 2.2845 \times 10^{-5} T & 0 & 0 \\ 0 & 0.0445 + 2.2086 \times 10^{-5} T & 0 \\ 0 & 0 & 0.0549 + 2.0644 \times 10^{-5} T \end{bmatrix},$$

$$\sigma_{ij} = \begin{bmatrix} \sigma_{11} & 0 & 0 \\ 0 & \sigma_{22} & 0 \\ 0 & 0 & \sigma_{33} \end{bmatrix} \text{ and}$$

$$p^{\mathrm{h}} = \frac{1}{3} \begin{bmatrix} \sigma_{11}+\sigma_{22}+\sigma_{33} & 0 & 0 \\ 0 & \sigma_{11}+\sigma_{22}+\sigma_{33} & 0 \\ 0 & 0 & \sigma_{11}+\sigma_{22}+\sigma_{33} \end{bmatrix}$$

. x is a function of temperature and was determined using the boundary between the δ and $\delta + \alpha$ phase in the binary Zr-H phase diagram [5]. In this experiment, $\sigma_{11} = 78$ MPa and $\sigma_{22} = \sigma_{33} = 0$. For the experiment done by Colas et al. [28], $\sigma_{22} = 160$ MPa and $\sigma_{11} = \sigma_{33} = 0$. Figure 3.13 shows the calculated ΔQ values respective to different σ_{ij} for the two experiments. Effect of the same σ_{ij} value applied along the different sample orientation is also shown in the figure. The externally applied stress decreases the Q_{p} at low temperature and increases it at high temperature; the transition temperature is at $580 - 610$ K depends on the direction and magnitude of the applied stress. The calculated ΔQ is -9 to 16 J mol^{-1} which is much smaller than the result observed in this experiment and by Colas et al. [28].

From the result of this experiment, we learn that the amount of hydrogen in the studied grain subsets could be increased by externally applying a tensile stress on the material. These grain subsets, however, could not be identified under the condition of this instrument. This observation is contradictory to Puls model which states the influence of external stress on hydrogen solvus is negligible. The average bulk behavior of the δ-phase is unknown. For the next in situ experiment, the studied grain subsets were identified by performing a texture analysis on a full Debye-Scherrer ring.

3.2.3 Isostress thermal-cycle experiment

This experiment was conducted at beamline 1-ID at APS. The tensile specimen was thermal-cycled between 400 °C and 150 °C with heating/cooling rate of 25/1 °C min^{-1}. A constant 105 MPa tensile stress was applied along the RD of the sample throughout the thermal-cycle process. The average hydrogen concentration contained in this sample was

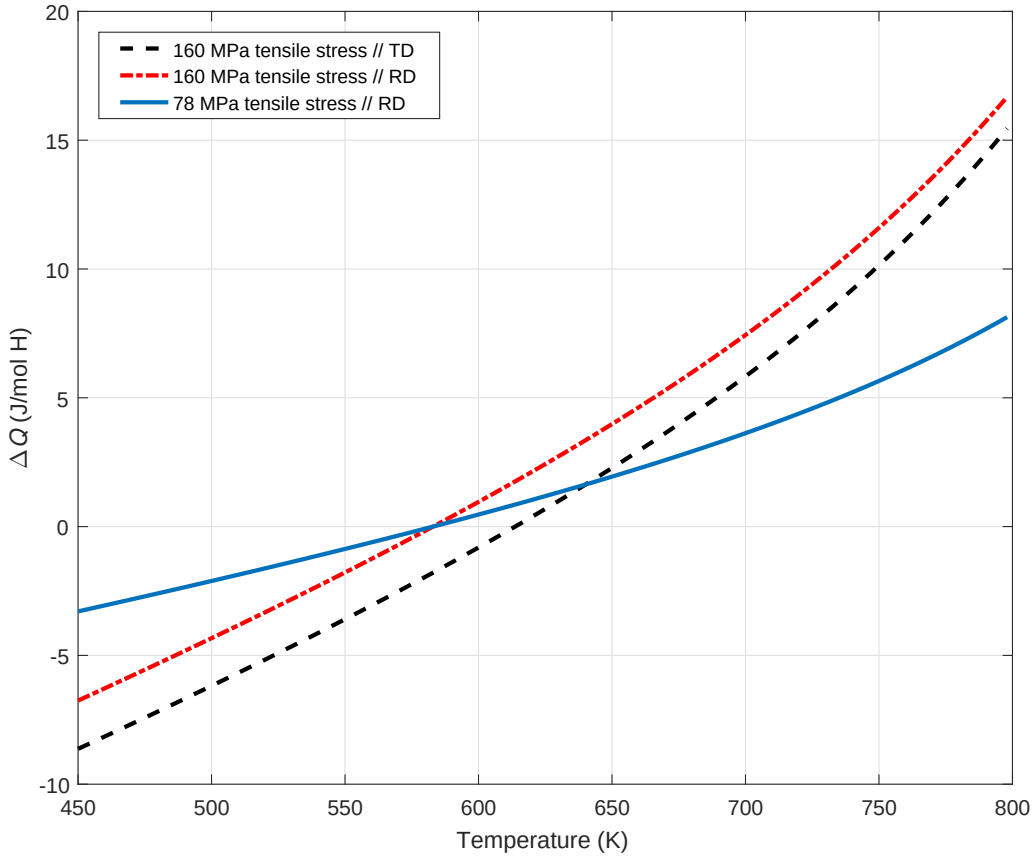

Figure 3.13: The change of Q_{p} due to the external applied tensile stress, calculated by Eqn. (3.9). The blue solid line, red dot-dash line and the black dash line represents the result for a 78 MPa stress applied along the RD, a 160 MPa stress applied along the RD and a 160 MPa stress applied along the TD, respectively. This figure is reprinted from the Fig. 4 in Ref. [13].

520 wppm. A 150×150 µm^2 beam size was used. Each diffraction data is an average of 10 exposures each has 0.4 second beam exposure time. The thermomechanical history of this experiment is shown in Fig. 3.14.

We first studied the texture relationship between the δ-hydride and the α-Zr phase. The texture is the measurement of the grain fraction that oriented in a specified direction. This can be qualitatively determined by examining the intensity distribution of a reflection around the Debye-Scherrer ring (Fig. 3.5) or quantitatively measured by integrating a 10° span sector azimuthally around the ring. Fig. 3.15 shows the azimuthal intensity distribution

of three reflections. The result of α-Zr $\{0002\}$ and α-Zr $\{10\bar{1}0\}$ reflections agree with the basal pole figure shown in Fig. 3.1. From Fig. 3.1, the majority of the Zr grains orient their c-axis $\sim 30°$ tilted from the ND toward to the TD, and their a-axis parallel to the RD and TD. The result in Fig. 3.15b further concludes that the majority of the Zr grains orient their a-axis parallel to the RD and some of them have their a-axis parallel to the TD. The α-Zr$\{0002\}$ in Fig. 3.15a shows no intensity in the panel 1 and 3 detectors because there are a very few Zr grains orient their c-axis parallel to the RD. The intensity distribution of the $\delta\{111\}$ reflection in Fig. 3.15c shows a strong relationship with the α-Zr$\{10\bar{1}0\}$ reflection. This suggests that the majority of the δ-phase grains studied in this experiment obey the relationship of $\{111\}_\delta \parallel \{10\bar{1}0\}_\alpha$. In other words, the majority of hydride responsible for the δ (111) reflection are those precipitated in α-Zr grains which oriented their a-axis along the RD. A direct observation for this relationship is shown in Fig. 3.16. It can be seen in Fig. 3.16 that the intensity of the $\delta\{111\}$ reflection is inversely proportional to the $\alpha\{10\bar{1}0\}$ intensity. The hydride phase dissolves and reduces the $\delta\{111\}$ intensity; the dissolved hydride phase

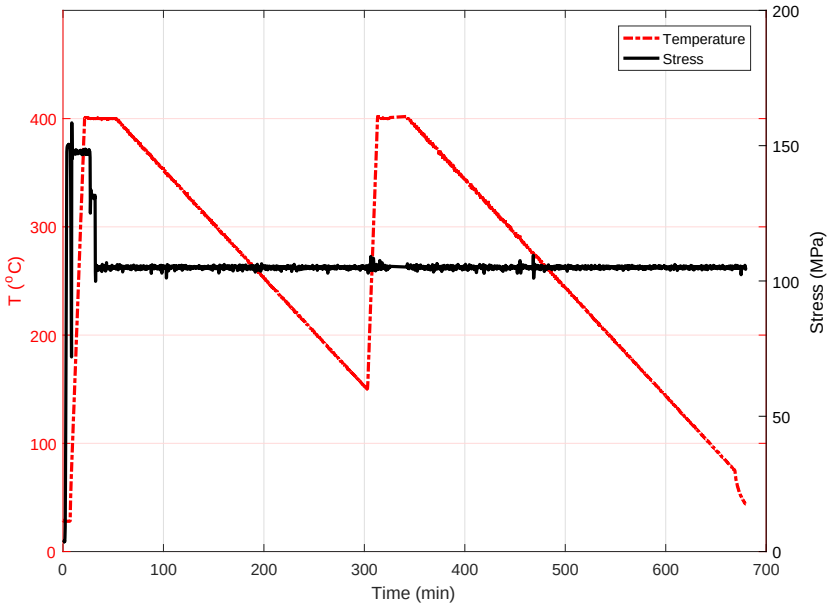

Figure 3.14: The thermal and mechanical history throughout the in situ thermal-cycle experiment. The black-solid line and the red-dashed line represents the stress and the temperature value, respectively.

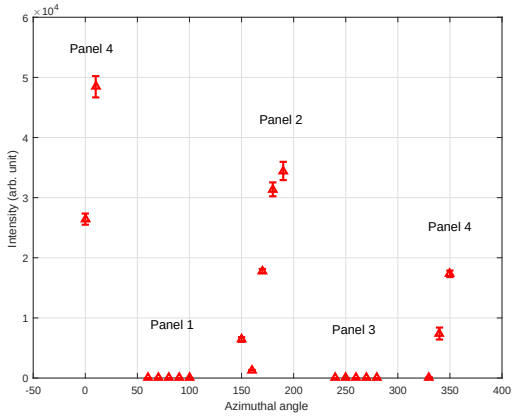

(a) α-Zr $\{0002\}$

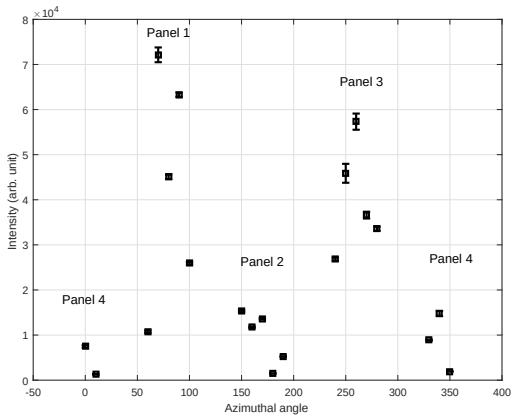

(b) α-Zr $\{10\bar{1}0\}$

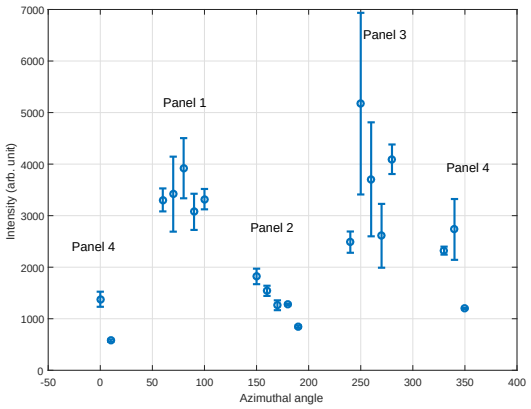

(c) δ $\{111\}$

Figure 3.15: Azimuthal intensity distribution for the reflection of (a) α-Zr $\{0002\}$, (b) α-Zr $\{10\bar{1}0\}$ and δ $\{111\}$. The diffraction measurement was done on RD-TD plane of the specimen. The gap between each panel detector is $\sim 40^{\circ}$ as schematically shown in Fig. 3.5.

transformed into α-Zr grains with the a-axis along the RD thus increasing the α-Zr$\{10\bar{1}0\}$ intensity. The opposite trend occurred when the δ-hydride phase precipitated.

As discussed in Section 3.2.2, the sampled grain subsets depend on the studied δ reflection. In this synchrotron experiment, it is known that regardless of which δ reflection picked, it always obeys the relationship of $\{111\}_\delta \parallel \{10\bar{1}0\}_\alpha$. For example, when studied $\{111\}_\delta$ at the angular section parallel to the RD, the sampled Zr grains have a-axis parallel to the RD. Similarly, when studied $\{220\}_\delta$ at the angular section parallel to the RD, the sampled Zr grains have a-axis titled $\sim 35°$ away from the RD. The α-Zr grain subset being sampled is schematically shown in Fig. 3.17. The direction of the externally applied stress is also shown in the figure.

The amount of hydrogen in the solid solution can again be calculated using the same procedure described in Section 3.1.3 and 3.2.2. Fig. 3.18 shows an example for the intensity evolution of the $\delta\{220\}$ throughout the thermal-cycle process. The amount of hydrogen in the solid solution was first calculated using the $\delta\{220\}$ and $\delta\{111\}$ reflection intensity that

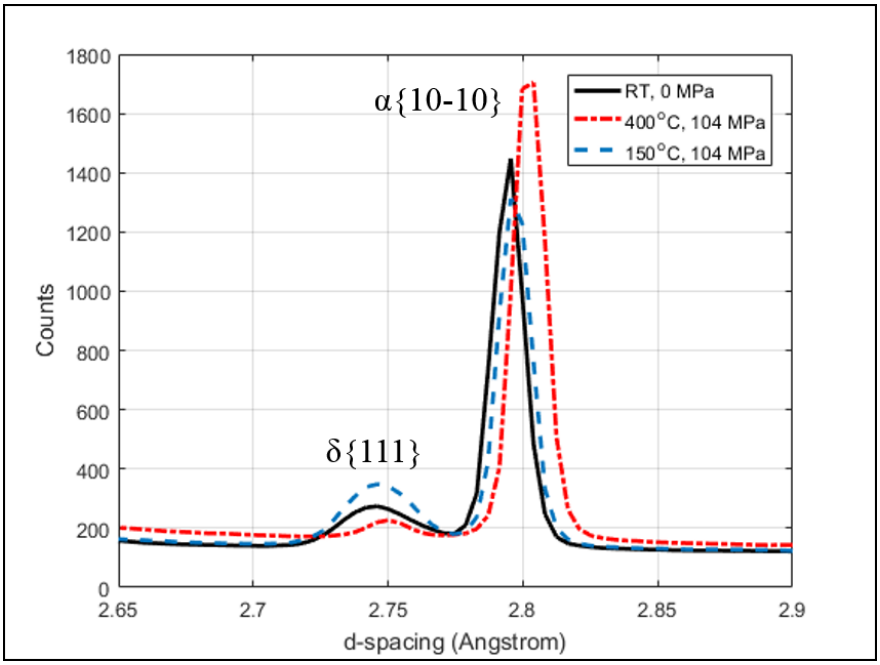

Figure 3.16: Details of the $\delta\{111\}$ and $\alpha\{10\bar{1}0\}$ diffraction spectrum taken under different thermomechanical conditions. The black solid line, red dot-dashed line and the blue dashed line represents the spectrum taken at the room temperature with 0 stress, at 400 °C with a 105 MPa stress and at 150 °C with a 105 MPa stress, respectively.

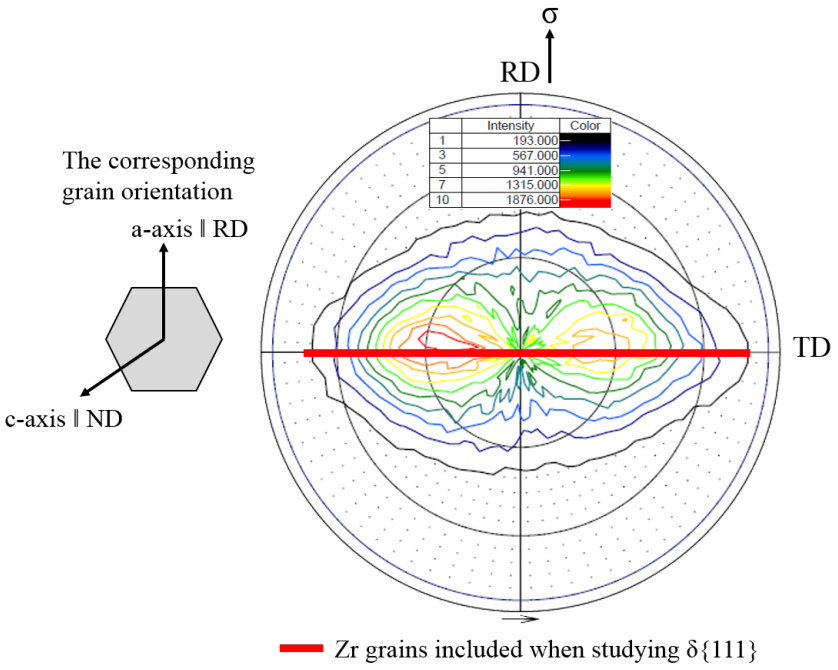

(a)

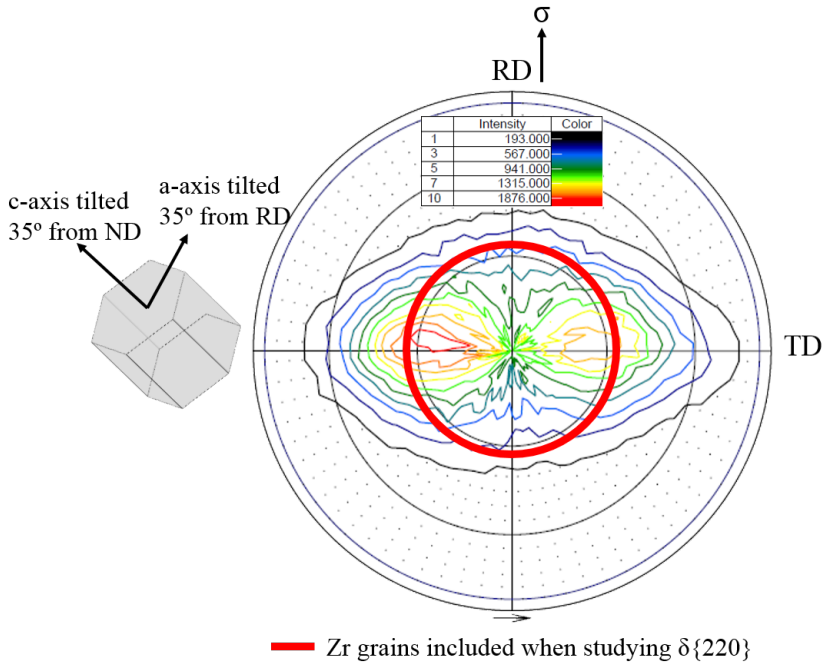

(b)

Figure 3.17: The α-Zr grain subset being sampled when studying different δ reflections. The case when (a) studying $\delta\{111\}$ and (b) studying $\delta\{220\}$. The sampled Zr grains are shown by the thick red line.

were integrated over the entire Debye-Scherrer ring. The temperature dependence of the hydrogen amount in the solid solution was described using the Arrhenius equation (Eqn. (2.18)). The numerical results are summarized in Table. 3.2.

The result in Table 3.2 shows that the Q_p is higher when studied the $\delta\{111\}$ reflection. Also, when Q_p is measured using the $\delta\{220\}$ reflection, the value is lower than the stress-free Q_p value which is also listed in Table. 3.2. The Q_p falls in the stress-free range when using the $\delta\{111\}$ reflection. This suggests that the effect of stress depends on the sampled grain subsets. Examining this result together with Fig. 3.17, demonstrates the hydrogen solvus is lessly affected in grains with a low tensile stress along the c-axis of the zirconium lattice. This is further supported by integrating 20-degree span $\delta\{220\}$ reflection along different angular sections on a Debye-Scherrer ring. This analysis is based on a fact that the stress component on the c-axis of a zirconium lattice varies for different integrated sectors. Fig. 3.19 shows this analysis schematically. The amount of hydrogen in each grain subset was calculated using

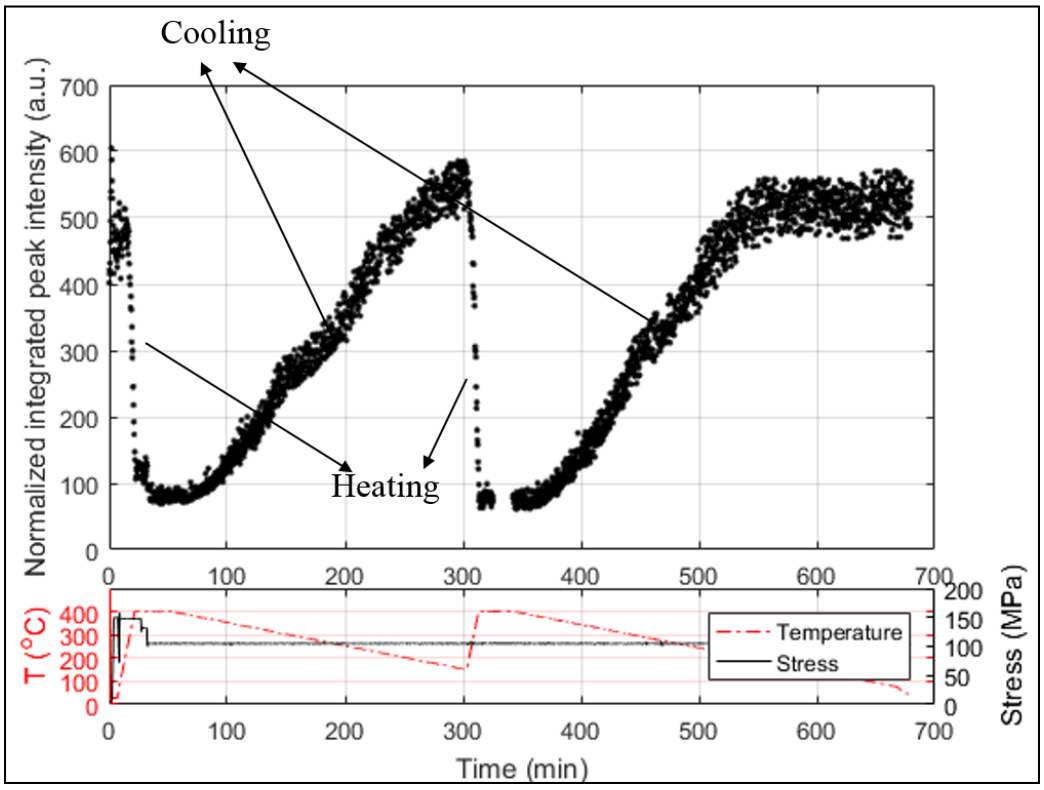

Figure 3.18: $\delta\{220\}$ intensity evolution throughout the thermal-cycle process. The subplot shows the corresponding thermal-mechanical history.

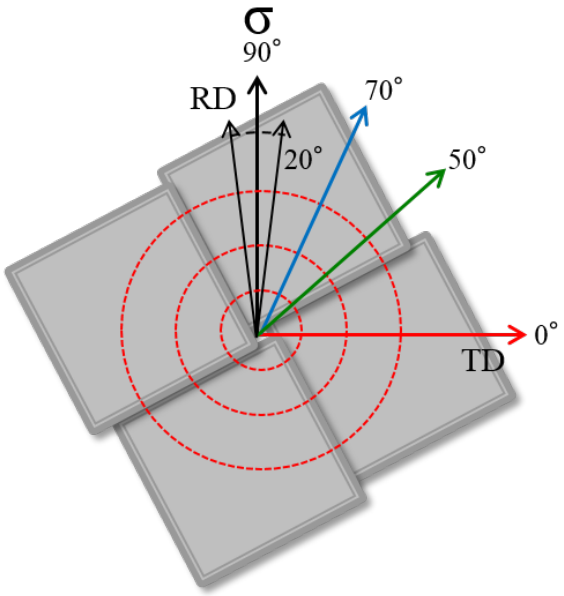

Figure 3.19: Schematically show the integration process for sampling different grain subsets.

the evolution of the $\delta\{220\}$ reflection intensity. Evolution of the hydrogen concentration as a function of the temperature was described using the Arrhenius equation (Eqn. (2.18)). Fig. 3.20 shows the data as well as the linear fitting line. Table 3.3 summarizes the measured Q value of each grain subset. The magnitude of the tensile stress component along the c-axis for each grain subset has been estimated based on the geometry shown in Fig. 3.17; these stress values are also listed in Table 3.3.

Examining the result in Table 3.3, it is observed that the higher the tensile stress on the c-axis, the lower the Q value is. From Eqn. (2.18), this suggests that the hydrogen concentration in the solid solution is higher for the grain subsets which have higher tensile

Table 3.2: Summary of Q_p and Q_d values measured using the reflection intensity that was integrated over the entire Debye-Scherrer ring.

Reflection	First Cycle		Second Cycle	
	Q_d (J/mol)	Q_p (J/mol)	Q_d (J/mol)	Q_p (J/mol)
$\delta(111)$, full ring	33923±308	27180±308	37021±906	29382±341
$\delta(220)$, full ring	18270±2810	21224±523	30827±1105	27194±391
External stress free [15, 16, 28, 60, 65, 68–72]	32117 - 45610	24320-34468	-	-

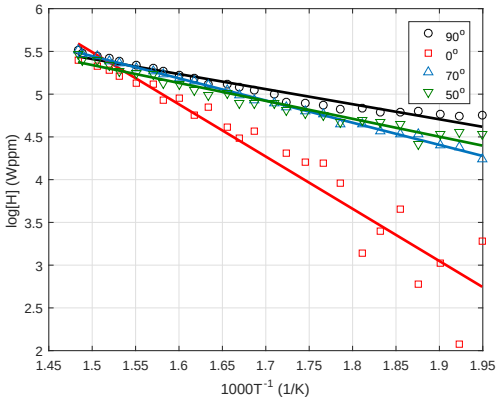

(a) First heating

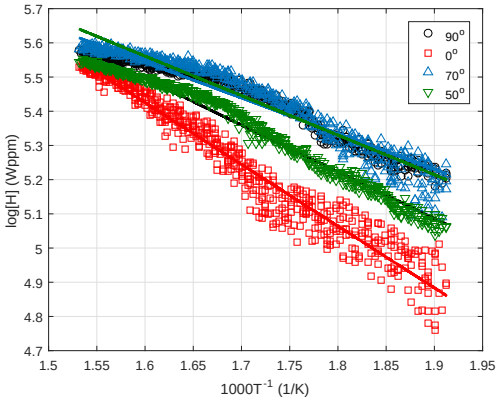

(b) First cooling

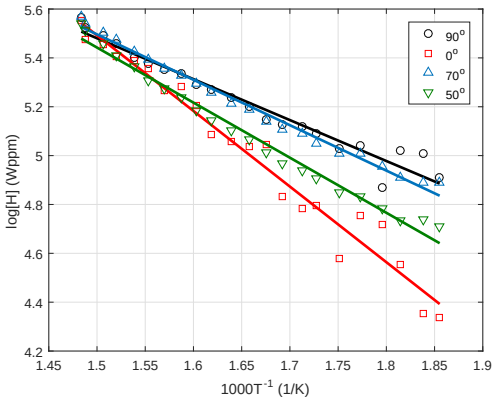

(c) Second heating

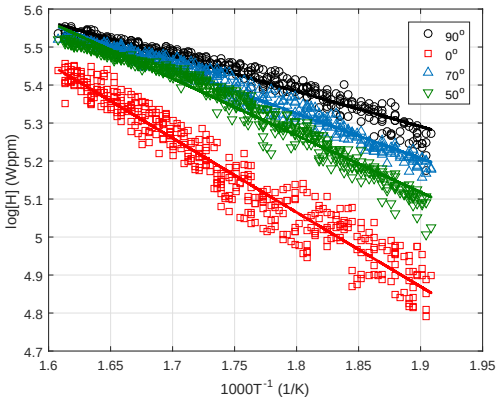

(d) Second cooling

Figure 3.20: Hydrogen concentration in the four sampled grain subsets as a function of temperature. The grain subset was sampled by integrating the segment shown in Fig. 3.19. The red-square, black-circle, blue-triangle and green inverted-triangle marker represents the 0°, 90°, 70° and 50° segment, respectively.

stress on the c-axis. It is the same result as shown in Table 3.2. Because the hydrogen reservoir is conserved, this result also suggests that the hydrogen diffuses from grain subsets which have lower stress on the c-axis to those which have higher stress. This hydrogen redistribution among the grain subsets only occurs when the external stress is present at elevated temperature.

This effect of crystalline orientation has also been observed by Vizcaíno *et al.* [59]. These authors observed that the precipitation temperature for hydride was increased the most for grains which had the largest stress along the c-axis. This is the same observation as in this research which the external stress effect is maximized for specific grain subsets. However, the observation by Ref. [59] implies that the external stress assists hydride precipitation and decreases the hydrogen concentration in the solution; this increases the Q_{p} value for these grains and is opposite to the result listed in Table 3.3.

3.3 Summary of experimental observation

The first in situ experiment suggests that the hydride phase is relatively stable under the isothermal condition and is independent of the external stress. The second and the third in situ experiments suggest that the effect of the external stress depends on the crystalline orientation; zirconium grains which have the higher tensile stress on the c-axis have higher hydrogen concentration in the solid solution. This also reflects on the increased Q value in these grains. Fig. 3.21 summarizes the Q_{p} values measured in this study by in situ neutron (Section 3.2.2) and synchrotron diffraction (Section 3.2.3) and the value measured by Colas *et al.* [28]. All data integrated the $\delta(220)$ reflection intensity over a 20° sector along the external stress direction. An approximate linear relationship between the Q_{p} and the external stress is observed. This suggests that the external stress increases the hydrogen concentration in the sampled grain subset. Since the hydrogen content is conserved, this also implies that the diffusion of hydrogen from one grain subset to another occurs, causing hydrogen redistribution. A linear fit for the three Q_{p} values is also shown in Fig. 3.21. The interpolated Q_{p} value at $\sigma = 0$ is ~ 27300, which agrees with the stress-free experimental data [15, 16, 28, 60, 65, 68–72]. This gives confidence for the experimental observation but also indicates

that there is a disagreement between the current theory and the experiment as discussed in Section 2.3. Like the other published works which mentioned this inconsistency [28, 59], it is difficult to find a physical reason for this discrepancy solely based on the experimental results. Simulations are performed to resolve this inconsistency. The purpose is to support this experimental observation and to understand the physics reason for the inconsistency between the current model and the experimental result. The simulation method and the result is described in Chapter 4.

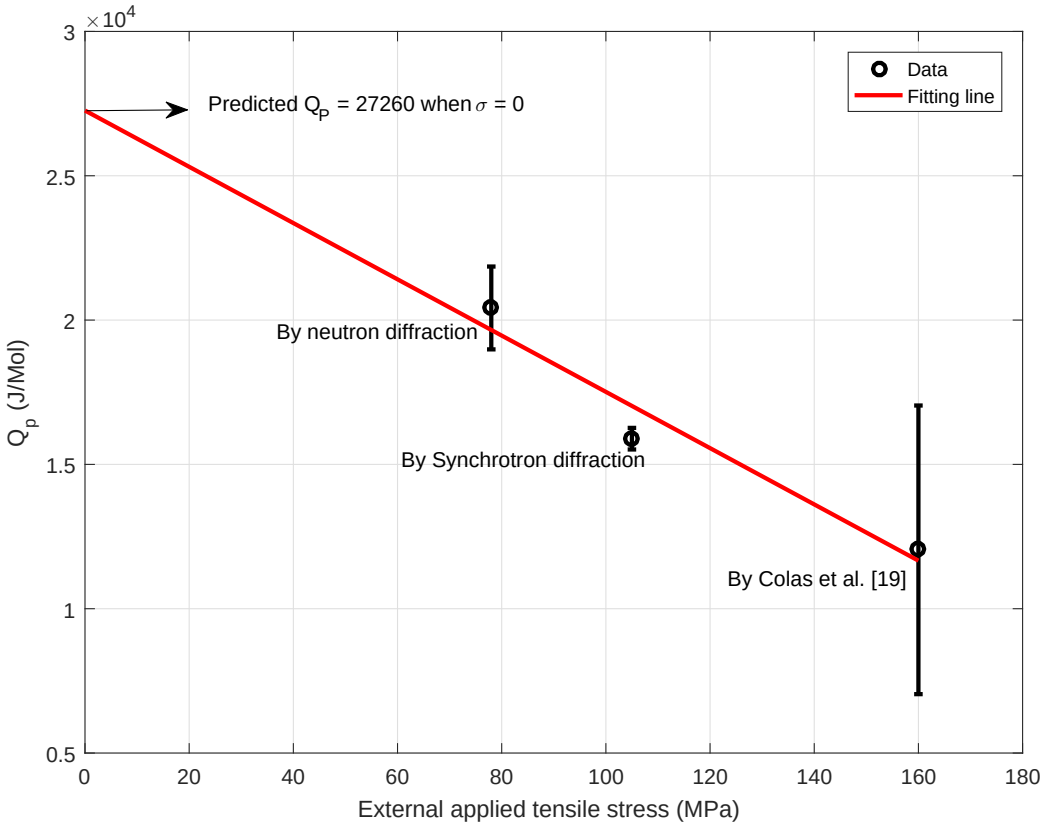

Figure 3.21: The hydride precipitation activation energy Q_{p} as a function of the external tensile stress. The black circle and the red solid line represented the experimental data and the fitting line, respectively.

Table 3.3: Summary of Q_p and Q_d values for each sector with applied stress.

Orientation	First Cycle		Second Cycle		Calculated stress on the c-axis (MPa)
	Q_d (J/mol)	Q_p (J/mol)	Q_d (J/mol)	Q_p (J/mol)	
90°	20116±2178	15891±374	31368±3932	15614±415	61
70°	26010±2810	17604±523	35719±1105	21375±475	55
50°	34302±1330	22684±424	56486±3358	28770±673	46
0°	84572±11307	34715±789	68366±8979	53042±1870	0
External stress free [15, 16, 28, 60, 65, 68–72]	32117 - 45610	24320-34468	-	-	

CHAPTER 4

PHASE-FIELD SIMULATION

4.1 Computational method

4.1.1 Evolution equations and their implementation

Phase-field methods have recently became a powerful approach to model mesoscale microstructure evolution in materials [82]. The methods enable prediction of complex morphological evolution without mathematically tracking the interface position by reducing the total free energy of the system. Phase-field methods have been extensively applied to study zirconium-hydrogen system. Ma *et al.* [83] studied the nucleation and growth of the γ-hydrides in a α-Zr phase. They observed that the morphology and the orientation of the hydride particle significantly depend on the strain energy of the system and the externally applied load. A similar research was done by Ma *et al.* [84] to study the heterogenous nucleation of γ-hydride at grain boundaries. Ma *et al.* [85] studied the effect of the non-uniformly applied stress by simulating the diffusion and precipitation of the γ-hydrides around a notch tip in a loaded cantilever. The hydrogen was observed diffuse from the lower hydrostatic tensile stress region to the higher hydrostatic tensile stress region. Additional research included the effect of plasticity by adding an additional non-conserved phase-field variable [86, 87]. The misfit stress induced during the hydride particle formation was significantly reduced by plastic deformation. Two phase-field model papers published by Thuinet *et al.* [88, 89] modeled the behavior of the ζ-hydride phase; Their result indicated the hydride particle orientation might be determined at the early nucleation stage before the ζ-phase transformed to relatively stable δ and γ phase. A more recent research by Bair *et al.* [44] also suggested that the ζ-hydride is an intermediate path for the final stable hydride phase.

Most of the phase-field work focuses on qualitative morphology studies. Although stress and strain in the system have be quantitatively described, time, length scale and the conserved variable are not. This is due to the phenomenological constants in the Landau-type free energy polynomial [82]. Therefore, Shi and Xiao [90] and Xiao *et al.* [91] developed a fully quantitative free energy function by quantifying the phenomenological constants. The temperature dependency was also included. Their results were in reasonable agreement with the experimental data. We used a different approach in this research to achieve a fully quantitative simulation. This is described and demonstrated in this chapter.

In this research, phase-field modeling was performed using Hyrax. Hyrax is a CALPHAD-based phase-field code developed specifically for studying the zirconium-hydrogen binary system, including hydrogen in the solution and as the δ-hydride phase. Hyrax was developed by a research group at the University of Michigan at Ann Arbor funded by Consortium for Advanced Simulation of LWRs (CASL) [92]. Hyrax was built on a finite element framework, the Multiphysics Object-Oriented Simulation Environment (MOOSE) [93]. MOOSE includes libMesh and PETSc to solve the linear and nonlinear finite element problems. Hyrax inherited many physical modules from MOOSE, including the solid mechanics and phase-field modules which are key components for running a phase-field modeling. The special aspect of Hyrax is the usage of a CALPHAD (Calculation of Phases Diagrams) based free energy function, which allows Hyrax perform a fully quantitative simulation. The application of the CALPHAD based free energy function is briefly discussed in Section 4.1.2 while more details can be found in Ref. [94].

Phase-field simulations predict the compositional and structural microstructure evolution using a set of phase-field variables. There are two types of phase-field variables, conserved and non-conserved. The time evolution of the microstructure is governed by a set of phase field equations, the Cahn-Hilliard and the Allen-Cahn equations, that couples two different type of variables [82]. The conserved variable satisfies the local conservation condition. For zirconium-hydrogen binary system studied in this research, the conserved variable is the hydrogen atomic fraction χ_{H}. The time evolution of the hydrogen atomic fraction in the

system is governed by the Cahn-Hilliard equation [95],

$$\frac{\partial \chi_{\mathrm{H}}(r,t)}{\partial t} = \nabla \cdot [M \nabla \Big(\frac{\partial g_{\mathrm{chem}}}{\partial \chi_{\mathrm{H}}} - \kappa_{\chi_{\mathrm{H}}} \nabla^2 \chi_{\mathrm{H}} + \frac{\partial F_{\mathrm{strain}}}{\partial \chi_{\mathrm{H}}} \Big)] \tag{4.1}$$

where χ_{H} is the atomic fraction of hydrogen in the system, M is the mobility of hydrogen which is assumed isotropic in this study, g_{chem} is the bulk free energy density, F_{strain} is the strain energy contribution and κ_χ is the gradient energy coefficient. Phase variable η_p is the non-conserved variable in this modeling; p represents the α-Zr and the δ-hydride phases. The Allen-Cahn equation governs the evolution of the phase variable η_p [96],

$$\frac{\partial \eta_p(r,t)}{\partial t} = -L(\frac{\partial g_{\mathrm{chem}}}{\partial \eta_p} - \kappa_{\eta_p} \nabla^2 \eta_p + \frac{\partial F_{\mathrm{strain}}}{\partial \eta_p}) \tag{4.2}$$

where η_p is the phase variable, L is the kinetic coefficient for η_p and κ_{η_p} is the gradient energy coefficient for the η_p. In this study $p = 1, 2$ with $\eta_1 = 0$ and $\eta_2 = 1$ represents the α-Zr and the δ-hydride phase, respectively. The α/δ interfacial energy is determined by κ_χ and κ_η. A constants κ_χ and κ_η yield different interfacial energies at a different temperatures. Therefore, κ_χ and κ_η are determined so that the α/δ interfacial energy is $\sim 500\ \mathrm{mJ\,m^{-2}}$ at each temperature (e.g., $\kappa_\chi = \kappa_\eta = 3.6 \times 10^{-5}\ \mathrm{mJ\,m^{-1}}$ at 600 K), which is larger than used by Bair *et al.* [44]. The interfacial energy only affects the hydride particle morphology but not the equilibrium hydrogen composition in the two phases. A higher interfacial energy also yields a wider interface which decreases required mesh resolution, increasing the computational efficiency.

The bulk free energy density g_{chem} is a combination of two single phase energies [94],

$$g_{\mathrm{chem}} = \frac{1}{\Omega_0}[(1 - h(\eta_p))G^{0,\alpha}_{\mathrm{mix}}(\chi, T) + h(\eta_p)G^{0,\delta}_{\mathrm{mix}}(\chi, T)] \tag{4.3}$$

where $G^{0,\alpha}_{\mathrm{mix}}$ is the molar free energy of mixing of hydrogen with α-zirconium phase, $G^{0,\delta}_{\mathrm{mix}}$ is the molar free energy for the δ-hydride phase and $\Omega_0 = 1.4 \times 10^{-5}\mathrm{m}^3/\mathrm{mol}$ is the molar volume for the α-zirconium phase. $h(\eta_p) = \eta_p^2(3 - 2\eta_p)$ is an interpolation function which increases from 0 to 1.

To solve Eqs. (4.1) and (4.2) using the finite element method (FEM), the weak forms

of the two equations were constructed [92]. First, the weighted integral residual of Eqs. (4.1) and (4.2) were constructed by multiplying with a test function ϕ_i. Integrating the second-order term by parts once and the fourth-order term by parts twice [97,98], Eq. (4.1) yields,

$$\begin{aligned}\Big(\frac{\partial \chi}{\partial t}, \phi_i\Big) &= -\Big(\kappa_i \nabla^2 \chi, \nabla \cdot (M \nabla \phi_i)\Big) - \left(M \nabla \Big(\frac{\partial g_{\text{chem}}}{\partial \chi} + \frac{\partial F_{\text{strain}}}{\partial \chi}\Big), \nabla \phi_i\right) \\ &+ \left\langle M \nabla (\kappa_\chi \nabla^2 \chi) \cdot \vec{n}, \phi_i \right\rangle - \left\langle M \nabla \Big(\frac{\partial g_{\text{chem}}}{\partial \chi} + \frac{\partial F_{\text{strain}}}{\partial \chi}\Big) \cdot \vec{n}, \phi_i \right\rangle \\ &+ \left\langle \kappa_\chi \nabla^2 \chi, M \nabla \phi_i \cdot \vec{n} \right\rangle\end{aligned} \tag{4.4}$$

where the inner product notation is used to represent the integrals. In addition, Eq. (4.2) yields,

$$\begin{aligned}\Big(\frac{\partial \eta_p}{\partial t}, \phi_i\Big) &= -L\Big(\kappa_{\eta_p} \nabla \eta_p, \nabla \phi_i\Big) - L\left(\Big(\frac{\partial g_{\text{chem}}}{\partial \eta_p} + \frac{\partial F_{\text{strain}}}{\partial \eta_p}\Big), \phi_i\right) \\ &+ L\Big\langle \kappa_\eta \nabla \eta_p \cdot \vec{n}, \phi_i \Big\rangle\end{aligned} \tag{4.5}$$

In MOOSE, each volume-integral term in the Eqn. (4.4) and (4.5) is an individual physics kernel and each surface-integral term is a boundary condition.

The hydrogen mobility M in the system was formulated to obey diffusion-controlled kinetics so that the hydrogen flux is calculated by Fick's law and must match the hydrogen flux described by the phase field model,

$$J = -D^i \nabla \left(\frac{\chi}{\Omega_0}\right) = -M^i \nabla \left(\frac{1}{\Omega_0} \frac{\partial G^{0,i}_{\text{mix}}}{\partial \chi}\right) \tag{4.6}$$

The mobility M in a single phase is calculated as,

$$M^i(\chi, T) = \frac{D^i(T)}{\partial^2 G^{0,i}_{\text{mix}} / \partial \chi^2}, i = \alpha \text{ or } \delta \tag{4.7}$$

In addition, the mobility M^{mix} at the interface is a combination of two single phase mobilities,

$$M^{\text{mix}}(\chi,\eta_p,T) = \Big(1-h(\eta_p)\Big)M^{\alpha}(\chi,T) + h(\eta_p)M^{\delta}(\chi,T) \tag{4.8}$$

The hydrogen diffusion coefficients $D^{\alpha}(T)$ and $D^{\delta}(T)$) were obtained in Ref. [99] and Ref. [100], respectively. Because of the primary kinetic limiting factor is M, the kinetic coefficient L in Eqn. (4.2) is choosen to be 10 times larger than M [44].

4.1.2 CALPHAD free energy approximation for the α-zirconium/δ-hydride system

The CALPHAD based molar free energies were formulated by Dupin *et al.* [101]. For the α-Zr phase,

$$\begin{aligned} G^{0,\alpha}_{\text{mix}}(\chi,T) &= \Big[(1-2\chi)G^{0,\text{hcp}}_{\text{Zr}}(T) + \chi G^{0,\text{hcp}}_{\text{ZrH}}(T)\Big] \\ &+ RT\left[\chi\ln\Big(\frac{\chi}{1-\chi}\Big) + (1-2\chi)\ln\Big(\frac{1-2\chi}{1-\chi}\Big)\right] \end{aligned} \tag{4.9}$$

and for the δ-hydride phase,

$$\begin{aligned} G^{0,\delta}_{\text{mix}}(\chi,T) &= \frac{1}{2}\Big[(2-3\chi)G^{0,\text{fcc}}_{\text{Zr}}(T) + \chi G^{0,\text{fcc}}_{\text{ZrH}_2}(T)\Big] \\ &+ RT\left[\chi\ln\Big(\frac{\chi}{2-2\chi}\Big) + (2-3\chi)\ln\Big(\frac{2-3\chi}{2-2\chi}\Big)\right] \\ &+ \left(\frac{3\chi^2-2\chi}{4(\chi-1)^2}\right)\Big[(\chi-1)L^0_{\text{fcc}}(T) + (1-2\chi)L^1_{\text{fcc}}(T)\Big] \end{aligned} \tag{4.10}$$

The formula of variables in Eqn. (4.9) and (4.10) are provided in Ref. [94, 101, 102] and are listed below,

$$G^{0,\text{hcp}}_{\text{Zr}}(T) = -7827.595 + 125.64905T - 24.1618T\ln(T) - 4.37791\times10^{-3}T^2 + 34971T^{-1}\ \text{J mol}^{-1},$$

$$G^{0,\text{fcc}}_{\text{Zr}}(T) = -227.595 + 124.74095T - 24.1618T\ln(T) - 4.37791\times10^{-3}T^2 + 34971T^{-1}\ \text{J mol}^{-1},$$

$$G^{0,\mathrm{gas}}_{\mathrm{H_2}}(T) = 8055.34 - 243.97T + 18.313T\ln(T) - 0.034513T^2 - 734182T^{-1}\ \mathrm{J\,mol^{-1}},$$

$$G^{0,\mathrm{hcp}}_{\mathrm{ZrH}}(T) = -45965 + 41.6T + G^{0,\mathrm{hcp}}_{\mathrm{Zr}}(T) + \frac{1}{2}G^{0,\mathrm{gas}}_{\mathrm{H_2}}(T)\ \mathrm{J\,mol^{-1}},$$

$$G^{0,\mathrm{fcc}}_{\mathrm{ZrH_2}}(T) = -170490 + 208.2T - 9.47T\ln(T) + G^{0,\mathrm{hcp}}_{\mathrm{Zr}}(T) + G^{0,\mathrm{gas}}_{\mathrm{H_2}}(T)\ \mathrm{J\,mol^{-1}},$$

$$L^0_{\mathrm{fcc}} = 14385 - 6T\ \mathrm{J\,mol^{-1}}\ \text{and}$$

$$L^1_{\mathrm{fcc}} = -106445 + 87.3T\ \mathrm{J\,mol^{-1}}$$

Eqn. (4.9) and (4.10) were reformulated in order to be applied in the finite element analysis. The natural logarithm term in Eqn. (4.9) and (4.10) may cause the free energy to be undefined near the boundary of χ_{H} at a range of [0,1]. Thus, the calculation on the bulk chemical free energy density (Eq. (4.3)) may require the calculation at a fraction which is not defined in one phase $G^{0,i}_{\mathrm{mix}}$ but is defined within the other. Also, because of the natural logarithm term, the $\partial G^{0,i}_{\mathrm{mix}}/\partial\chi$ exhibits highly nonlinear behavior near their composition boundaries. This causes the numerical solver attempt to calculate the free energy density at $\chi < 0$, which is non-physical.

In order to avoid Eqn. (4.1) becoming undefined, a new approximation was proposed by Jokisaari and Thornton [94]. The $G^{0,p}_{\mathrm{mix}}$ is composed of three subfunctions $\tilde{G}^{0,p}_{\mathrm{mix}}$ defined within the three χ subdomains. The subdomain boundaries $[\chi_{\mathrm{low}}\ \chi_{\mathrm{high}}]$ are chosen so that for $\chi > \chi_{\mathrm{high}}$ and $\chi < \chi_{\mathrm{low}}$, the subfunction $\tilde{G}^{0,p}_{\mathrm{mix}}$ is approximated by the second-order Taylor expansion of $G^{0,p}_{\mathrm{mix}}$, while $\tilde{G}^{0,p}_{\mathrm{mix}} = G^{0,p}_{\mathrm{mix}}$ when $\chi_{\mathrm{low}} \leq \chi \leq \chi_{\mathrm{high}}$. This yields a second-order differentiable $G^{0,p}_{\mathrm{mix}}$ across the whole composition and temperature range encountered in this work as long as the original CALPHAD molar free energies are second-order differentiable. The derivation detail are given in Ref. [94]. These authors suggested that the χ^i_{low} should be chosen approximately 10% less than the equilibrium concentration of α-Zr. Thus in this work, the $\chi_{\mathrm{low}} = 0.001$, $\chi_{\mathrm{high}} = 0.499$ were chosen for the α-phase and $\chi_{\mathrm{low}} = 0.5$, $\chi_{\mathrm{high}} = 0.665$ were chosen for the δ-phase.

4.1.3 Strain energy contribution

The mechanical behavior of the system was modeled using the linear elasticity, $F_{\text{strain}} = F_{\text{el}}$. The total strain at each element node is related to the displacement u such that,

$$\epsilon_{ij}^{\text{total}}(\mathbf{r}) = \frac{1}{2}[\frac{\partial u_i(\mathbf{r})}{\partial x_i} + \frac{\partial u_j(\mathbf{r})}{\partial x_j}] \tag{4.11}$$

The difference between the elastic strain and the total strain is determined as [88, 89],

$$\epsilon_{ij}^{\text{el}}(\mathbf{r}) = \epsilon_{ij}^{\text{total}}(\mathbf{r}) - \epsilon_{ij}^{0}(\mathbf{r}) \tag{4.12}$$

where $\epsilon_{ij}^{0}(\mathbf{r})$ is the local strain tensor which includes 1): the misfit strain between the α-Zr and the δ-hydride phase, and 2): the dilatation strain induced by interstitial hydrogen. The values of these two strain sources have been discussed in Section 2.2. ϵ_{ij}^{0} is approximated as a linear combination of these two contributions [92],

$$\epsilon_{ij}^{0}(\mathbf{r}) = [\big(1 - \eta^2(\mathbf{r})\big)\chi_{\text{H}}(\mathbf{r})\epsilon_{ij}^{\text{H}} + \eta^2(\mathbf{r})(1-\psi)\epsilon_{ij}^{\text{misfit}}] \tag{4.13}$$

where χ_{H} is the hydrogen atomic fraction, ϵ_{ij}^{H} is the dilation strain induced by hydrogen in solid solution, $\epsilon_{ij}^{\text{misfit}}$ is the temperature-dependent misfit strain between the zirconium and the hydride phase and ψ is an artificial factor that estimates the fraction of misfit strain being relieved by plastic deformation. $\psi = 0.5$ is chosen in this study. The total elastic strain energy of the system is then given as,

$$F_{\text{el}} = \frac{1}{2}\int_V C_{ijkl}(\mathbf{r})\epsilon_{ij}^{\text{el}}(\mathbf{r})\epsilon_{kl}^{\text{el}}(\mathbf{r})dV \tag{4.14}$$

where C_{ijkl} is the temperature and phase-dependent stiffness tensor which is given by,

$$C_{ijkl}(\mathbf{r}) = \Big[\Big(1 - h\big(\eta(\mathbf{r})\big)\Big)C_{ijkl}^{\alpha} + h\big(\eta(\mathbf{r})\big)C_{ijkl}^{\delta}\Big] \tag{4.15}$$

The temperature-dependent elastic modulus C_{ijkl}^{α} for the α-Zr is obtained in Ref. [25]. Currently, no temperature-dependent C_{ijkl}^{δ} data exists. Therefore, a constant C_{ijkl}^{δ} published in

Ref. [9] is used for all temperature range encountered in this work.

4.2 Result and Discussion

4.2.1 Validation of Hyrax

The fully quantitative free energy function allows Hyrax to calculate the effect of stress on hydrogen solubility in the α-Zr solution. In this section, Hyrax was first validated by comparing the modeling result with the experimental data. The FEA simulation was performed on multiple resources which include 1): the 16 cores quad-CPU Tempest 4400 Workstation owned by our research group, 2): the Illinois Campus Cluster and 3): the High-Performance Computing cluster in Idaho National Laboratory.

In all the following simulations, the conserved variable χ is described as χ_{H} since it is the hydrogen atomic fraction in the system that we studied. The width of the interface and the interfacial energy is controlled by the gradient energy coefficients κ_{η_p} and κ_{χ}. During the simulation, Hyrax uses adaptive scheme for both temporal and spatial evolution to significantly increase the computing efficiency without losing correctness of the simulation.

An example of phase-field simulation using Hyrax is shown in Fig. 4.1. The system in Fig. 4.1 is at 600 K and has an average hydrogen concentration of 600 wppm. We first consider the case when the strain energy is not included, $F_{\mathrm{el}} = 0$. The phase variable is set as 0 and 1 for the α-Zr and the δ-hydride phase, respectively. A hydride seed with a uniform composition of $\chi_{\mathrm{H}} = 0.6$ was placed in the middle of the system at $t = 0$ while the χ_{H} in the α-Zr phase was set as 0.1. Thus, the hydrogen was supersaturated in the α-Zr phase at $t = 0$. The nucleation algorithm was not implemented and the supersaturation drove the hydrogen flux toward the hydride seed as opposed to forming new hydride particles in the α-Zr matrix. The size of the δ-hydride seed increased until the two phases (δ and α) reached the equilibrium hydrogen concentration The equilibrium was defined when the δ-hydride seed size was invariant with respect to the t and the chemical potential was a constant value across the system. Equilibrium of the system was established and $t = t_{\mathrm{eq}}$. In addition to χ_{H}, the phase transformation in the system was successfully predicted by the evolution of

non-conserved variable η_p as shown in the bottom row of Fig. 4.1. The hydride seed grew isotropically when strain energy is not included ($F_{el} = 0$). This yielded a sphere particle, minimizing the interfacial energy in the system.

The strain energy is included in the next example using the Eqn. (4.14). The result is shown in Fig. 4.2. Because the strain induced by the δ-phase and interstitial hydrogen is anisotropic, this strain energy is also anisotropic in the system. The δ-hydride seed grew into an elliptical particle when the strain energy was included. The long and the short axis of the particle were parallel to the a-axis and c-axis of the α-Zr matrix, respectively. This is due to the larger lattice misfit strain along the c-axis compared to the a-axis (see Section 2.2). Thus, the hydride seed preferentially grew along the a-axis in order to reduce the total energy of the system.

Fig. 4.3a shows the area fraction of the hydride seed as a function of time for the system with $F_{el} = 0$. The growth rate of the δ-hydride phase increases when temperature decreases from 700 K, and reaches the maximum value when the temperature is near 485 K. Further

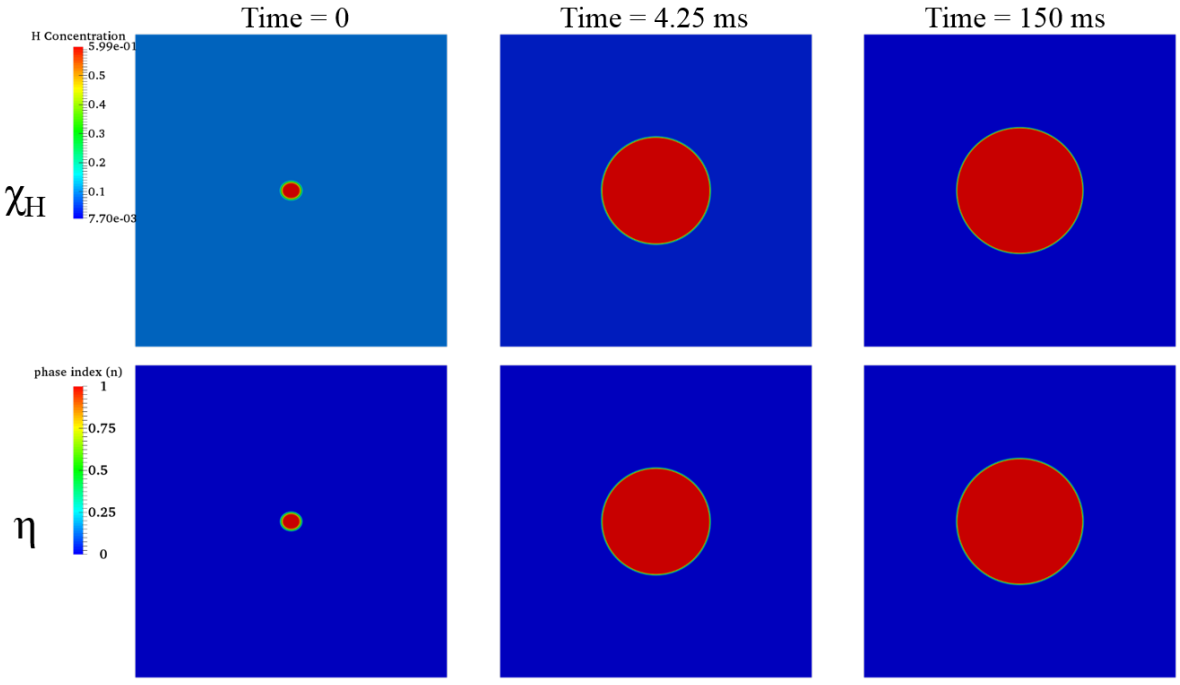

Figure 4.1: Evolution of χ_H and η predicted by Eqn. (4.1) and (4.2) at 600 K when $F_{el} = 0$.

decreases the temperature to below 485 K, however, decreasing the hydride growth rate. The growth of a nucleus is primarily affected by two terms, 1): the driving force for phase transformation, which decreases linearly with the increasing temperature, and 2): the mass transfer term (the diffusion of hydrogen atoms), which increases exponentially with the increasing temperature. As a result, the overall growth rate reaches the maximum value at an intermediate temperature. The growth kinetic can be described by fitting the data in Fig. 4.3a with the Avrami equation [103],

$$A_f^{\delta} = A_f^{\delta,t_{\text{eq}}} - A_f^{\delta,t_0}\exp(-Kt^n) \tag{4.16}$$

where A_f^{δ} is the area fraction of the δ-hydride, t is the time, $A_f^{\delta,t_{\text{eq}}}$ and A_f^{δ,t_0} are the area fraction at the time t_{eq} and t_0, respectively. K and n are the fitting parameters and represents the rate constant and the Avrami coefficient, respectively. When describing the area fraction, K is proportional to the square root of the particle growth rate. The fitted K corresponds

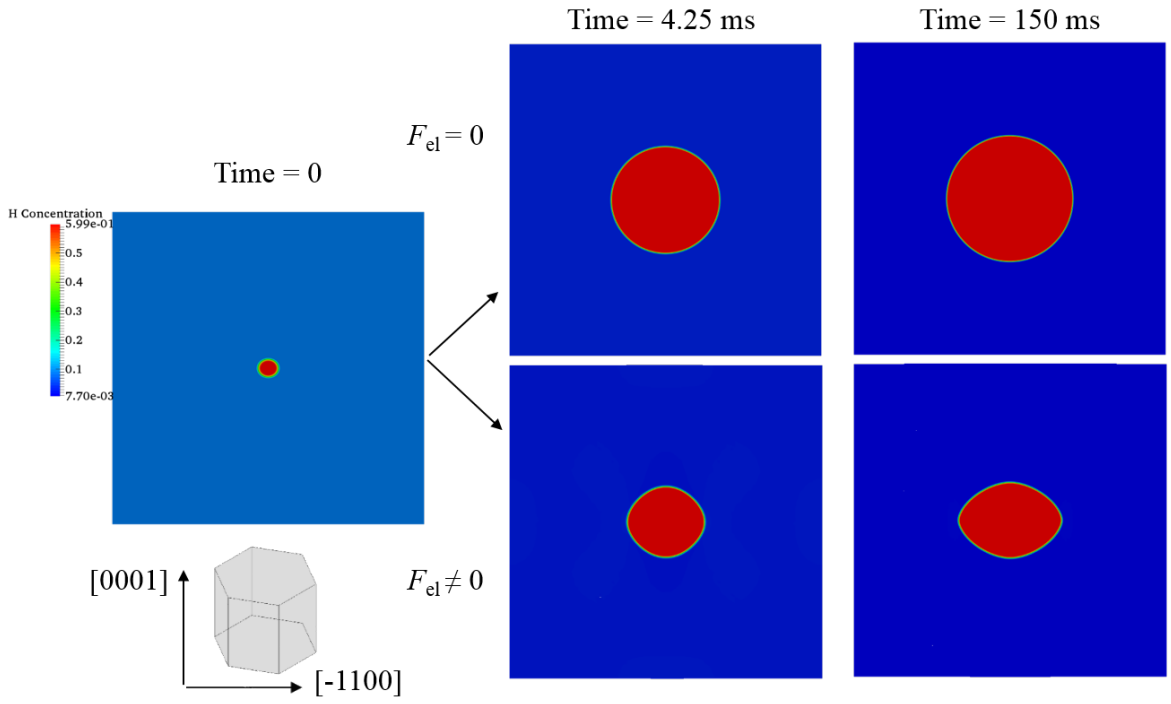

Figure 4.2: Evolution of χ_{H} when $F_{\text{el}} = 0$ and $F_{\text{el}} =$ Eqn. (4.14). A single h.c.p zirconium crystal specifies the orientation of this simulation.

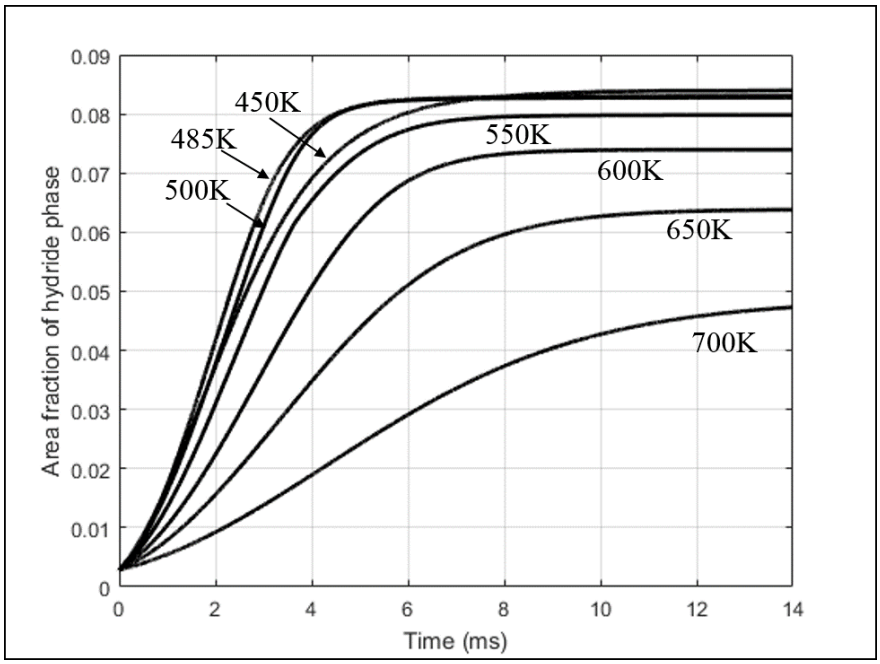

(a)

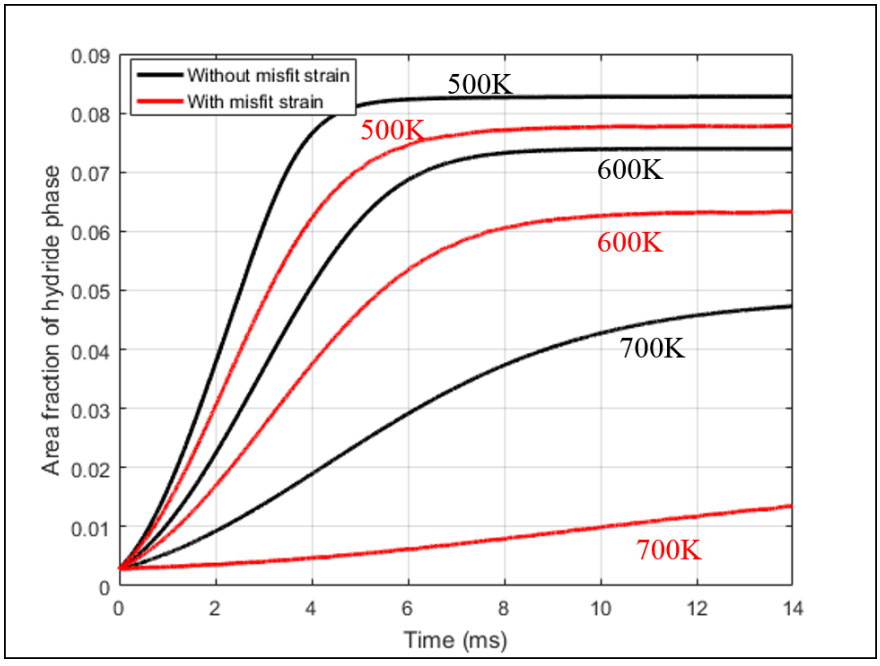

(b)

Figure 4.3: Evolution of the δ-hydride area fraction at different temperatures. (a) The system with $F_{\text{el}} = 0$. (b) Comparing between the $F_{\text{el}} = 0$ systems and the systems with $F_{\text{el}} =$ Eqn. (4.14).

to the data in Fig. 4.3a is shown in Fig. 4.4, which shows the maximum K value is at 485 K. Fig. 4.3b compares the evolution of the hydride particle area fraction between two cases when the $F_{\text{el}} = 0$ and when $F_{\text{el}} =$ Eqn. (4.14). The addition of the strain energy suppressed the growth rate of the hydride particle since extra energy was needed during the phase transformation to compensate the lattice misfit strain. The result suggests that the thermodynamic and kinetic modules of Hyrax agree with the classical theory, giving confidence to the modeling results.

Furthermore, all systems in Fig. 4.3 have the same ∼600 wppm hydrogen concentration, but the area fractions at the equilibrium state are different between the systems as shown the figure. This is because the equilibrium hydrogen concentration varies at different temperatures, which is determined by minimizing the total free energy of the system. The hydrogen

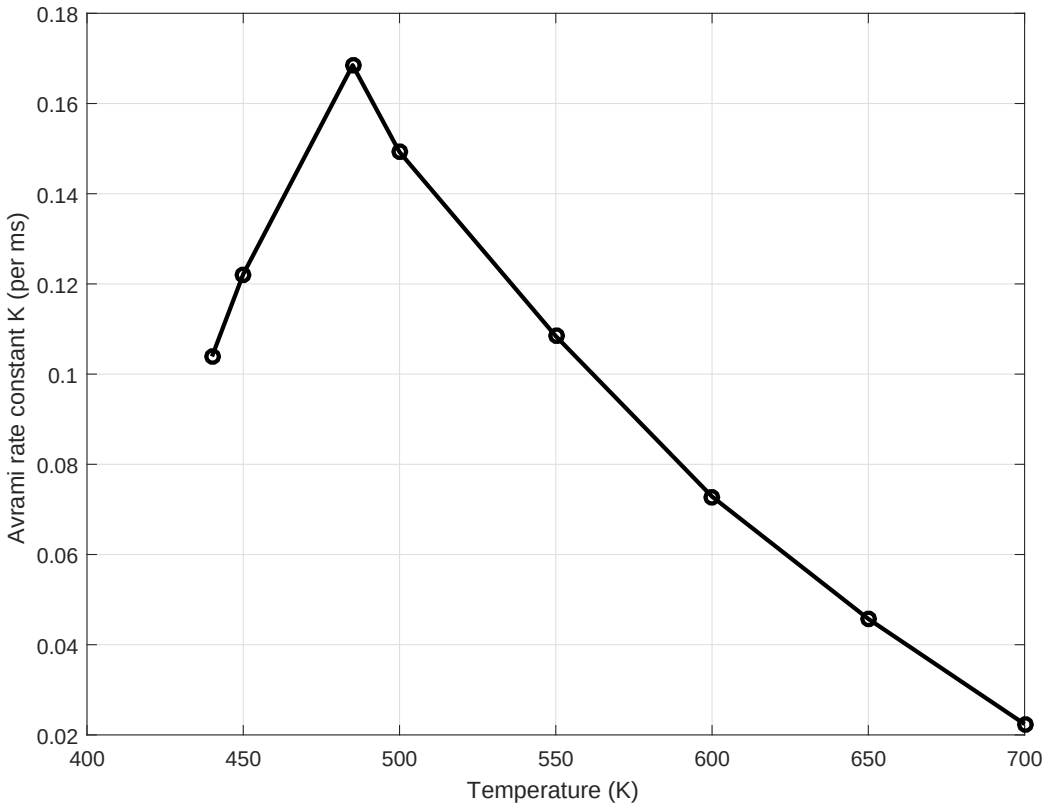

Figure 4.4: The Avrami rate constant K as a function of temperature fitted using the Eqn. (4.16) and data in Fig. 4.3a.

solvus in α-Zr solution can be modeled by extracting the equilibrium χ_{H} in the zirconium solution at each temperature. Since the hydride phase grows during the simulation, the hydrogen solvus for the system that includes F_{el} is regarded as the precipitation solvus (TSSp). For the system with $F_{\mathrm{el}} = 0$, the modeled solvus is between the dissolution (TSSd) and the precipitation solvus (TSSp) since no strain energy is involved. Fig. 4.5 shows the hydrogen solvus predicted by Hyrax. The result is compared with the experiment conducted by McMinn *et al.* [15] and Kearns [16], respectively. McMinn *et al.* measured the hydrogen TSSp in a Zircaloy-2 solution. Kearns's data utilized the diffusion-couple method for hydrogen in a zirconium solution; this data is often regarded as the strain energy free solvus (TSS) since no hydride dissolution or precipitation was involved. For both cases, the mod-

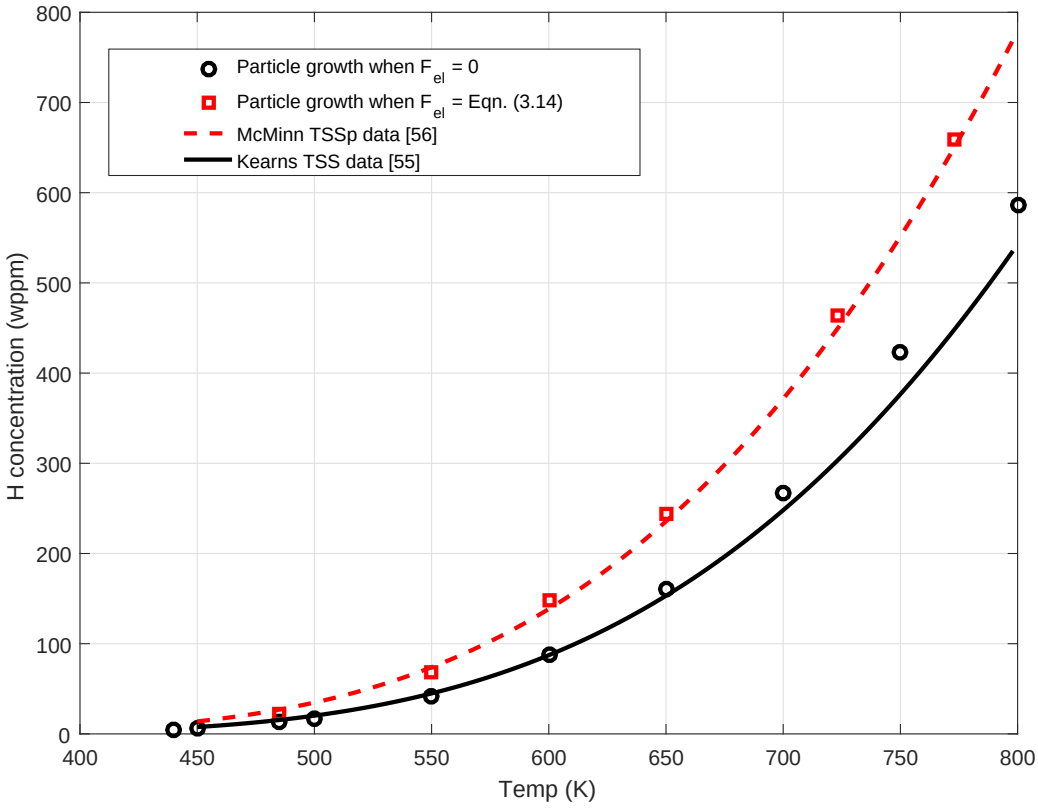

Figure 4.5: Hydrogen solvus in the zirconium solution. The red square and the black circle are solvus data calculated by Hyrax for the systems with $F_{\mathrm{el}} = 0$ and with $F_{\mathrm{el}} =$ Eqn. (4.14), respectively. The red-dashed and the black-solid line are solvus measured experimentally by Ref. [15] and Ref. [16], respectively.

eled solvus agree well with the experimental result. We regard the result as the validation of Hyrax output. The modeled hydrogen solvus are described using the Arrhenius-type equation,

For TSS,

$$C_{\mathrm{H}}^{\mathrm{TSS}}\ (\mathrm{wppm}) = 230960 \times \exp\Big(\frac{-39433 \pm 400}{RT}\Big) \tag{4.17}$$

For TSSp,

$$C_{\mathrm{H}}^{\mathrm{TSSp}}\ (\mathrm{wppm}) = 208981 \times \exp\Big(\frac{-37329 \pm 2260}{RT}\Big) \tag{4.18}$$

where R is the ideal gas constant the T is the temperature in K. Comparing the result listed in Table 3.3, the molded Q values agree with the stress-free Q_p, and are larger than the Q_p measured under applied stress. The hydrogen solvus under the effect of applied stress is modeled in the following sections.

4.2.2 Effect of an uniformly applied stress on a single Zr crystal system

A general formula to include the external stress contribution on the total strain energy is,

$$F_{\mathrm{el}} = \frac{1}{2}\int_V C_{ijkl}\epsilon_{ij}^{\mathrm{el}}(\mathbf{r})\epsilon_{kl}^{\mathrm{el}}(\mathbf{r})dV - V\epsilon_{ij}^{\mathrm{a}}\sigma_{ij}^{\mathrm{a}} \tag{4.19}$$

where ${\epsilon_{ij}}^{\mathrm{a}}$ is the strain induced by the applied stress at each point and σ_{ij}^{a} is the applied stress. An advantage of the FEA method is the external stress can be input as a boundary condition in a form of a displacement. The strain induced by the external stress is then calculated using Eqn. (4.11).

It is clear that the modeling system in Fig. 4.1 and 4.2 have two mirror symmetries. Therefore, the system size can be reduced to a quarter to reduce the computing resources while keeping the correct physics information. Fig. 4.6 shows an example of a quarter system at equilibrium at 600 K. Also shown in the figure is the crystalline orientation of the system. The external stress direction is varied by applying the displacement at different boundaries. The simulation process is the same as the last section; a hydride seed is placed in the middle of the supersaturated Zr matrix with the external stress applied at the boundary. The χ_H

value in the Zr solution is output when the system reaches the equilibrium.

The change of equilibrium hydrogen concentration in the zirconium solid solution as a function of externally applied tensile stress is shown in Figure 4.7. The modeling result suggests that the tensile stress has a negligible effect on the hydrogen solvus. In Fig. 4.7a, the tensile stress slightly decreases the amount of hydrogen in the solution. Increasing stress from 0 to 250 MPa decreases the hydrogen concentration in the solution by less than 1 wppm. This observation agrees well with Puls theory of the hydrogen solvus concentration under stress [54, 63]. Puls estimated that under a uniform 1800 MPa stress, the energy term Q is only decreased by 129 $\mathrm{J\,mol^{-1}H}$, corresponding to increase of $\sim$ 3 wppm hydrogen in the solution at 600 K. However, this does not agree with the experimental observation discussed in Chapter 3.

One hypothesis is the stress effect could significantly depend on the crystalline orientation. For the next modeling, the stress was applied along the different lattice directions at different temperatures. The TSSp hydrogen solvus was again described by the Arrhenius equation using the equilibrium hydrogen concentration at each temperature. The simulated hydrogen solvus are shown in Fig. 4.8. In Fig. 4.8a, the stress effect is insignificant and the three hydrogen solvus overlapped. Fig. 4.8b shows a part of Fig. 4.8a that was enlarged to show the difference. Since the c-axis is stiffer, the effect of the stress when applied along the a-axis is twice as large as when the stress is applied along the c-axis, but the stress effect is negligible in both cases. Linear regression analysis based on the Arrhenius type equation for all of the data points in Fig. 4.8a is summarized in Table 4.1. In Table 4.1, three Q_p are equal within the uncertainty.

The modeling result in this section suggests that regardless of the loading direction, uniform applied stress has no effect on the hydrogen precipitation behavior in a single zirconium

Table 4.1: The Q_p values of simulated hydrogen solvus.

Conditions	Q_p (J/mol)
$\sigma = 0$	36652±2261
$\sigma = 100$ MPa $\parallel$ a-axis	36998±1122
$\sigma = 100$ MPa $\parallel$ c-axis	37037±1097

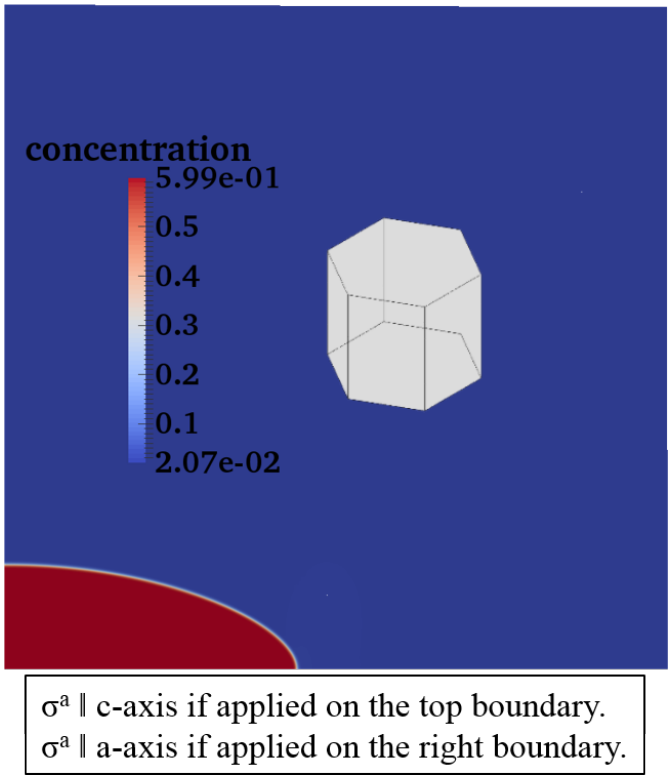

Figure 4.6: The equilibrium system at 600 K with a quarter of hydride particle.

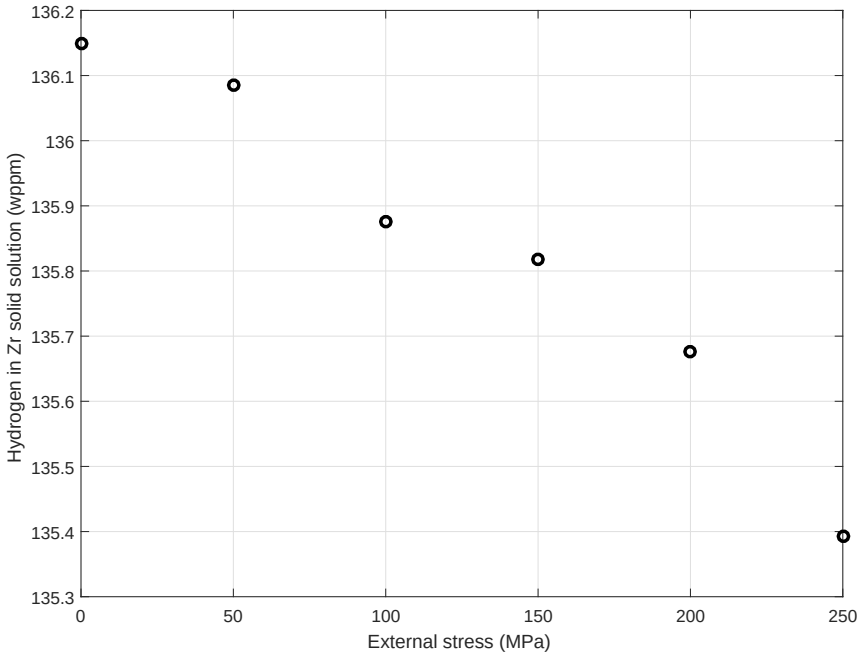

Figure 4.7: Effect of the external tensile stress on the hydrogen amount in the zirconium solid solution at 600 K. The stress was applied along the a-axis of a zirconium lattice.

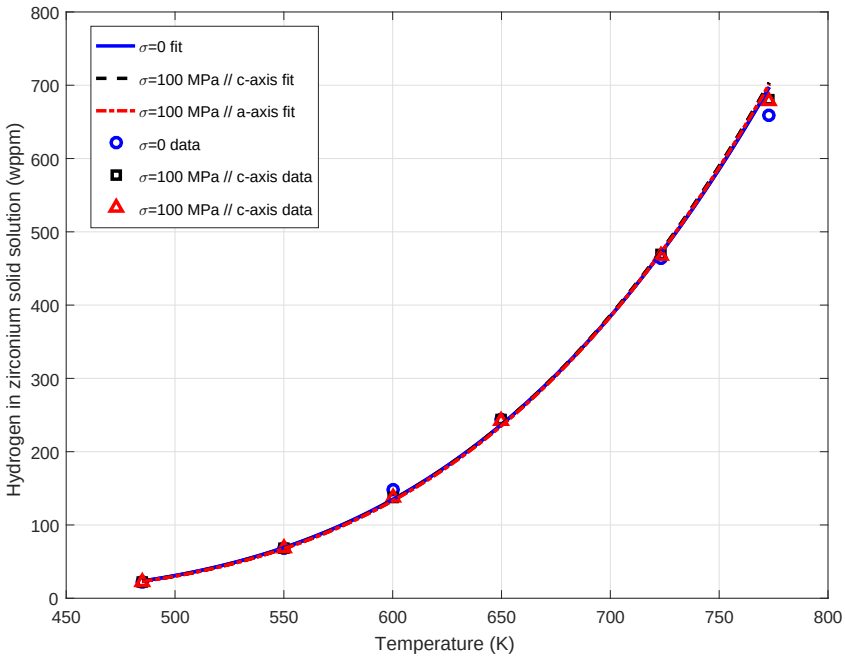

(a)

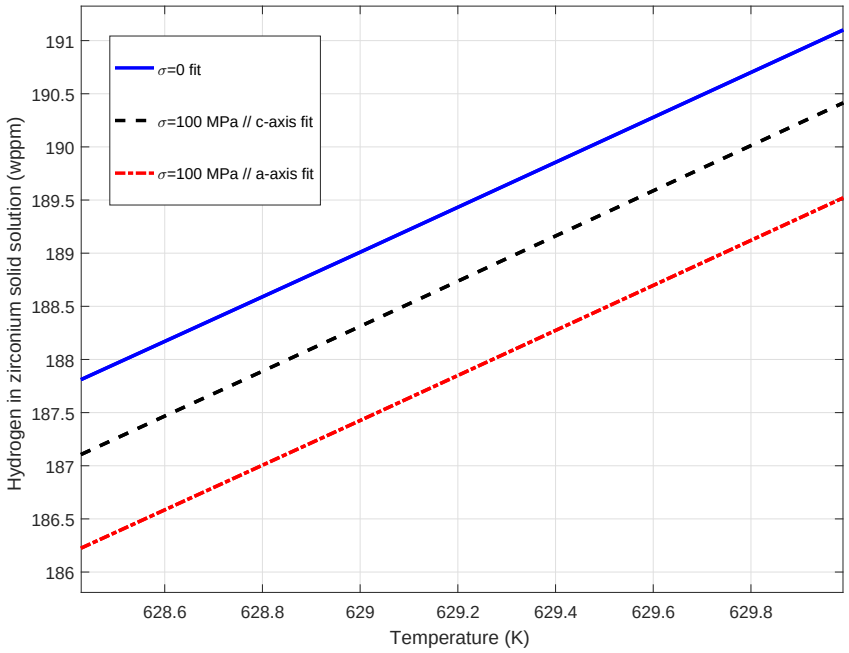

(b)

Figure 4.8: (a) Hydrogen TSSp solvus simulated by Hyrax under different stress conditions. (b) Same as the (a) but only shows a narrow temperature and the hydrogen concentration range.

crystal. Again, this agrees well with Puls's theory but does not explain the experimental observation by Colas *et al.* [28], Vizcaíno *et al.* [59] and this work. Since both the Puls's theory and Hyrax modeling described in this section focused on a single zirconium crystal system and all experiments performed on polycrystal samples, it is reasonable to postulate that the disagreement might be due to the different behavior between a single and a poly-crystal system. Therefore, we simulated the stress effect on a bi-crystals zirconium system. This is discussed in the next section.

4.2.3 Effect of an uniformly applied stress on a bi-crystal system

The bi-crystal system with two zirconium crystals is shown in Fig. 4.9a. Zirconium lattices with different crystalline orientations are depicted in the figure. The 0° grain has the c-axis parallel to the x-axis (the horizontal direction) while the 90° grain has the c-axis parallel to the y-axis (the vertical direction). The grain boundary is ignored and hydrogen is free to diffuse between the two crystals. Since the diffusion coefficient is assumed isotropic, the crystalline orientation is defined by the compliance tensor arrangement. The simulation process is the same as the last section. A hydride seed is placed in the middle of each zirconium crystal, surrounding by the super-saturated zirconium solution. A 100 MPa uniform tensile stress is applied along the x-axis of the system. Fig. 4.9b shows the bi-crystals system after reach the equilibrium. It is clear in Fig. 4.9b that the hydride particle in the 0° crystal becomes larger than the particle in the 90° crystal. Since the hydrogen concentration in the system is conserved, this result indicates that hydrogen diffuses to the 0° crystal from the 90° crystal. In other words, hydrogen diffuses toward the crystal which has the c-axis parallel to the load direction, precipitating more hydride phase in that crystal. This is the same observation as by the diffraction experiment (see Table 3.3). The result of the first bi-crystals modeling is encouraging. A series of systematic modeling for the bi-crystal system was performed. The data interpretation is given in the following paragraphs.

Similarly to the quarter-particle treatment in the Section 3.2.2, the computational efficiency can be increased by reducing the modeling system size by half. In order to confirm that the behavior observed in Fig. 4.3 was solely caused by the external stress, modeling for

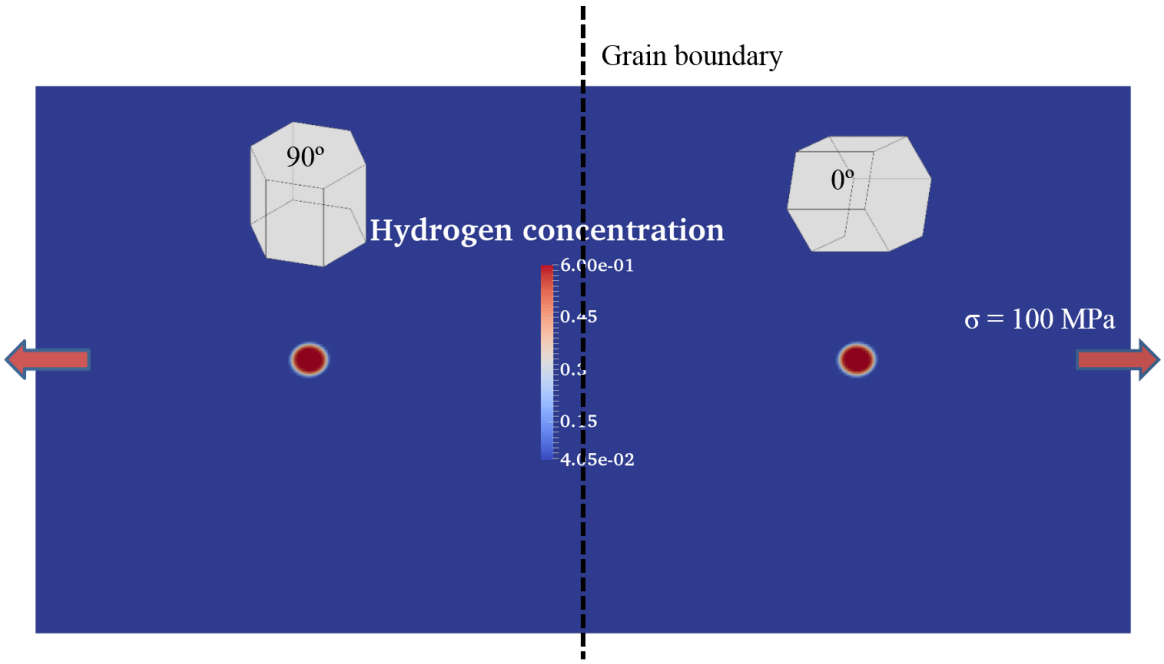

(a)

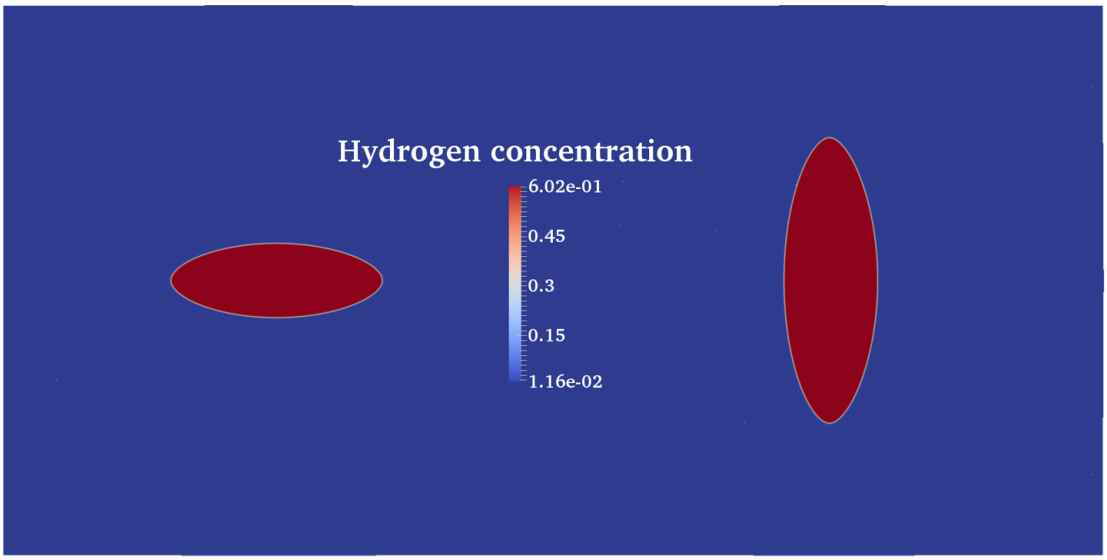

(b)

Figure 4.9: Evolution of hydride particles in a bi-crystal system under a 100 MPa applied stress. The left and the right zirconium grain has the a and the c-axis parallel to the stress direction, respectively. The grain boundary indicates the boundary for different stiffness tensor arrangement, but does not contribute extra energy to the system. (a) The system at $t = 0$ and (b) the system at $t = t_{\text{eq}}$

several bi-crystal systems with different crystal arrangements were performed. The orientations and results are shown in Fig. 4.10. It was observed that when the external stress is absence, the hydride particle in each zirconium grain grew at the same rate. The size of the hydride particle at equilibrium is the same between each zirconium grain, independent of the crystalline orientation. This is as expected. Furthermore, the applied stress does not affect the system which has grains with the same orientation but only affects the system composed of a 0° and a 90° grain. In the last system of Fig. 4.10, the hydrogen diffuses from the 90° grain toward the 0° grain, precipitating more hydride in the 0° grain as also observed in Fig. 4.3. The result confirms that the hydrogen redistribution only occurs between crystals with different crystalline orientations when an external stress is present.

We can calculate the difference of equilibrium hydride area fraction ΔA_f^δ between the system with and without the external stress at different temperatures T using,

$$\Delta A_f^\delta(T) = A_{f,\sigma}^\delta(T) - A_{f,\sigma=0}^\delta(T) \tag{4.20}$$

where $A_{f,\sigma}^\delta$ and $A_{f,\sigma=0}$ are equilibrium δ-hydride area fraction with and without the applied stress, respectively. ΔA_f^δ represents the extra amount of hydrogen diffuses to the 0° crystal to form additional hydride phase induced by the external stress. $\Delta A_f^\delta(T)$ can be converted to $\Delta \mathrm{H}_{\mathrm{wppm}}^\sigma(T)$, the additional amount of hydrogen in the solid solution. Fig. 4.11 shows the three hydrogen TSSp solvus by 1): the synchrotron diffraction in the Section 3.2.3, 2): Hyrax modeling for a single crystal system with $\sigma = 0$ in the Section 4.2.1, and 3): Hyrax modeling for a bi-crystal system with $\sigma = 105$ MPa in this section. Although using a simplified bi-crystals model, the simulated TSSp is close to the experimental measurement, except at 485 K. This result supports the conclusion stated in Section 3.3 that the external stress does not affect the hydrogen solubility in zirconium but re-distributes the hydrogen among zirconium crystals based on the crystalline orientation. The hydrogen tends to diffuse toward to grains with higher tensile stress along the c-axis, precipitating more hydride phase in the grains.

The grain boundary is not included in this bi-crystal system. Adding a grain boundary could affect the system by: 1) providing a high-diffusivity path along the boundary and 2) providing heterogeneous nucleation sites for the zirconium hydride. It is known for metal

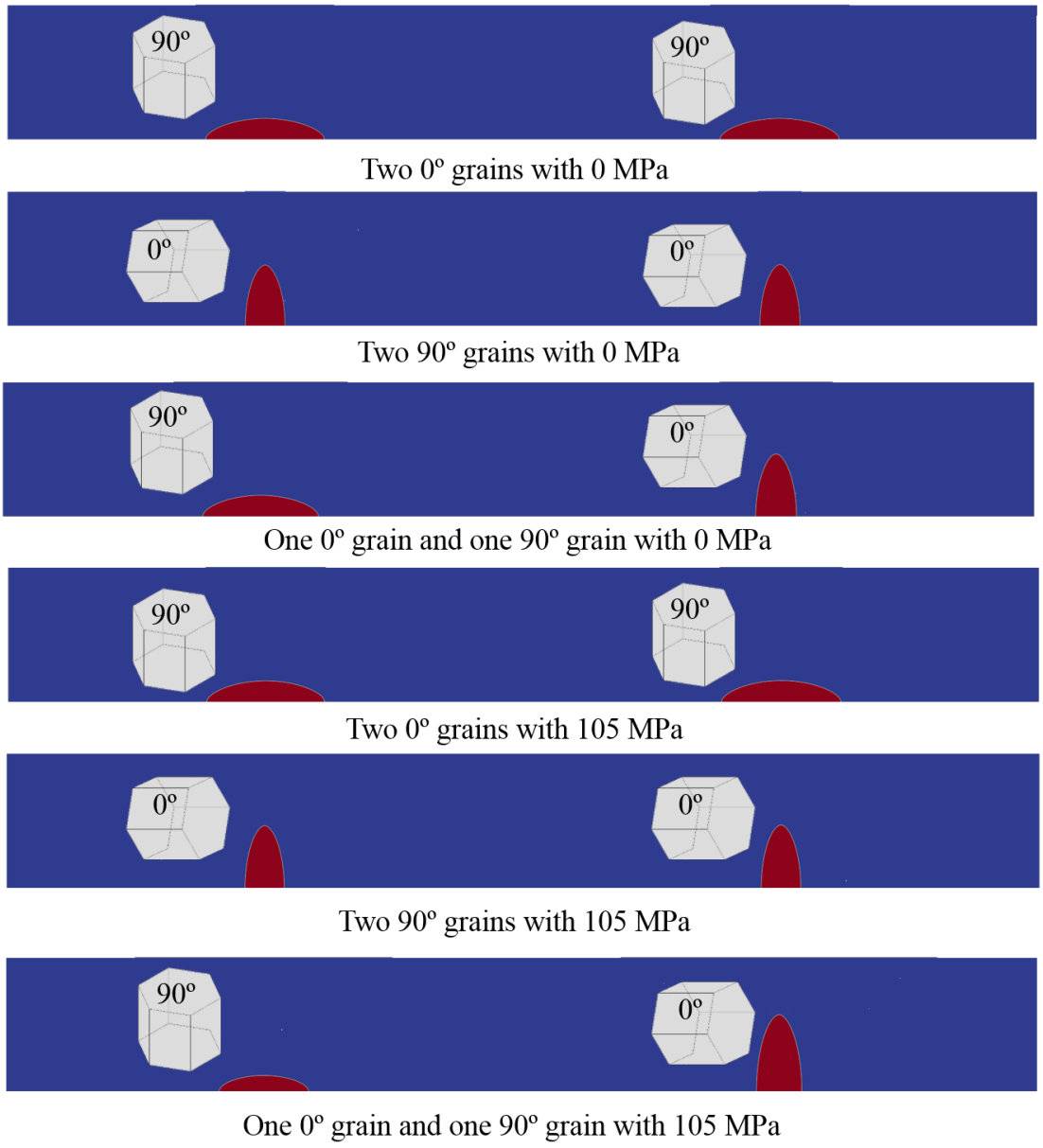

Figure 4.10: Hydride particles distribution among grains in bi-crystal systems with different orientation arrangements. Systems were at 600 K and ran to equilibrium.

alloys that the grain boundary diffusion becomes dominant at low temperatures (below 0.75-0.8 melting temperature) [104]. Therefore, we can expect the grain boundary diffusion is much greater than the diffusion within the zirconium lattice for the temperature range encountered in this study. However, the boundary diffusion should only affect the kinetic process not equilibrium state.

Unlike the grain boundary diffusion, not including nucleation of the intergranular hydride (hydride nucleation on the grain boundary) could yield uncertainty to the modeling result. Bailey [17] observed the preferential nucleation of intergranular hydride in a zirconium specimen using a TEM image (shown in Fig. 4.12a). Ma *et al.* [84] also incorporated the grain

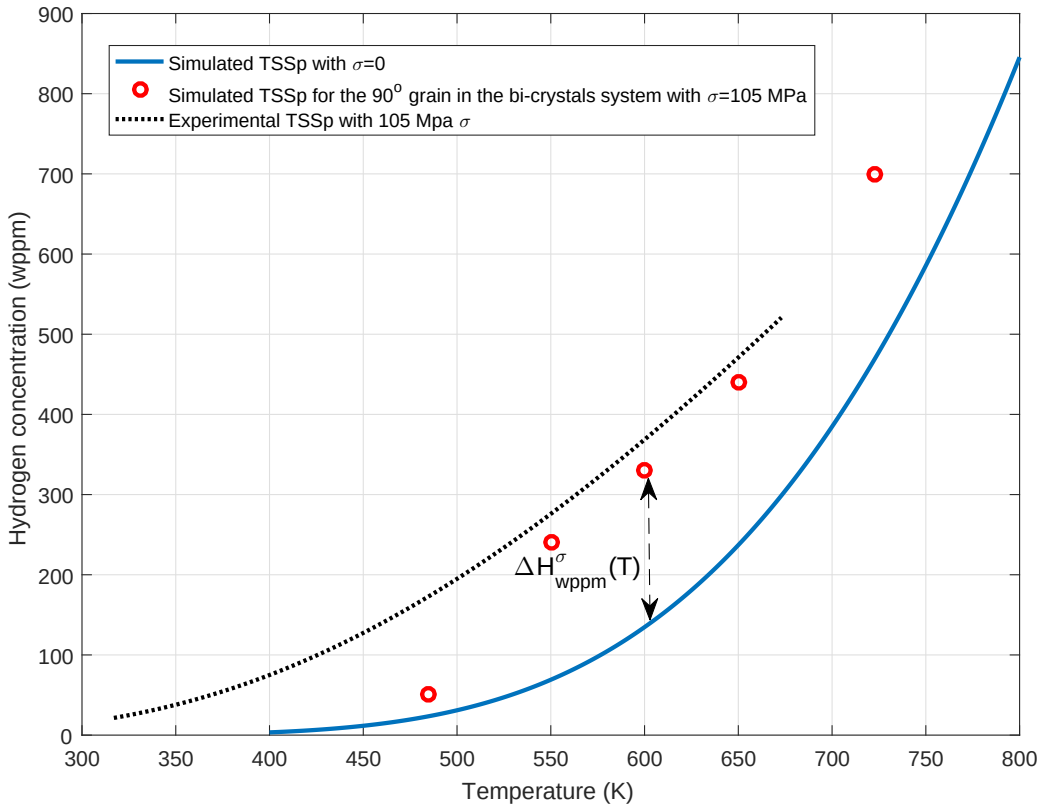

Figure 4.11: Hydrogen TSSp solvus measured by synchrotron diffraction and Hyrax simulation. The black-dash line is the experimental result listed in Table 3.3. The blue-solid line is the solvus simulated by Hyrax for a single crystal system without the external stress, while the red circle is the solvus simulated by Hyrax for the 90° grain in the bi-crystals system with $\sigma = 105$ MPa.

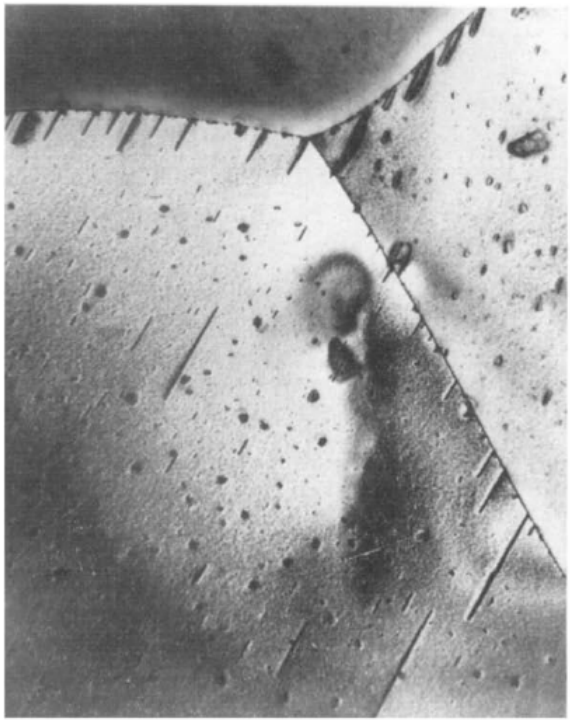

(a) The preferential nucleation of intergranular hydride.

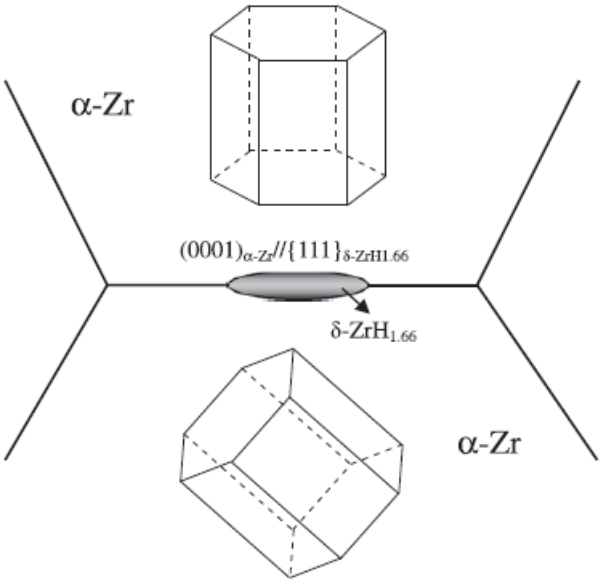

(b)

Figure 4.12: (a) A TEM image shows the preferential nucleation of hydride on the zirconium grain boundary. This figure was reprinted from Fig. 2(c) in Ref. [17]. (b) The preferred grain orientations for intergranular δ hydride. This figure was reprinted from Fig. 6(a) in Ref. [18].

boundary energy in their phase-field simulation for a bi-crystalline zirconium system. In their work, the free energy of the system was artificially decreased when a hydride particle nucleated on the grain boundary. It is clear that their result is only qualitatively valid. A theoretical discussion by Qin *et al.* [18] provided more understanding for intergranular hydride in a zirconium matrix. Their calculation indicated the intergranular hydride was most likely to form at the boundary where only one of the two adjacent Zr crystals had the basal plane parallel to the boundary, as schematically shown in Fig. 4.12b. Notice that Fig. 4.12b is very similar to the bi-crystalline system simulated in this work (see Fig. 4.9). This implies that our bi-crystalline system maybe too simplified and could lead to an erroneous result. However, these authors also pointed out the formation of intergranular hydrides was affected by many factors and had larger uncertainty than the formation of the intragranular hydrides. For example, the intergranular hydride is less frequently in the CWSR than the recrystallized Zircaloy due to the average lower grain boundary energy in the CWSR sample.

To summarize, not including the grain boundary could affect the equilibrium status of the bi-crystalline system due to formation of the intergranular hydrides. Adding the nucleation algorithm should be considered in the future work. The diffusion along the grain boundary should not affect the equilibrium status but will affect the modeling kinetic.

It is interesting to understand why hydrogen redistribution among grains occurred. We examined the elastic strain energy term F_{el} since it was the only variable affected by the stress at $t = 0$. Fig. 4.13 shows the F_{el} distribution at $t = 0$ for several bi-crystals systems with 105 MPa applied stress. The energy value within the Zr matrix, as well as the contour generated by the strain field around the hydride seed, can be observed. For the system which has two 0° or 90° crystals, the F_{el} value is the same within two matrix solution. However, for the system which has one 0° and one 90° crystal, the F_{el} value is lower within the 0° crystal, generating a strain energy gradient across the system. At $t = 0$, this strain energy gradient is solely raised by the external stress. The 0° crystal becomes a preferential site to contain more interstitial hydrogen and form greater hydride phase area fraction, generating more lattice misfit strain to compensate the strain energy gradient. The diffusion of hydrogen from the 90° crystal to the 0° crystal also balances the strain energy value between two crystals, decreasing the chemical potential gradient of the system. This also explains why

hydrogen re-distribution does not occur without the external stress since the strain energy gradient is lacking. However, the equilibrium hydrogen concentration in the solution only slightly varied. Table 4.2 summarized the equilibrium χ_{H} value in the α-Zr solution under various conditions. This observation indicates that the external stress does not affect the hydrogen solubility, but redistributes the precipitated hydride phase among Zr crystals. The

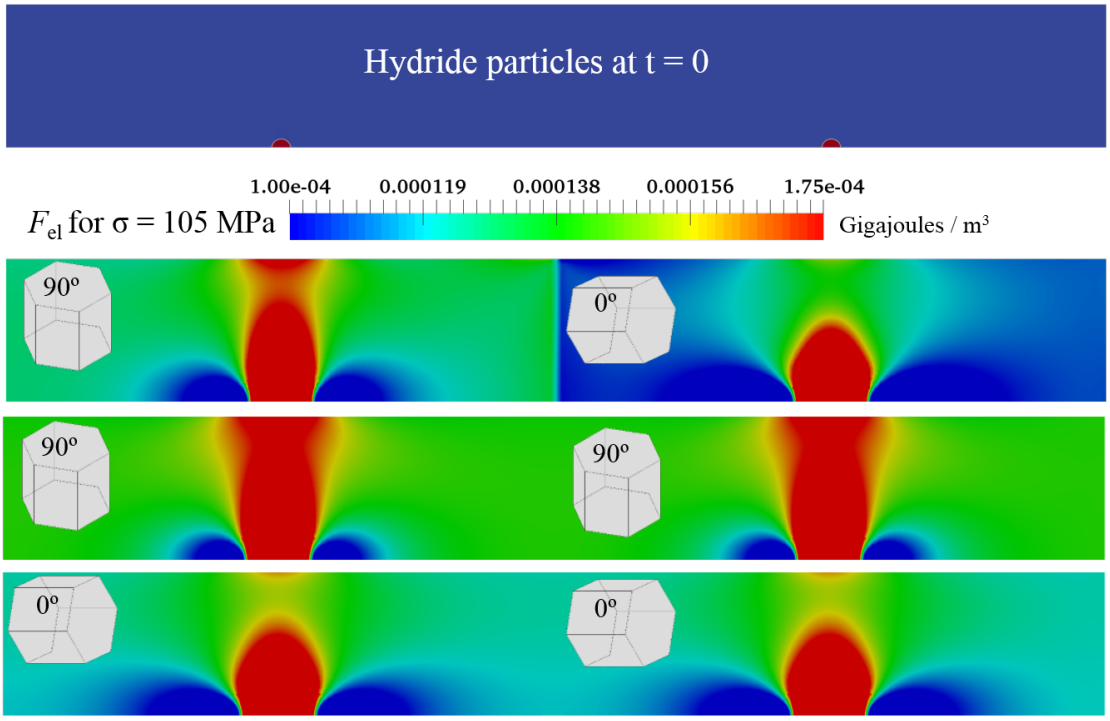

Figure 4.13: Distribution of F_{el} in several bi-crystals systems with different orientation arrangements. Systems were at $t = 0$, 600 K with 105 MPa stress applied along the x-axis. The top image shows the two hydride seeds at $t = 0$.

Table 4.2: Summary of equilibrium $\chi_{\mathrm{H}}^{\alpha}$ at 600 K under various conditions.

	Single crystal			Bi-crystals	
	0	100 MPa || a-axis	100 MPa || c-axis	0	100 MPa
$\chi_{\mathrm{H}}^{\alpha}$	1.24×10^{-2}	1.24×10^{-2}	1.23×10^{-2}	1.24×10^{-2}	1.24×10^{-2}

stress facilitates hydride accumulation in crystals which have higher tensile stress on their c-axis.

Several published results support our observation. Vizcaíno *et al.* [59] studied effect of crystalline orientation on the external stress applied to a Zr-2.5Nb alloy. Using synchrotron diffraction technique, these authors observed an appearance of δ-phase reflection when subjected to an external load among Zr crystals with their c-axis parallel to the loading direction. This means when the load was applied, hydrogen re-distributed among grains followed by preferential precipitation of hydride in those Zr grains. Une *et al.* [105] studied the effect of tensile load on a Zry-2 cladding tube using electron backscatter diffraction technique. They observed that hydride preferentially precipitated in grains whose basal plane normal (c-axis) was closely inclined toward to the load direction. The result of our study provides the explanation for these observations.

We demonstrate that beside studying the morphology evolution of particles, phase-field modeling is also applicable for quantitative study. The technical gap, as described in Section 2.3, between the Pul's theory and the experimental observation was resolved after applied in the phase-field simulation. The finding of this research is summarized in the next chapter.

CHAPTER 5

CONCLUSION

We have utilized in situ diffraction technique and the phase-field simulation to study the effect of stress on hydrogen solvus in zirconium alloy solution. One of the primary goals is to resolve the disagreement between the current theory prediction and the experimental observation. The important finding throughout this research and the comprehensive explanation for the disagreement between the theory and the experiment are stated below:

I. For the overall hydrogen/deuterium concentration experimentally studied in this research, the f.c.c δ-hydride is the only hydride/deuteride phase present in the specimens; this is true for both the hydride blister and other regions. This suggests that δ-hydride is the most stable zirconium-hydride phase when precipitating under a slow cooling rate ($1\ ^{\circ}\mathrm{C\,min^{-1}}$) regardless the formation of the hydride rim or blister region or not.

II. According to our experiment, the applied stress only affects the hydride when associated with dissolution or precipitation behavior. The δ-hydride is fairly stable under an isothermal condition if the applied stress is below the yield strength of the zirconium matrix. The external stress effect depends on the studied Zr crystalline orientation; the tensile stress increases the hydrogen solubility in Zr grains with their basal plane normal (c-axis) inclined toward the stress direction, decreasing the energy term Q if using the Arrhenius type equation to describe the hydrogen solvus (see Table 3.3). This effect increased with increasing tensile stress magnitude along the c-axis of the Zr grains. This observation is consistent with previous experimental results, but in disagreement with the theoretical estimation which stats that the effect of external stress on hydrogen solubility is negligible.

III. The CALPHAD-based phase-field modeling code Hyrax was applied to quantitatively

simulate the hydrogen solubility in a zirconium matrix. The model was first validated by comparing with the previous stress-free experimental data (see Fig. 4.5). The result is in good agreement with experimental data and is considered the first validation of Hyrax output. The simulation for a single crystal system (containing only one zirconium grain) suggests that the external stress does not affect the hydrogen solubility regardless the stress value and direction (see Fig. 4.8 and Table 4.1). This result is consistent with the theoretical estimation but in disagreement with the experimental observation.

IV. Phase-field modeling for a bi-crystal system shows that under applied stress, hydrogen diffuses toward to the preferable crystal, precipitating a larger hydride particle in that crystal. This only occurs when the two crystals have different orientation and when the external stress is present (see Fig. 4.10). For the bi-crystal system that we studied, the preferable crystal oriented with the c-axis parallel to the stress direction (0° grain in Fig. 4.10). We calculated the extra amount of hydrogen transported by the external stress to the preferable crystal and compared with our synchrotron experiment result (see Fig. 4.11); the two results are in reasonable agreement. This suggests that the external stress re-distributes the hydride among zirconium crystals. The redistriubtion is caused by the strain energy gradient induced by the external stress (see Fig. 4.13). The grain with a lower strain energy is preferable for occupying more hydrogen and growing larger hydride particle.

An important conclusion is the stress does not affect the hydrogen solvus in a zirconium-hydrogen system, as also predicted by the Puls theory. Stress redistributes hydrogen and the hydride phase among zirconium grains of a system. When a stressed system reaches equilibrium, crystals with the preferable orientation contain greater amount of the hydride phase. Although the experiment performed in this research and other previous works [28, 59, 105] support this conclusion, several limitations exist. One significant uncertainty exists in Eqn. (4.20) and Fig. 4.11, where we converted the extra hydride fraction into the extra hydrogen in the solid solution for the modeled bi-crystal system. This is because what we observed extra hydrogen in the solid solution raised by the external stress during the

synchrotron experiment; the stress actually decreased the hydride fraction, causing more hydrogen in the solid solution. This is opposite to the modeling result. It could be during the experiment the system never reached the equilibrium or when the hydride phase re-distributed by the stress, its texture changed and could not be detected using the same plane reflection. These facts should be considered if going to apply this conclusion. Other issues include 1): nucleation algorithms was not implemented, 2): plastic deformation around the hydride particle was not included and 3): the grain boundary was not considered. These along with other minor issue such as not including possible defects in Zr crystals could change the equilibrium hydrogen and hydride distribution. Nevertheless, this study did resolve the disagreement between the theoretical estimation and experimental observation. The effect of external stress on hydride distribution in a Zr-H system is significant, and should not be ignored when evaluating or predicting the fuel cladding performance.

REFERENCES

[1] *ASTM B811-13e1 Standard Specification for Wrought Zirconium Alloy Seamless Tubes for Nuclear Reactor Fuel Cladding*, ASTM International, West Conshohocken, PA Std., 2013. [Online]. Available: www.astm.org

[2] A. M. Garde, S. R. Pati, M. A. Krammen, G. P. Smith, and R. K. Endter, "Corrosion behavior of zircaloy-4 cladding with varying tin content in high-temperature pressurized water reactors," in *Zirconium in the Nuclear Industry: Tenth International Symposium*. ASTM International, 1994.

[3] S. Kass, "The development of the zircaloys," in *Corrosion of Zirconium Alloys*. ASTM International, 1964.

[4] C. Lemaignan and A. T. Motta, "Zirconium alloys in nuclear applications," *Materials Science and Technology*, 1994.

[5] E. Zuzek, J. Abriata, A. San-Martin, and F. Manchester, "The h-zr (hydrogen-zirconium) system," *Journal of Phase Equilibria*, vol. 11, no. 4, pp. 385–395, 1990.

[6] C. Domain, R. Besson, and A. Legris, "Atomic-scale ab-initio study of the zr-h system: I. bulk properties," *Acta materialia*, vol. 50, no. 13, pp. 3513–3526, 2002.

[7] S. MacEwen, C. Coleman, C. Ells, and J. Faber, "Dilation of hcp zirconium by interstitial deuterium," *Acta Metallurgica*, vol. 33, no. 5, pp. 753–757, 1985.

[8] S. Yamanaka, D. Setoyama, H. Muta, M. Uno, M. Kuroda, K. Takeda, and T. Matsuda, "Characteristics of zirconium hydrogen solid solution," *Journal of Alloys and Compounds*, vol. 372, no. 1, pp. 129–135, 2004.

[9] P. Olsson, A. Massih, J. Blomqvist, A.-M. A. Holston, and C. Bjerkén, "Ab initio thermodynamics of zirconium hydrides and deuterides," *Computational Materials Science*, vol. 86, pp. 211–222, 2014.

[10] M. N. Cinbiz, D. A. Koss, A. T. Motta, J.-S. Park, and J. D. Almer, "In situ synchrotron x-ray diffraction study of hydrides in zircaloy-4 during thermomechanical cycling," *Journal of Nuclear Materials*, vol. 487, pp. 247–259, 2017.

[11] T. B. Flanagan, N. Mason, and H. Birnbaum, "The effect of stress on hydride precipitation," *Scripta Metallurgica*, vol. 15, no. 1, pp. 109–112, 1981.

[12] J.-l. Lin, X. Han, B. J. Heuser, and J. D. Almer, "Study of the mechanical behavior of the hydride blister/rim structure in zircaloy-4 using in-situ synchrotron x-ray diffraction," *Journal of Nuclear Materials*, vol. 471, pp. 299–307, 2016.

[13] J.-l. Lin, K. An, A. D. Stoica, and B. J. Heuser, "Effect of external stress on deuteride (hydride) precipitation in zircaloy-4 using in situ neutron diffraction," *Journal of Nuclear Materials*, vol. 487, pp. 396–405, 2017.

[14] J.-L. Lin, "Investigation of the mechanical behavior of rim/blister structure hydride phases in zircaloy-4 by utilizing high energy synchrotron x-ray diffraction," Ph.D. dissertation, 2015.

[15] A. McMinn, E. C. Darby, and J. S. Schofield, "The terminal solid solubility of hydrogen in zirconium alloys," in *Zirconium in the Nuclear Industry: Twelfth International Symposium*. ASTM International, 2000.

[16] J. Kearns, "Terminal solubility and partitioning of hydrogen in the alpha phase of zirconium, zircaloy-2 and zircaloy-4," *Journal of nuclear materials*, vol. 22, no. 3, pp. 292–303, 1967.

[17] J. Bailey, "Electron microscope observations on the precipitation of zirconium hydride in zirconium," *Acta metallurgica*, vol. 11, no. 4, pp. 267–280, 1963.

[18] W. Qin, N. K. Kumar, J. Szpunar, and J. Kozinski, "Intergranular δ-hydride nucleation and orientation in zirconium alloys," *Acta Materialia*, vol. 59, no. 18, pp. 7010–7021, 2011.

[19] H. G. Rickover, L. D. Geiger, and B. Lustman, "History of the development of zirconium alloys for use in nuclear reactors," Energy Research and Development Administration, Tech. Rep., 1975.

[20] J. Abriata, J. Bolcich, and D. Arias, "The sn- zn (tin-zirconium) system," *Bulletin of Alloy Phase Diagrams*, vol. 4, no. 2, pp. 147–154, 1983.

[21] D. Charquet, R. Hahn, E. Ortlieb, J.-P. Gros, and J.-F. Wadier, "Solubility limits and formation of intermetallic precipitates in zrsnfecr alloys," in *Zirconium in the Nuclear Industry: Eighth International Symposium*. ASTM International, 1989.

[22] B. Cox, "Some thoughts on the mechanisms of in-reactor corrosion of zirconium alloys," *Journal of Nuclear materials*, vol. 336, no. 2, pp. 331–368, 2005.

[23] F. Garzarolli, R. Schumann, and E. Steinberg, "Corrosion optimized zircaloy for boiling water reactor (bwr) fuel elements," in *Zirconium in the Nuclear Industry: Tenth International Symposium*. ASTM International, 1994.

[24] V. Garat, D. Deuble, B. Dunn, and J. Mardon, "Quantification of the margins provided by m5® cladding in accidental conditions," in *Proceedings of the 2012 LWR Fuel Performance Meeting, Manchester, UK, September 2–6*, 2012.

[25] E. Fisher and C. Renken, "Single-crystal elastic moduli and the hcp to bcc transformation in ti, zr, and h," *Physical Review*, vol. 135, no. 2A, p. A482, 1964.

[26] J. Kearns, "Thermal expansion and preferred orientation in zircaloy (lwbr development program)," Bettis Atomic Power Lab., Pittsburgh, PA (USA), Tech. Rep., 1965.

[27] A. Anderson, R. Thompson, and C. Cook, "Ultrasonic measurement of the kearns texture factors in zircaloy, zirconium, and titanium," *Metallurgical and Materials Transactions A*, vol. 30, no. 8, pp. 1981–1988, 1999.

[28] K. B. Colas, A. T. Motta, M. R. Daymond, and J. D. Almer, "Effect of thermomechanical cycling on zirconium hydride reorientation studied in situ with synchrotron x-ray diffraction," *Journal of Nuclear Materials*, vol. 440, no. 1, pp. 586–595, 2013.

[29] P. Tempest, "Preferred orientation and its effect on bulk physical properties of hexagonal polycrystalline materials," *Journal of Nuclear Materials*, vol. 92, no. 2-3, pp. 191–200, 1980.

[30] A. Garde, G. Smith, and R. Pirek, "In-pwr irradiation performance of dilute tin-zirconium advanced alloys," *ASTM SPECIAL TECHNICAL PUBLICATION*, vol. 1423, pp. 490–504, 2002.

[31] J.-C. Brachet, V. Vandenberghe-Maillot, L. Portier, D. Gilbon, A. Lesbros, N. Waeckel, and J.-P. Mardon, "Hydrogen content, preoxidation, and cooling scenario effects on post-quench microstructure and mechanical properties of zircaloy-4 and m5® alloys in loca conditions," *Journal of ASTM International*, vol. 5, no. 5, pp. 1–28, 2008.

[32] P. Narang, G. Paul, and K. Taylor, "Location of hydrogen in α-zirconium," *Journal of the Less Common Metals*, vol. 56, no. 1, pp. 125–128, 1977.

[33] R. Khoda-Bakhsh and D. Ross, "Determination of the hydrogen site occupation in the α phase of zirconium hydride and in the α and β phases of titanium hydride by inelastic neutron scattering," *Journal of Physics F: Metal Physics*, vol. 12, no. 1, p. 15, 1982.

[34] P. Burr, S. Murphy, S. Lumley, M. Wenman, and R. Grimes, "Hydrogen accommodation in zr second phase particles: Implications for h pick-up and hydriding of zircaloy-2 and zircaloy-4," *Corrosion Science*, vol. 69, pp. 1–4, 2013.

[35] M. Christensen, W. Wolf, C. Freeman, E. Wimmer, R. Adamson, L. Hallstadius, P. Cantonwine, and E. Mader, "H in α-zr and in zirconium hydrides: solubility, effect on dimensional changes, and the role of defects," *Journal of Physics: Condensed Matter*, vol. 27, no. 2, p. 025402, 2014.

[36] B. Baranowski, S. Majchrzak, and T. Flanagan, "The volume increase of fcc metals and alloys due to interstitial hydrogen over a wide range of hydrogen contents," *Journal of Physics F: Metal Physics*, vol. 1, no. 3, p. 258, 1971.

[37] H. Peisl, "Lattice strains due to hydrogen in metals," *Hydrogen in metals I*, pp. 53–74, 1978.

[38] E. Hong, D. C. Dunand, and H. Choe, "Hydrogen-induced transformation superplasticity in zirconium," *International journal of hydrogen energy*, vol. 35, no. 11, pp. 5708–5713, 2010.

[39] R. Beck, "Zirconium-hydrogen phase system," *Am. Soc. Metals, Trans. Quart.*, vol. 55, 1962.

[40] K. Barraclough and C. Beevers, "Some observations on the phase transformations in zirconium hydrides," *Journal of Nuclear Materials*, vol. 34, no. 2, pp. 125–134, 1970.

[41] Z. Zhao, J.-P. MORNIROLI, A. Legris, A. Ambard, Y. Khin, L. Legras, and M. BLATYRIEIX, "Identification and characterization of a new zirconium hydride," *Journal of microscopy*, vol. 232, no. 3, pp. 410–421, 2008.

[42] G. Carpenter, "The precipitation of γ-zirconium hydride in zirconium," *Acta Metallurgica*, vol. 26, no. 8, pp. 1225–1235, 1978.

[43] S. Mishra, K. Sivaramakrihnan, and M. Asundi, "Formation of the gamma phase by a peritectoid reaction in the zirconium-hydrogen system," *Journal of Nuclear Materials*, vol. 45, no. 3, pp. 235–244, 1972.

[44] J. Bair, M. A. Zaeem, and D. Schwen, "Formation path of δ hydrides in zirconium by multiphase field modeling," *Acta Materialia*, vol. 123, pp. 235–244, 2017.

[45] M. Puls, S.-Q. Shi, and J. Rabier, "Experimental studies of mechanical properties of solid zirconium hydrides," *Journal of Nuclear Materials*, vol. 336, no. 1, pp. 73–80, 2005.

[46] M. Puls, *The Effect of Hydrogen and Hydrides on the Integrity of Zirconium Alloy Components: Delayed Hydride Cracking*, ser. Engineering Materials. Springer London, 2012. [Online]. Available: http://books.google.com/books?id=wKDxctPfv-gC

[47] V. Syasin, E. Boyko, and V. Y. Markin, "Investigations of hardness, internal friction and brittleness of zirconium hydride," *Zeitschrift für Physikalische Chemie*, vol. 164, no. 2, pp. 1567–1572, 1989.

[48] M. Kerr, M. Daymond, R. Holt, and J. Almer, "Strain evolution of zirconium hydride embedded in a zircaloy-2 matrix," *Journal of Nuclear Materials*, vol. 380, no. 1, pp. 70–75, 2008.

[49] S. Yamanaka, K. Yamada, K. Kurosaki, M. Uno, K. Takeda, H. Anada, T. Matsuda, and S. Kobayashi, "Characteristics of zirconium hydride and deuteride," *Journal of alloys and compounds*, vol. 330, pp. 99–104, 2002.

[50] J. Bradbrook, G. Lorimer, and N. Ridley, "The precipitation of zirconium hydride in zirconium and zircaloy-2," *Journal of Nuclear Materials*, vol. 42, no. 2, pp. 142–160, 1972.

[51] G. Carpenter, "The dilatational misfit of zirconium hydrides precipitated in zirconium," *Journal of Nuclear Materials*, vol. 48, no. 3, pp. 264–266, 1973.

[52] R. N. Singh, P. Ståhle, A. R. Massih, and A. Shmakov, "Temperature dependence of misfit strains of δ-hydrides of zirconium," *Journal of Alloys and Compounds*, vol. 436, no. 1, pp. 150–154, 2007.

[53] A. Barrow, A. Korinek, and M. Daymond, "Evaluating zirconium–zirconium hydride interfacial strains by nano-beam electron diffraction," *Journal of Nuclear Materials*, vol. 432, no. 1, pp. 366–370, 2013.

[54] M. Puls, "The effects of misfit and external stresses on terminal solid solubility in hydride-forming metals," *Acta Metallurgica*, vol. 29, no. 12, pp. 1961–1968, 1981.

[55] G. Slattery, "The terminal solubility of hydrogen in zirconium alloys between 30 and 400 c," *INST METALS J*, vol. 95, no. 2, pp. 43–47, 1967.

[56] M. Puls, "Elastic and plastic accommodation effects on metal-hydride solubility," *Acta Metallurgica*, vol. 32, no. 8, pp. 1259–1269, 1984.

[57] J. Lee, Y. Earmme, H. Aaronson, and K. Russell, "Plastic relaxation of the transformation strain energy of a misfitting spherical precipitate: ideal plastic behavior," *Metallurgical transactions A*, vol. 11, no. 11, pp. 1837–1847, 1980.

[58] T. Flanagan, C.-N. Park, and W. Oates, "Hysteresis in solid state reactions," *Progress in Solid State Chemistry*, vol. 23, no. 4, pp. 291–363, 1995.

[59] P. Vizcaíno, J. Santisteban, M. V. Alvarez, A. Banchik, and J. Almer, "Effect of crystallite orientation and external stress on hydride precipitation and dissolution in zr2. 5% nb," *Journal of Nuclear Materials*, vol. 447, no. 1, pp. 82–93, 2014.

[60] R. Tang and X. Yang, "Dissolution and precipitation behaviors of hydrides in n18, zry-4 and m5 alloys," *International Journal of Hydrogen Energy*, vol. 34, no. 17, pp. 7269–7274, 2009.

[61] L. Simpson and M. Puls, "The effects of stress, temperature and hydrogen content on hydride-induced crack growth in zr-2.5 pct nb," *Metallurgical and Materials Transactions A*, vol. 10, no. 8, pp. 1093–1105, 1979.

[62] R. Dutton, K. Nuttall, M. Puls, and L. Simpson, "Mechanisms of hydrogen induced delayed cracking in hydride forming materials," *Metallurgical and Materials Transactions A*, vol. 8, no. 10, pp. 1553–1562, 1977.

[63] M. P. Puls, "Review of the thermodynamic basis for models of delayed hydride cracking rate in zirconium alloys," *Journal of nuclear materials*, vol. 393, no. 2, pp. 350–367, 2009.

[64] M. Puls, "Effects of crack tip stress states and hydride-matrix interaction stresses on delayed hydride cracking," *Metallurgical and Materials Transactions A*, vol. 21, no. 11, pp. 2905–2917, 1990.

[65] K. Une and S. Ishimoto, "Dissolution and precipitation behavior of hydrides in zircaloy-2 and high fe zircaloy," *Journal of Nuclear Materials*, vol. 322, no. 1, pp. 66–72, 2003.

[66] K. Une and S. Ishimoto, "Terminal solid solubility of hydrogen in unalloyed zirconium by differential scanning calorimetry," *Journal of Nuclear Science and Technology*, vol. 41, no. 9, pp. 949–952, 2004.

[67] P. Vizcaino, A. D. Banchik, and J. Abriata, "Calorimetric determination of the δ hydride dissolution enthalpy in zircaloy-4," *Metallurgical and Materials Transactions A*, vol. 35, no. 8, pp. 2343–2349, 2004.

[68] J.-S. Kim and Y.-S. Kim, "Effect of thermal history on the terminal solid solubility of hydrogen in zircaloy-4," *International Journal of Hydrogen Energy*, vol. 39, no. 29, pp. 16 442–16 449, 2014.

[69] P. Vizcaıno, A. Banchik, and J. Abriata, "Solubility of hydrogen in zircaloy-4: irradiation induced increase and thermal recovery," *Journal of nuclear materials*, vol. 304, no. 2, pp. 96–106, 2002.

[70] R. Singh, S. Mukherjee, A. Gupta, and S. Banerjee, "Terminal solid solubility of hydrogen in zr-alloy pressure tube materials," *Journal of Alloys and Compounds*, vol. 389, no. 1, pp. 102–112, 2005.

[71] O. Zanellato, M. Preuss, J.-Y. Buffiere, F. Ribeiro, A. Steuwer, J. Desquines, J. Andrieux, and B. Krebs, "Synchrotron diffraction study of dissolution and precipitation kinetics of hydrides in zircaloy-4," *Journal of Nuclear Materials*, vol. 420, no. 1, pp. 537–547, 2012.

[72] P. Vizcaíno, A. Flores, P. Bozzano, A. Banchik, R. Versaci, and R. Ríos, "Hydrogen solubility and microstructural changes in zircaloy-4 due to neutron irradiation," in *Zirconium in the Nuclear Industry: 16th International Symposium*. ASTM International, 2012.

[73] S.-Q. Shi, G. Shek, and M. Puls, "Hydrogen concentration limit and critical temperatures for delayed hydride cracking in zirconium alloys," *Journal of nuclear materials*, vol. 218, no. 2, pp. 189–201, 1995.

[74] J.-L. Lin, W. Zhong, H. Z. Bilheux, and B. J. Heuser, "Azimuthally anisotropic hydride lens structures in zircaloy 4 nuclear fuel cladding: High-resolution neutron radiography imaging and bison finite element analysis," *Journal of Nuclear Materials*, vol. 496, pp. 129–139, 2017.

[75] A. Hammersley, "Fit2d: an introduction and overview," *European Synchrotron Radiation Facility Internal Report ESRF97HA02T*, vol. 68, p. 58, 1997.

[76] A. Hammersley, S. Svensson, and A. Thompson, "Calibration and correction of spatial distortions in 2d detector systems," *Nuclear Instruments and Methods in Physics Research Section A: Accelerators, Spectrometers, Detectors and Associated Equipment*, vol. 346, no. 1-2, pp. 312–321, 1994.

[77] A. Larson and R. Von Dreele, "Gsas general structure analysis system, report laur 86-748," *Los Alamos National Laboratory, Los Alamos, NM*, 1986.

[78] B. H. Toby, "Expgui, a graphical user interface for gsas," *Journal of applied crystallography*, vol. 34, no. 2, pp. 210–213, 2001.

[79] B. D. Cullity, S. R. Cullity, and S. Stock, *Elements of X-ray Diffraction*, 2001, no. Sirsi) i9780201610918.

[80] A. R. Denton and N. W. Ashcroft, "Vegards law," *Physical review A*, vol. 43, no. 6, p. 3161, 1991.

[81] D. York, N. M. Evensen, M. L. Martınez, and J. D. B. Delgado, "Unified equations for the slope, intercept, and standard errors of the best straight line," *American Journal of Physics*, vol. 72, no. 3, pp. 367–375, 2004.

[82] L.-Q. Chen, "Phase-field models for microstructure evolution," *Annual review of materials research*, vol. 32, no. 1, pp. 113–140, 2002.

[83] X. Ma, S. Shi, C. Woo, and L. Chen, "Effect of applied load on nucleation and growth of γ-hydrides in zirconium," *Computational materials science*, vol. 23, no. 1, pp. 283–290, 2002.

[84] X. Ma, S. Shi, C. Woo, and L. Chen, "Phase-field simulation of hydride precipitation in bi-crystalline zirconium," *Scripta Materialia*, vol. 47, no. 4, pp. 237–241, 2002.

[85] X. Ma, S. Shi, C. Woo, and L. Chen, "The phase field model for hydrogen diffusion and γ-hydride precipitation in zirconium under non-uniformly applied stress," *Mechanics of Materials*, vol. 38, no. 1, pp. 3–10, 2006.

[86] X. Guo, S. Shi, Q. Zhang, and X. Ma, "An elastoplastic phase-field model for the evolution of hydride precipitation in zirconium. part i: Smooth specimen," *Journal of Nuclear Materials*, vol. 378, no. 1, pp. 110–119, 2008.

[87] X. Guo, S. Shi, Q. Zhang, and X. Ma, "An elastoplastic phase-field model for the evolution of hydride precipitation in zirconium. part ii: Specimen with flaws," *Journal of Nuclear Materials*, vol. 378, no. 1, pp. 120–125, 2008.

[88] L. Thuinet, A. De Backer, and A. Legris, "Phase-field modeling of precipitate evolution dynamics in elastically inhomogeneous low-symmetry systems: Application to hydride precipitation in zr," *Acta Materialia*, vol. 60, no. 13, pp. 5311–5321, 2012.

[89] L. Thuinet, A. Legris, L. Zhang, and A. Ambard, "Mesoscale modeling of coherent zirconium hydride precipitation under an applied stress," *Journal of Nuclear Materials*, vol. 438, no. 1, pp. 32–40, 2013.

[90] S.-Q. Shi and Z. Xiao, "A quantitative phase field model for hydride precipitation in zirconium alloys: Part i. development of quantitative free energy functional," *Journal of Nuclear Materials*, vol. 459, pp. 323–329, 2015.

[91] Z. Xiao, M. Hao, X. Guo, G. Tang, and S.-Q. Shi, "A quantitative phase field model for hydride precipitation in zirconium alloys: Part ii. modeling of temperature dependent hydride precipitation," *Journal of Nuclear Materials*, vol. 459, pp. 330–338, 2015.

[92] A. M. Jokisaari and K. Thornton, "Hyrax: Phase field modeling of zirconium hydride precipitation and growth in zirconium." Raleigh, NC: 12th US National Congress on Computational Mechanics, (USNCCM12), 2013, pp. 22 – 25.

[93] D. Gaston, C. Newman, G. Hansen, and D. Lebrun-Grandie, "Moose: A parallel computational framework for coupled systems of nonlinear equations," *Nuclear Engineering and Design*, vol. 239, no. 10, pp. 1768–1778, 2009.

[94] A. Jokisaari and K. Thornton, "General method for incorporating calphad free energies of mixing into phase field models: Application to the α-zirconium/δ-hydride system," *Calphad*, vol. 51, pp. 334–343, 2015.

[95] J. W. Cahn and J. E. Hilliard, "Free energy of a nonuniform system. i. interfacial free energy," *The Journal of chemical physics*, vol. 28, no. 2, pp. 258–267, 1958.

[96] S. M. Allen and J. W. Cahn, "A microscopic theory for antiphase boundary motion and its application to antiphase domain coarsening," *Acta Metallurgica*, vol. 27, no. 6, pp. 1085–1095, 1979.

[97] R. H. Stogner, G. F. Carey, and B. T. Murray, "Approximation of cahn–hilliard diffuse interface models using parallel adaptive mesh refinement and coarsening with c1 elements," *International journal for numerical methods in engineering*, vol. 76, no. 5, pp. 636–661, 2008.

[98] M. R. Tonks, D. Gaston, P. C. Millett, D. Andrs, and P. Talbot, "An object-oriented finite element framework for multiphysics phase field simulations," *Computational Materials Science*, vol. 51, no. 1, pp. 20–29, 2012.

[99] J. Kearns, "Diffusion coefficient of hydrogen in alpha zirconium, zircaloy-2 and zircaloy-4," *Journal of Nuclear Materials*, vol. 43, no. 3, pp. 330–338, 1972.

[100] G. Majer, W. Renz, and R. Barnes, "The mechanism of hydrogen diffusion in zirconium dihydrides," *Journal of Physics: Condensed Matter*, vol. 6, no. 15, p. 2935, 1994.

[101] N. Dupin, I. Ansara, C. Servant, C. Toffolon, C. Lemaignan, and J. Brachet, "A thermodynamic database for zirconium alloys," *Journal of nuclear materials*, vol. 275, no. 3, pp. 287–295, 1999.

[102] A. Dinsdale, "Sgte data for pure elements," *Calphad*, vol. 15, no. 4, pp. 317–425, 1991.

[103] M. Avrami, "Kinetics of phase change. i general theory," *The Journal of Chemical Physics*, vol. 7, no. 12, pp. 1103–1112, 1939.

[104] D. A. Porter, K. E. Easterling, and M. Sherif, *Phase Transformations in Metals and Alloys, (Revised Reprint)*. CRC press, 2009.

[105] K. Une, K. Nogita, S. Ishimoto, and K. Ogata, "Crystallography of zirconium hydrides in recrystallized zircaloy-2 fuel cladding by electron backscatter diffraction," *Journal of nuclear science and technology*, vol. 41, no. 7, pp. 731–740, 2004.